People's Democratic Republic of Algeria

Ministry of Higher Education and Scientific Research

University of El Oued

Faculty of Exact Sciences

Laboratory of LABTHOP

A Doctoral Thesis

Submitted in Fulfillment of the Requirements for Degree of Doctor (LMD)

Field: PHYSICS

Specialization: Applied Physics

Title: Study and modeling of non-linear propagation in Single-Mode optical fibers

Presented by: Mesbahi Tahar

Defended on [02/06/2026], in the presence of the Examination Committee:

Name	Rank	Affiliation	Role
Azzedine Beggas	Professor	University of El oued	Chair
Abdelkader Medjouri	Professor	University of El oued	Supervisor
Mosbah Difallah	Professor	University of El oued	Examiner
Said Mehellou	Professor	University of El oued	Examiner
Djamel Abed	Professor	University of Guelma	Examiner
Soufiane Benhamida	Professor	University of Ouargla	Examiner

Academic Year: 2024-2025 / 1446-1447 AH

Acknowledgements

First and foremost, I would like to express my sincere gratitude to my supervisor, Professor **Medjouri Abdelkader**, for his valuable guidance, continuous support, and encouragement throughout the course of this research. His expertise and vision were fundamental in shaping the direction and outcomes of this work.

My thanks also go to Prof. **Azzedine Beggas**, Chair of the defense committee, for his encouragement and support.

I am also grateful to the examiners, Prof. **Mosbah Difallah**, Prof. **Said Mehellou** (University of El Oued), Prof. **Djamel Abed** (University of Guelma), and Prof. **Soufiane Benhamida** (University of Ouargla), for their time, remarks, and helpful comments that contributed to improving this thesis.

I also extend my heartfelt thanks to the Faculty of Exact Sciences at Hamma Lakhdar University, El-Oued, for providing the necessary resources and a supportive academic environment, especially Professor **Dalmi Samia**, the supervisor of the research project.

Lastly, I would like to express my profound gratitude to my family and friends for their unwavering support and encouragement throughout this journey.

Tahar Mesbahi

2025

Abstract

This thesis investigates the nonlinear propagation in optical fibers with emphasis on supercontinuum (SC) generation. The fundamentals of optical fibers are introduced, including standard and photonic crystal fibers (PCFs), their fabrication methods, linear properties, and applications. Nonlinear effects of second and third order, such as harmonic generation, phase matching, self- and cross-phase modulation, solitons, four-wave mixing, Raman and Brillouin scattering, are also discussed. Numerical methods for SC modeling, namely the Runge-Kutta in the interaction picture (RK4IP) and the Split-Step Fourier Method (SSFM), are presented to analyze spectral dynamics in different dispersion regimes. A $Ge_{20}As_{20}Se_{17}Te_{43}$ chalcogenide PCF was designed and numerically analyzed for broadband supercontinuum generation in the all-normal dispersion regime. Using RK4IP-based solutions of the generalized nonlinear Schrödinger equation (GNLSE), a stable and coherent SC spectrum spanning 2.9–13.95 μm at the −5 dB level was achieved with a 5.8 μm wavelength pump, 50 fs pulses, and a 15 kW over 15 cm fiber length. These results provide guidelines for future experimental work and the development of tailored chalcogenide fibers for spectroscopy and frequency metrology.

Keywords: Photonic crystal fibre (PCF), supercontinuum (SC), nonlinear, RK4IP method.

Résumé

Cette thèse étudie la propagation non linéaire dans les fibres optiques, avec un accent particulier sur la génération de supercontinuum (SC). Les principes fondamentaux des fibres optiques sont présentés, incluant les fibres standards et les fibres à cristal photonique (PCFs), leurs méthodes de fabrication, leurs propriétés linéaires et leurs applications. Les effets non linéaires d'ordre deux et trois, tels que la génération d'harmoniques, l'accord de phase, la modulation de phase auto- et croisée, le mélange à quatre ondes, les solitons, ainsi que les diffusions Raman et Brillouin, sont également abordés. Des méthodes numériques de modélisation du SC, notamment la méthode de Fourier à pas fractionné (SSFM) et Runge-Kutta dans l'image d'interaction (RK4IP), sont utilisées pour analyser la dynamique spectrale dans différents régimes de dispersion. Une fibre à cristal photonique en verre chalcogénure $Ge_{20}As_{20}Se_{17}Te_{43}$ a été conçue et analysée numériquement pour la génération large bande de SC en régime de dispersion tout-normal. En résolvant l'équation de Schrödinger non linéaire généralisée (GNLSE) avec RK4IP, un spectre SC stable et cohérent couvrant la plage 2,9–13,95 µm à −5 dB a été obtenu avec une puissance crête de pompe de 15 kW, des impulsions de 50 fs et une longueur de fibre de 15 cm. Ces résultats fournissent des lignes directrices pour de futurs travaux expérimentaux et la conception de fibres chalcogénures adaptées aux applications en spectroscopie et en métrologie de fréquence.

Mots-clés : Fibre à cristal photonique (PCF), supercontinuum (SC), non linéaire, méthode RK4IP.

ملخص

تهدف هذه الأطروحة إلى دراسة الانتشار اللاخطي في الألياف البصرية مع التركيز على توليد الطيف الفائق المستمر (SC). وقد تم عرض الأسس والمبادئ النظرية للألياف البصرية، بما في ذلك الألياف الكلاسيكية والألياف البلورية الضوئية (PCFs)، وطرق تصنيعها، وخصائصها الخطية، وتطبيقاتها. كما تمت مناقشة التأثيرات اللاخطية من المرتبة الثانية والثالثة، مثل توليد التوافقيات، والمطابقة الطورية، والانتشار الذاتي والمتبادل للطور، والخلط الرباعي للأمواج، والسوليتونات، بالإضافة إلى تشتت رامان وبريلوين. تم عرض الطرق العددية المعتمدة في نمذجة الطيف الفائق المستمر، وهي طريقة (SSFM) وطريقة (RK4IP)، وذلك لتحليل الديناميكيات الطيفية في أنظمة التبدد المختلفة. كما تم تصميم ليف بلوري ضوئي مصنوع من زجاج كالكوجيني $Ge_{20}As_{20}Se_{17}Te_{43}$ وتحليله عددياً لتوليد الطيف الفائق المستمر في نظام التبدد السالب. وباستخدام طريقة RK4IP لحل معادلة شرودنغر اللاخطية المعممة (GNLSE). تم الحصول على الطيف الفائق المستمر مستقر ومتجانس يغطي المجال من 2.9 إلى 13.95 ميكرومتر عند مستوى 5− ديسبل، وذلك عند الضخ النبضة بطول موجي قدره 5.8 ميكرومتر، زمنها 50 فيمتوثانية، وبقدرة 15 كيلواط ، ضمن ليف يبلغ طوله 15 سم. وتوفر هذه النتائج رؤية مهمة للأعمال التجريبية المستقبلية، وتسهم في تطوير ألياف كالكوجينية مُصمَّمة خصيصًا لتطبيقات التحليل الطيفي ومعايرة الترددات المترولوجية.

الكلمات المفتاحية: الألياف البلورية الضوئية (PCF)، الطيف الفائق المستمر، الزجاج الكالكوجيني، طريقة RK4IP.

Table of Contents

Chapter 4:

Modeling of Supercontinuum Generation in Chalcogenide PCF

List of figures

Chapter 1:

Chapter 2:

Chapter 3:

Chapter 4:

List of tables

List of Acronyms

Term	**Meaning**
ANDi	All-normal chromatic dispersion
BPM	Birefringent phase matching
SRS	Stokes Raman scattering
ChGs	Chalcogenide glasses
CL	Circular Lattice
CW	Continuous-wave
EM	Electromagnetic
FDFD	Finite-difference frequency-domain method
FWM	Four-wave mixing
FSF	Frequency Sum Generation
GAST	$Ge_{20}As_{20}Se_{17}Te_{43}$
GDF	Frequency Difference Generation
GNLSE	Generalized Nonlinear Schrödinger Equation
GVD	Group velocity dispersion
HC-PCF	Hollow-core photonic crystal fibers
HOM	Higher-order spatial modes
KDP	Potassium dihydrogen phosphate
LAN	Local area network
LPGs	Long-period gratings
MI	Modulation instability
MIR	Mid-infrared
MM-GNLSE	Multimode generalized nonlinear Schrödinger equation
MMF	Multimode optical fiber
OCT	Optical coherence tomography
OPOs	Optical Parametric Oscillators
OWB	Optical Wave breaking
PCF	Photonic crystal fibers
PBG	Photonic bandgap

PML	Perfectly matched layers
RK4IP	Runge-Kutta in the interaction picture
SBS	Stimulated Brillouin scattering
SC	Supercontinuum
SHG	Second harmonic generation
SPM	Phase modulation
SRS	Stimulated Raman scattering
SMF	Single-mode fibers
SSFM	Split-step Fourier method
THG	Third-harmonic generation
THz	Terahertz
TOD	Third-order dispersion
XPM	Cross-phase modulation
ZBLAN	ZrF_4 BaF_2 LaF_3 AlF_3 NaF
ZDW	Zero-dispersion wavelength

List of Symbols

Symbols	Meaning
V	The normalized frequency
Λ	The wavelength
N	The refractive index
Λ	The lattice constant or pitch
D	The diameter of the holes
B	The propagation constant
k	The angular wave number
I	The intensity
L_c	The confinement losses
n_{eff}	The effective refractive index
L	The propagation length.
f	Frequency
ω	The angular frequency
c	velocity of light in vacuum
D_c	The chromatic dispersion
B	The birefringence
A_{eff}	The effective area
p	The polarization
E	The electric feld
ϵ_0	The permittivity of a vacuum
χ	The susceptibility
L_{Co}	The coherence length
n_2	The nonlinear index coefficient
γ	The Kerr effect
A(z,T)	The pulse envelope
R(T)	The delayed Raman response
$\phi(t)$	The phase
Ω_{Dv}	The frequency detuning of the dispersive wave

List of Symbols

P_0	The pick power
T_{FWHM}	The width-half-maximum duration
H	The magnetic field
σ	The conductivity
$\lvert g_{12}^{1}(\lambda)\rvert$	The first-order degree of coherence
L_D	The dispersive length
L_{NL}	The nonlinear length
L_{OWB}	The wave-breaking distance

General introduction

The generation of broad and continuous spectra resulting from the propagation of intense optical pulses through a nonlinear medium is known as supercontinuum (SC) generation. The broadband radiation, produced through nonlinear frequency conversion of a tightly focused, high-intensity laser beam within a dielectric medium, is commonly referred to as a supercontinuum. Rather than representing a single phenomenon, the term "supercontinuum" encompasses various nonlinear effects that collectively contribute to a substantial spectral broadening of optical pulses, often extending over several octaves. The dispersion characteristics of the medium play a decisive role in governing the underlying nonlinear mechanisms, which include phase matching, soliton dynamics, self-phase modulation (SPM), and Raman scattering [1,2].

SC sources have been extensively utilized in many different applications, spanning fundamental research in chemistry, physics, and biology, as well as excitation spectroscopy and absorption [3]. They have enabled the production of femtosecond short pulses for applications such as optical clocks and frequency combs [4], which played a pivotal role in metrology and contributed to a Nobel Prize in 2005. Additional applications include atmospheric science, optical communication, ranging and light detection [5]. SC sources are also critical in biomedical imaging methods like OCT (optical coherence tomography) [6] and CARS (coherent anti-Stokes Raman scattering) [7], as well as in live-cell imaging using advanced microscopy methods [8].

Supercontinuum (SC) generation has been extensively studied across diverse nonlinear media, such as gases, liquids, solids, and different classes of waveguides. The first observation of this phenomenon was reported by Alfano and Shapiro in 1970 in bulk borosilicate glass, known for its notable nonlinear properties [9]. Selecting media with high nonlinearity and low loss, optimizing the overall chromatic dispersion (CD) through waveguide dispersion engineering, and choosing an appropriate injection pulse are essential strategies for SC generation [10]. The optical waveguide, under femtosecond pumping, leads to the generation of spectrally continuous radiation through the combined effects of several linear and nonlinear processes. This process is strongly influenced by the dispersion profile of the waveguide [11]. When optical pumping is performed in the anomalous dispersion regime, the supercontinuum (SC) generation process is primarily governed by soliton dynamics, dispersive wave emission, and Raman-induced self-frequency shift. The resulting spectra can span an extremely broad bandwidth, as new optical components arise from the fission of higher-order solitons. Nevertheless, the coherence of these spectra is often compromised, since their evolution is highly sensitive to noise amplification, which causes significant pulse-to-pulse fluctuations. Conversely, in the normal dispersion regime, SC generation is mainly driven by self-phase modulation (SPM), while spectral broadening toward longer wavelengths is facilitated by the optical wave-breaking (OWB) effect. Although the spectral width obtained in this case is narrower compared to that in the anomalous regime, the output exhibits a smoother shape and a substantially higher degree of coherence [12].

Conventional highly nonlinear optical fibers, which employ either a small mode area or highly nonlinear materials in the fiber core, have been widely used for supercontinuum generation. Since their introduction by Knight et al. (1996, 1998), photonic crystal fibers (PCFs) have attracted significant attention due to their unique properties, including high modal birefringence, large nonlinear coefficients, dispersion tailoring and management, and endlessly single-mode transmission. Among these properties, highly nonlinear effects stand out as an intriguing phenomenon that can be utilized for various applications, such as supercontinuum spectrum generation and slow light effects. As a result, PCFs offer a novel approach for supporting supercontinuum generation compared to conventional fibers [13].

An extensive variety of soft-glass PCFs, such as those made from chalcogenide, fluoride, and tellurite glasses, have been the focus of extensive research owing to their large nonlinear refractive indices and broad infrared transparency. In particular, ChG glasses offer a remarkably wide transmission window, extending from the visible region to wavelengths as long as 25 µm, depending on composition, together with a high linear refractive index typically ranging between 2.0 and 3.5. Furthermore, their nonlinear refractive index is several hundred times larger than that of fluoride-based glasses, making them highly attractive for nonlinear optical applications [14]. In 2000, M. Monro et al. reported the fabrication of the first non-silica holey or photonic crystal fibers. The study utilized chalcogenide glass based on Gallium Lanthanum Sulphide (GLS). Applications of these fibers included acousto-optic devices, optical switching, high power delivery, air-guiding fibers, fiber sensors, and mid-infrared devices, among others. Additionally, the research highlighted that holey fiber technology provides an improved route toward fabricating single-mode compound glass fibers [15].

Chalcogenide-based PCFs, with their high nonlinearities and broad infrared transmission windows, have proven to be highly suitable for SC production in region of the infrared. In 2005, B. Shaw et al. conducted the first study on SC production in photonic crystal fibers (PCFs)-based chalcogenide. The study demonstrated SC production in an As-Se-PCF, when pumped with 100 fs pulses at a wavelength of 2.5 um, the spectrum spans from 2.1 um to 3.2 nm. [16]. In recent years, the spectral width of the supercontinuum in chalcogenide waveguides has rapidly increased. tellurium-, selenium-, and Sulfur-based chalcogenide waveguides have enabled the generation of supercontinuum spectra spanning 2–16 µm, 2–14 µm, and 1.5–8 µm, respectively [17]. Compared to S- or Se-based glasses, Te-based chalcogenide glasses are more attractive for mid-IR supercontinuum production due to their broader transmission windows and higher optical nonlinearities, which result from the higher atomic weight of Te. However, the metallic nature of Te leads to an increased tendency for crystallization, hindering the production of low-loss optical fibers due to excessive scattering. Replacing a small amount of Te with Se improves resistance to crystallization while maintaining a wide optical transmission window. Nevertheless, the attenuation of such fibers remains high (>10 dB/m), and their drawing process is challenging to control [18]. The first experimental demonstration of supercontinuum (SC) generation in a tellurium-based chalcogenide step-index fiber was reported by Z. Zhao et al. in 2016. The low-loss fiber, fabricated using isolated extrusion, exhibited record optical losses of 2–3 dB/m at 6.2–10.3 µm and generated a spectrum spanning 1500–14000 nm when pumped with a 4500 nm, ~150 fs laser [19].

Coherent mid-infrared (mid-IR) radiation has gained significant interest because its wide range of applications in scientific and technological fields, including industrial process control, spectroscopy, frequency metrology, information technology, photobiology, photomedicine, and photochemistry [20]. With all-normal and flat-top dispersion profiles, photonic crystal fibers are particularly well-suited for exploiting the intrinsic coherence characteristics of supercontinuum generation. In this context, several efforts have been devoted to designing chalcogenide based on photonic crystal fibers with flat-top and all-normal dispersion [21]. In 2020, Jing Xiao et al. employed numerical simulations to investigate the coherence of supercontinuum (SC) generation. "Their results demonstrated that an all-normal dispersion fiber composed of Ge, As, Se, and Te glasses can generate a highly coherent supercontinuum spanning the 3.5–10.5 µm wavelength range.

The relatively large material zero-dispersion wavelengths (ZDWs) of this tellurium-based glass facilitate the realization of an all-normal dispersion profile [22].

In this study, we propose a general model for supercontinuum production in single-mode PCFs. The $Ge_{20}As_{20}Se_{17}Te_{43}$ glass is selected as the solid background material due to its exceptional characteristics, including long-wave infrared (IR) transparency and the ability to obtain an ANDi (all-normal dispersion) regime, thanks to its larger material zero-dispersion wavelength (ZDW). Additionally, we propose a PCF design based on a circular lattice (CL-PCF), characterized by six rings to ensure efficient light confinement within the fiber core. The nonlinear and linear optical properties are meticulously calculated across various wavelengths using the FDFD method, complemented by perfectly matched layers (PML) as boundary conditions. And, the GNLSE is numerically solved to model the propagation of optical pulses and the supercontinuum production process.

This manuscript consists of four chapters:

Chapter1 provides an overview of optical fibers, beginning with their fundamental principles and classifications. It covers standard fibers, which form the backbone of optical communication, and introduces photonic crystal fibers (PCFs), which offer unique structural and optical advantages. The chapter discusses the fabrication techniques and mechanisms of PCFs, including their linear properties such as propagation losses, chromatic dispersion, effective area, and birefringence. Additionally, it highlights the applications of PCFs, while emphasizing the impact of material selection on their performance.

Chapter 2 focuses on second- and third-order nonlinearities in optical fibers. It discusses the principles and mechanisms behind these nonlinear effects, with fibers providing a platform for high field confinement and long interaction lengths. The chapter covers second-order effects like phase matching, SHG (second harmonic generation), as well as parametric processes, followed by third-order effects such as cross-phase modulation, self-phase modulation, four-wave mixing, solitons, Brillouin scattering and Raman.

Chapter 3 presents an overview of supercontinuum (SC) generation, including its applications and mechanisms in bulk media and waveguides, with a focus on single-mode and multimode fibers.

It discusses two numerical methods for simulating SC generation: the RK4IP method and the SSFM. The chapter also covers broadening mechanisms and spectral dynamics in different dispersion regimes, highlighting key interactions in the anomalous, normal, and all-normal dispersion regimes. Finally, we introduced the modeling of multimode SC generation, which is described by the multimode generalized nonlinear Schrödinger equation (MM-GNLSE).

Chapter 4 provides the findings on supercontinuum (SC) production in a single-mode PCF based on $Ge_{20}As_{20}Se_{17}Te_{43}$ as the background glass with an ANDi regime. The nonlinear and linear properties of the fiber are precisely calculated for various wavelengths using the FDFD method, along with the perfectly matched layers (PML) boundary condition. The propagation of optical pulses and the supercontinuum generation process are then modeled by numerically solving the GNLSE.

A summary of these works, along with some perspectives, are provided in the general conclusion of this manuscript.

Reference

[1]. Dudley, J. M., & Genty, G. Supercontinuum light. Physics today, 66(7), 29-34. (2013).

[2]. Granzow, N. Supercontinuum white light lasers: a review on technology and applications. Photonics and Education in Measurement Science 2019, 11144, 34-38. (2019).

[3]. Poudel, C., & Kaminski, C. F. Supercontinuum radiation in fluorescence microscopy and biomedical imaging applications. JOSA B, 36(2), A139-A153. (2019).

[4]. Udem, T., Holzwarth, R., & Hänsch, T. W. Optical frequency metrology. Nature, 416(6877), 233-237. (2002).

[5]. Kasparian, J., Rodríguez, M., Méjean, G., Yu, J., Salmon, E., Wille, H., ... & Woste, L. White-light filaments for atmospheric analysis. Science, 301(5629), 61-64. (2003).

[6]. Huang, D., Swanson, E. A., Lin, C. P., Schuman, J. S., Stinson, W. G., Chang, W., & Fujimoto, J. G. Optical coherence tomography. Science, 254(5035), 1178-1181. (1991).

[7]. McConnell, G. Confocal laser scanning fluorescence microscopy with a visible continuum source. Optics Express, 12(13), 2844–2850. (2004).

[8]. Kaminski, C. F., Watt, R. S., Elder, A. D., Frank, J. H., & Hult, J. Supercontinuum

radiation for applications in chemical sensing and microscopy. Applied Physics B, 92, 367-378. (2008).

[9]. Dai, S., Wang, Y., Peng, X., Zhang, P., Wang, X., & Xu, Y. A review of mid-infrared supercontinuum generation in chalcogenide glass fibers. Applied Sciences, 8(5), 707. (2018).

[10]. Fang, Y., Bao, C., Li, S. A., Wang, Z., Geng, W., Wang, Y., ... & Yue, Y. Recent progress of supercontinuum generation in nanophotonic waveguides. Laser & Photonics Reviews, 17(1), 2200205. (2023).

[11]. Medjouri, A., Abed, D., & Becer, Z. Numerical investigation of a broadband coherent supercontinuum generation in Ga8Sb32S60 chalcogenide photonic crystal fiber with all-normal dispersion. Opto-Electronics Review, 27(1), 1-9. (2019).

[12]. Dudley, J. M., Genty, G., & Coen, S. Supercontinuum generation in photonic crystal fiber. Reviews of modern physics, 78(4), 1135-1184. (2006).

[13]. Li, J., Wang, J., Teng, Y., Xu, Z., & Cheng, J. Broadband supercontinuum generation based on filled structural photonic crystal fibers with low incident optical power. Optical and Quantum Electronics, 52, 1-11. (2020).

[14]. Yuan, Y., Xia, K., Wang, Y., Liu, Z., Zhang, N., Su, J., ... & Dai, S. Precision fabrication of a four-hole Ge 15 Sb 15 Se 70 chalcogenide suspended-core fiber for generation of a 1.5–12 μm ultrabroad mid-infrared supercontinuum. Optical Materials Express, 9(5), 2196-2205. (2019).

[15]. Monro, T. M., West, Y. D., Hewak, D., Broderick, N. G. R., & Richardson, D. J. Chalcogenide holey fibres. Electronics Letters, 36(24), 1998-2000. (2000).

[16]. Shaw, L. B., Thielen, P. A., Kung, F. H., Nguyen, V. Q., Sanghera, J. S., & Aggarwal, I. D. IR supercontinuum generation in As-Se photonic crystal fiber. In Advanced Solid-State Photonics (p. TuC5). Optica Publishing Group. (2005).

[17]. Zhang, M., Li, L., Li, T., Wang, F., Tian, K., Tao, H., ... & Yang, Z. Mid-infrared supercontinuum generation in chalcogenide fibers with high laser damage threshold. Optics Express, 27(20), 29287-29296. (2019).

[18]. Lemiere, A., Désévédavy, F., Mathey, P., Froidevaux, P., Gadret, G., Jules, J. C., ... & Smektala, F. Mid-infrared supercontinuum generation from 2 to 14 μm in arsenic-and antimony-free chalcogenide glass fibers. JOSA B, 36(2), A183-A192. (2019).

[19]. Zhao, Z., Wang, X., Dai, S., Pan, Z., Liu, S., Sun, L., ... & Wang, R. 1.5–14 μm midinfrared supercontinuum generation in a low-loss Te-based chalcogenide step-index fiber. Optics letters, 41(22), 5222-5225. (2016).

[20]. Dudley, J. M., & Coen, S. Coherence properties of supercontinuum spectra generated in photonic crystal and tapered optical fibers. Optics letters, 27(13), 1180-1182. (2002).

[21]. Saini, T. S., Kumar, A., & Sinha, R. K. Broadband mid-IR supercontinuum generation in As2Se3 based chalcogenide photonic crystal fiber: A new design and analysis. Optics Communications, 347, 13-19. (2015).

[22]. Xiao, J., Tian, Y., Zhao, Z., Yao, J., Wang, X., Chen, P., ... & Wang, R. Investigation of tellurium-based chalcogenide double-clad fiber for coherent mid-infrared supercontinuum generation. Optical Fiber Technology, 55, 102144. (2020).

Chapter 1:

Optical Fibers (General Presentation and Propagation Properties)

1. Introduction

This chapter provides a comprehensive overview of optical fibers, focusing on their general presentation and propagation properties. It begins with an introduction to standard optical fibers, followed by a discussion on different types of optical fibers, with special emphasis on photonic crystal fibers. PCFs, a recent advancement in technology of optical fiber, are introduced with details on their structure and the fabrication techniques used to create them. The chapter delves into the unique guiding mechanisms in PCFs, highlighting their linear properties and how they differ from conventional fibers. The chapter also covers the classification of PCFs into single-mode and multi-mode fibers, with an exploration of the various propagation losses encountered in these fibers, including absorption losses, scattering losses, and confinement losses. Additionally, chromatic dispersion and birefringence, which play crucial roles in the performance of optical fibers, are discussed in detail.

2. General Introduction to Optical Fibers:

The transmission of information through light has long been utilized by humans. Tracing back to antiquity, the positioning of stars and coastal lighthouses guided sailors. In the 16th century, the construction of Genoese towers enabled the prevention of piracy acts through the rapid propagation of light signals from one tower to adjacent ones. More recently, Alexander G. Bell, known for the invention of the telephone, developed the photophone in 1880. This system transmitted a sound signal in the form of light by vibrating a mirror that reflected sunlight, while a similar device located up to 200 meters away allowed the reproduction of the original sound signal. Although considered a precursor, this airborne process was highly sensitive to atmospheric disturbances, and its relatively short range doomed the invention. To address this limitation, the early works of John L. Baird and Clarence W. Hansell in 1927 led to a patent on the transmission of television images using fine glass fibers, although this process was never fully implemented. Then, in 1930, Heinrich Lamm succeeded in transmitting the first image of a filament through a quartz fiber network. It was not until after 1960, with Theodore H. Maiman's invention of the ruby laser, that optical fiber transmission saw renewed interest. Indeed, in 1964, Charles K. Kao described and envisioned a communication system relying on the combined use of lasers and optical fibers. His visionary work on silica fibers and the experimental demonstration of the proof of concept for long-distance optical information transmission earned him the 2009 Nobel Prize in Physics. From then on, a technological race began to develop low-loss optical fibers, enabling transmission over greater distances Typically made of silica (SiO_2), these optical fibers possess properties that can vary greatly depending on their types and manufacturing processes [1].

3. Standard fibers.

Since 1970, the demonstration of low-loss propagation in fibers of silica has greatly accelerated the development of optical fibers, Light transmission applications commonly use optical fibers as waveguides. A layer of glass or plastic, known as cladding, encases the optical fiber's core and distinguishes it by possessing a lower refractive index than the core. Typically, optical fibers consist of a single cladding, a single core, and a protective coating. The jacket, buffer, cladding, and core are the four primary parts of an optical fiber, as shown in Fig. 1[2].

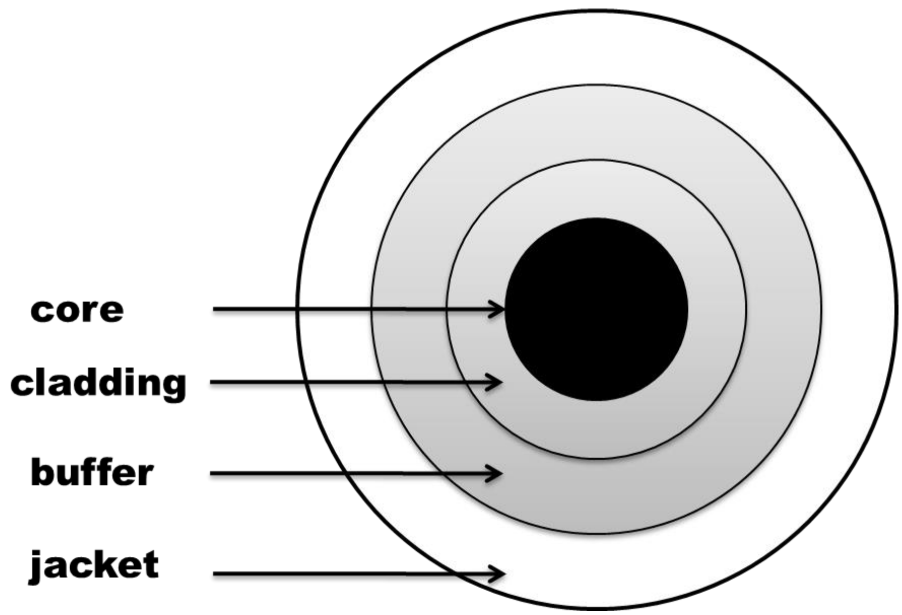

Fig. 1. *Structure of standard optical fiber. Adapted from [2].*

The fundamental operating principle of optical fibers is TIR (total internal reflection), which occurs when the angle of incidence of light within the core exceeds the critical angle at the interface between the core and the cladding. Under this condition, the light is confined within the core by repeated reflections, ensuring its propagation along the fiber. When the incidence angle is greater than the critical angle, the light does not penetrate into the cladding but instead remains guided inside the core. The extent of confinement depends on the refractive indices of the core and cladding, as well as the angle of incidence. Figure 2 illustrates the phenomenon of total internal reflection. [3].

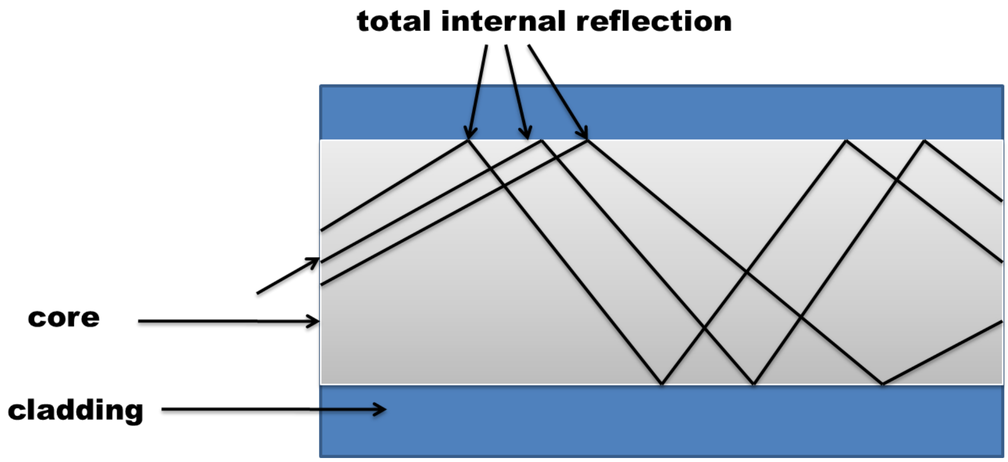

Fig. 2. Total internal reflection in fibers. Adapted from [3].

3.1 Optical fiber types

In general, optical fibers can be classified based on their structure (planar or cylindrical), number of modes, and refractive index profile. Based on their refractive index profile, fibers are typically divided into two types: step-index and graded-index fibers. Step-index fibers have a sharp discontinuity at the interface between the cladding and the core, with a core of constant refractive index. In contrast, graded-index fibers possess a core whose refractive index is maximum at the center and gradually decreases toward the cladding. Based on the number of supported modes, fibers are further divided into two categories fibers: single-mode and multimode, as illustrated in Fig. 3.

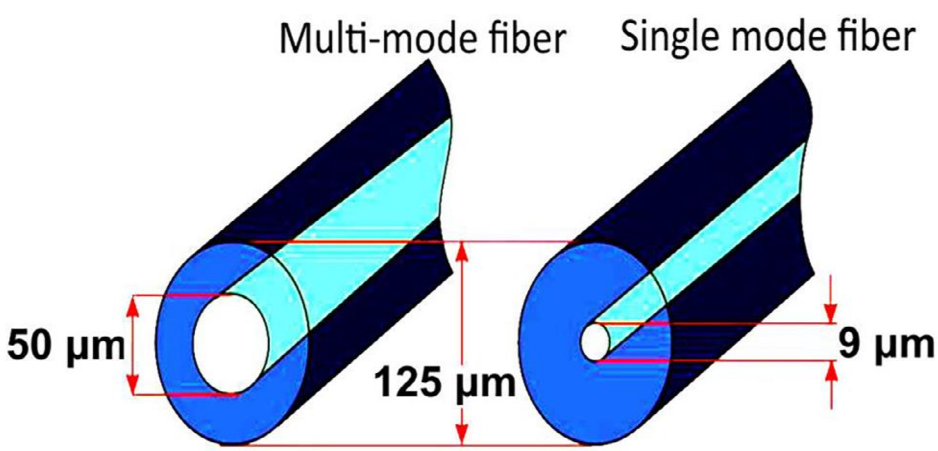

Fig. 3. Dimensions of multi-mode and single-mode optical fibers. Reproduced from [4].

The best option for long-distance communication is a single-mode fiber, making them ideal for applications such as multi-channel TV transmission systems and long-distance telephone. The core diameters of these fibers are small, typically 5000 or 10000 nm. On the other hand, for communication across short distances, multimode fibers are utilized, such as video surveillance and local area network (LAN) systems. Their core sizes range from 50 to 62.5 µm. The large core diameter causes light to travel along multiple optical paths in a random manner; the rays arrive at the detector at varying times as a result. This leads to temporary broadening of the signal, which can reduce effective range to around 200–500 meters and data transmission speed [4].

The normalized frequency, often denoted as, is a dimensionless parameter used in optical fiber analysis to determine the mode propagation conditions. It is defined by the equation [2]:

$$V = \frac{2\pi a}{\lambda_0}\sqrt{n_1^2 - n_2^2} \quad (1)$$

Where n_2 and n_1 denote the refractive indices of the cladding and core, respectively. The fiber core diameter is denoted by a and the operating wavelength is λ_0 .

For $V > 2.405,$ the fiber works as a multimode. and $V < 2.405$, The fiber is single-mode.

Because single-mode fibers have a small core diameter, light propagates along the fiber axis. For light propagation to occur in single-mode fibers, a specific condition must be met, namely that the value of V must be less than 2.405 [5].

4. Photonic crystal fibers

Photonic crystal fibers (PCFs) represent a groundbreaking advancement in optical fiber technology, emerging from the broader field of photonic crystals, which were conceptualized in the late 20th century. The theoretical foundation of photonic crystals was laid by Eli Yablonovitch and Sajeev John in 1987, who independently proposed the ability of periodic dielectric structures to manipulate the flow of light. This concept inspired the development of various optical devices, including PCFs. The first practical demonstration of a PCFs was introduced in 1996 by Philip Russell. Unlike conventional fibers, which guide light through a uniform core-cladding refractive index difference, PCFs rely on a periodic arrangement of air holes in their cladding. This unique structure allows for superior control of light propagation, enabling endlessly single-mode operation, a broader range of dispersion control, and exceptional nonlinear optical properties. When compared to traditional optical fibers, PCFs offer several advantages. For instance, they can achieve much lower attenuation and higher confinement of light, making them perfect for applications using high-power lasers. Additionally, the tunable design of their microstructure allows engineers to customize their properties for specific uses, such as supercontinuum generation or hollow-core guidance for low-loss gas transmission. In contrast, conventional fibers are often limited in their ability to tailor dispersion and nonlinear characteristics. PCFs have thus expanded the range of applications for optical fibers, including advanced sensing, telecommunications, and biomedical imaging. Research now focuses on improving PCF fabrication for longer fiber lengths and lower losses, opening pathways for advanced applications [6]. Table 1 summarizing the development of PCFs.

Table. 1. *summarizing the development of photonic crystal fibers (PCFs) [7].*

Year	Researcher/Group	Contribution/Idea	Key Details
1987	Yablonovitch	Concept of photonic bandgap (PBG)	Introduced PBG for in-plane structures.
1991	Philip Russell	Hollow-core waveguide based on 2D out-of-plane PBG	Focused on overcoming high-refractive-index material constraints.
1995	Birks et al.	Air-glass interface in fiber optics	Made the hollow-core waveguide compatible with fiber-optics technology.
1996	Russell & colleagues	First photonic-crystal fiber (PCF) demonstration	Developed fiber with micrometer-scale holes in a hexagonal pattern.
1997	Birks, Knight, and St. J. Russell	Solid-core PCF guidance principle	Introduced single-mode guidance for all wavelengths.
1999	Cregan et al.	First hollow-core PCF (HC-PCF) demonstration	Achieved confinement of more than 99% of light in core over narrow transmission windows.
2001	Russell	Air-core fiber for waveguiding	Demonstrated a new approach to overcome material attenuation, dispersion, and nonlinear effects.
2003	Smith et al.	Low-loss HC-PCF	Reported losses as low as 1 dB/km in hollow-core PCF.
2005	Roberts et al.	HC-PCF improvement	Further reduction in losses and development in fabrication process.

4.1 Structure of a Photonic Crystal Fiber (PCF)

A PCF is formed by a two-dimensional lattice composed of air holes arranged parallel to the propagation axis within a silica matrix. The opto-geometrical parameters defining the microstructure in the cladding are the distance between the centers of two adjacent holes, denoted by Λ (lattice constant or pitch), d represents the diameter of the air holes, and the number of air hole rings. The ratio d/Λ is called the filling factor and represents the proportion of air present in the cladding. The holes of air can be arranged in various patterns, such as triangular, rectangular, circular, octagonal, hybrid, etc. The core, often described as a structural defect, is created by removing one or more air holes, enabling the confinement and guidance of light along the PCF. Fig .4 illustrates an example of cross-sections of a PCF (b) and a conventional fiber (a) [8].

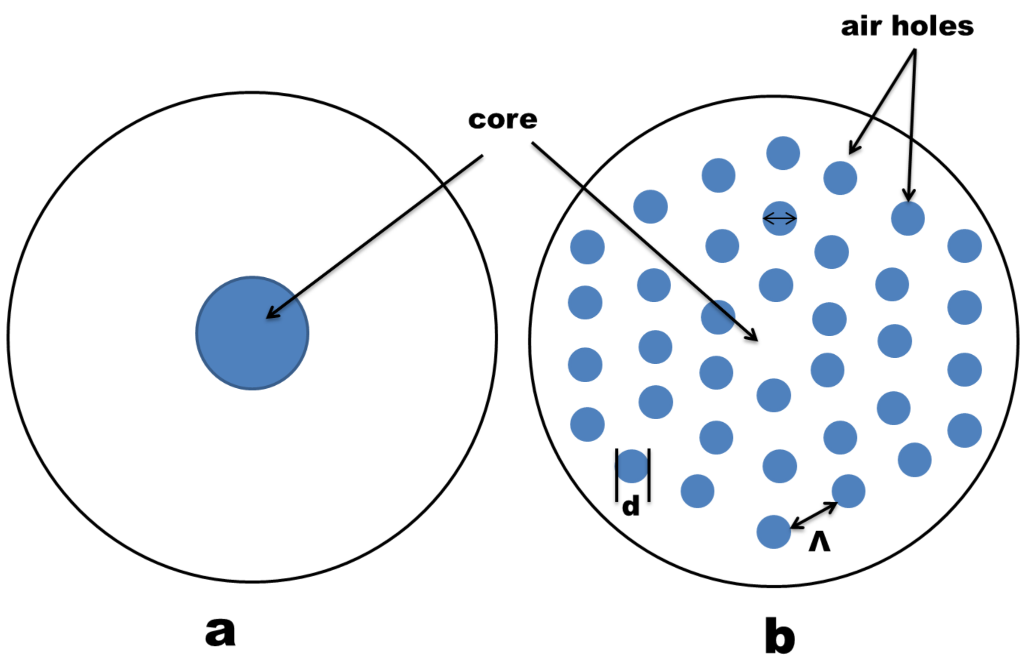

Fig.4. *Transverse cross-section of a conventional fiber (a) and a PCF (b). Adapted from [8].*

4.2 Fabrication of Photonic Crystal Fibers

The fabrication of PCFs is a meticulous process that typically involves the stack-and-draw technique. Initially, thin-walled silica tubes and rods are carefully arranged to create a preform that replicates the desired microstructure of the PCF. This arrangement defines the core and the air hole's structure, ensuring precise geometrical parameters like hole diameter d, lattice pitch Λ, and filling factor. Once the preform is assembled, it undergoes a drawing process in a specialized fiber-drawing tower. During this step, the preform is heated to high temperatures, allowing it to be stretched into a long fiber while maintaining the proportionality and integrity of the microstructure. Advanced control systems ensure uniformity in the fiber's dimensions and optical properties throughout the drawing process. Modifications to the fabrication process can also be introduced to create variations such as hollow-core PCFs or hybrid designs. Techniques like chemical etching or selective material removal may be employed to refine the microstructure further. To fabricate photonic crystal fibers (PCFs) with optimal precision, the following conditions must be met [8].

1- The silica must be well dehydrated and of very high purity, with minimal roughness at the silica/air interfaces.
2- Accurate control of the parameters d and Λ is essential, as the optical characteristics of PCFs are highly sensitive to their values.
3- The PCF's cross-section must be axially maintained to minimize transmission losses.

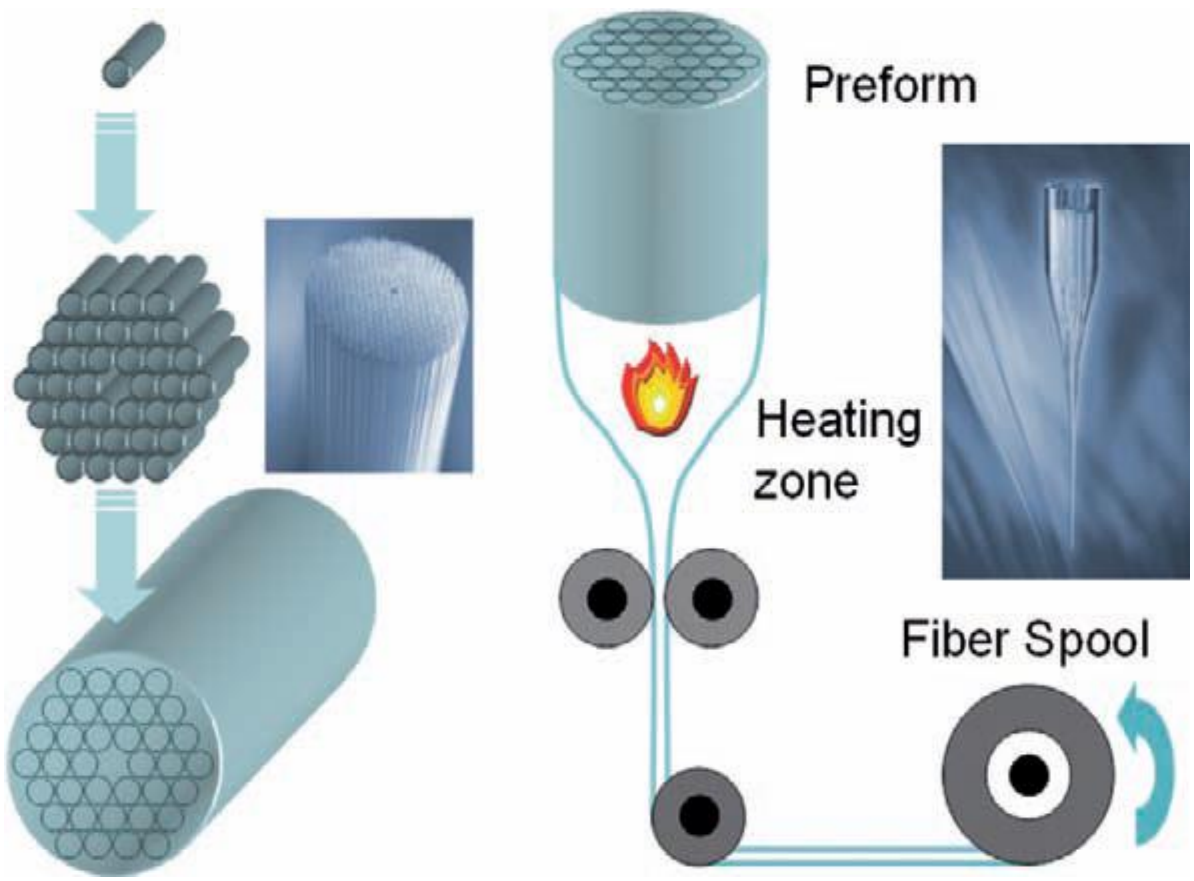

***Fig 5**. The PCF fabrication methodology. Reproduced from [6].*

4.3 Mechanisms in Photonic Crystal Fibers

Photonic crystal fibers (PCFs) guide light through two primary mechanisms:

4.3.1 Photonic Band gap Guiding Mechanism:

This mechanism is unique to certain types of PCFs, particularly hollow-core fibers. Instead of relying on a greater core refractive index, light is confined in a less-index (or air-filled) core by the effect of band gap photonic. The periodic arrangement of air holes in the cladding creates a photonic bandgap that forbids the propagation of particular wavelength ranges in the cladding, thereby confining the light within the core [9].

4.3.2 Index-Guiding Mechanism:

In this mechanism, the PCF behaves similarly to conventional optical fibers, … in which light is guided through a solid core possessing a refractive index greater than that of the surrounding cladding. The cladding is made up of air holes, which create an effective refractive index lower than that of the core. Light propagation in the fiber is achieved through total internal reflection at the core–cladding boundary [10].

These guiding mechanisms enable PCFs to exhibit Particular characteristics, example as, wide tunability, endlessly single-mode operation, and low-loss transmission.

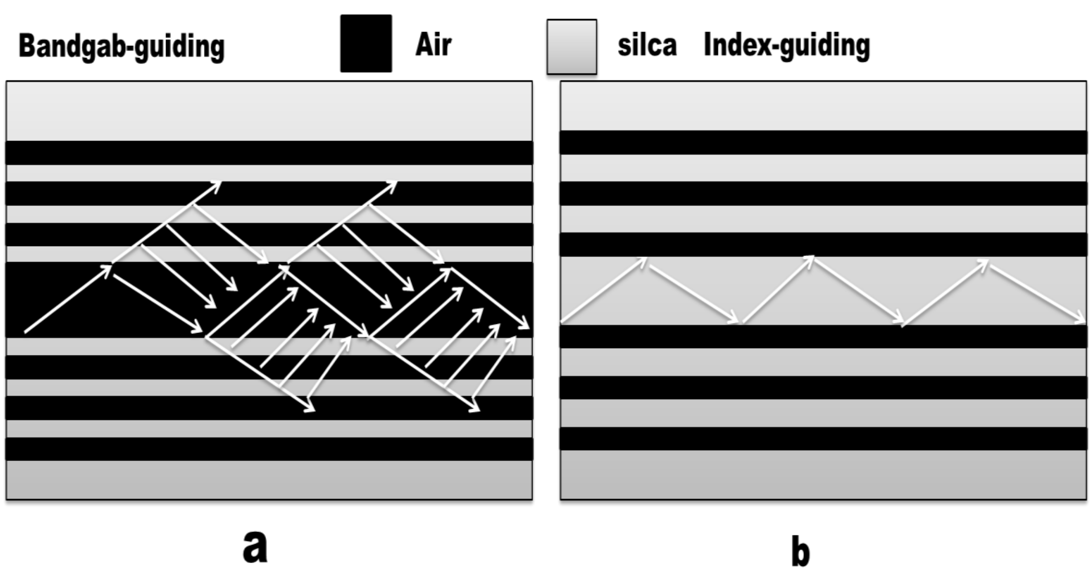

Fig 6. *A PCF's guiding mechanisms: bandgap-guiding(a), index-guiding(b). Adapted from [11].*

4.4 Linear Properties of PCFs

PCFs with a solid-core share many characteristics with conventional step-index fibers. A cladding with an effective refractive index (n_{eff}) lower than the refractive index of the core material is produced by the periodic arrangement of air holes in PCFs. In practice, the effective refractive index of the highest-order mode that can propagate in the core is denoted by n_{eff} , and the principle of total internal reflection is employed in these fibers to guide light. However, A solid-core microstructured fiber has substantially greater light confinement than a step-index fiber. For effective light guidance in the core of PCF, the β (propagation constant) must satisfy condition (2), ensuring that only an evanescent wave exists in the cladding. This condition defines the allowable range of β for maintaining efficient light confinement in the core. If β is less than the cutoff propagation constant of the cladding, the light cannot remain confined in the core and spreads into the cladding [12].

$$kn_{cl} < \beta < kn_c \quad (2)$$

where kn_{cl} denotes the maximum propagation constant permitted in the cladding for effective core guidance, and kn_c represents the maximum propagation constant allowed in the core. Here, n_{cl} and n_c correspond to the refractive indices of the cladding and the core, respectively.

4.4.1 Single-Mode and Multi-Mode PCF:

The guiding characteristics of PCFs are primarily governed by their optical and geometrical characteristics. For instance, in high core index fibers, achieving single-mode propagation across the fiber's transparency range is possible by optimizing the ratio of hole diameter to total cladding area (d/Λ). In conventional step-index fibers, single-mode propagation is characterized by a normalized frequency (V) below 2.405. We apply the same equation (1) for step-index fibers to PCFs, substituting the refractive index of the cladding with the effective index of the photonic crystal fibers cladding. When the ratio of hole diameter to inter-hole spacing (d/Λ) is below 0.4, the fiber can maintain single-mode operation regardless of the wavelength. This enables the creation of broadband single-mode fibers while preserving a large core size. The normalized frequency for PCFs is expressed as follows [13]:

$$V_{eff} = \frac{2\pi a}{\lambda} \sqrt{n_c^2 - n_{eff}^2} \quad (3)$$

where V_{eff} is the normalized frequency, a is the core radius, λ is the propagating light wavelength, n_c represents the refractive index of the material that makes up the core and n_{eff} is the effective index of the microstructure cladding.

4.4.2 Propagation Losses

A wave propagating through an optical fiber is attenuated along its propagation path. Several processes contribute to this attenuation. These processes can be classified into two categories: those related to the material of the core and its manufacturing quality (absorption, scattering), and others related to the cladding's ability to confine the wave within the core (air fraction in the cladding, number of air-hole rings). In the first category, we find electronic absorption, multiphoton absorption, Rayleigh scattering, and Mie scattering. In the second category, we find confinement losses.

4.4.2.1 Absorption Losses

Material absorption can be classified into two categories: intrinsic absorption and extrinsic absorption.

- **Intrinsic Absorption**

This type of loss originates from the interaction between pure silica and light. In this process, an electron within the silica molecule absorbs a photon and undergoes a transition between electronic states. Such electronic resonances occur in the ultraviolet region (λ < 0.4 µm) for silica, with the absorption tail extending into the visible spectrum. Additionally, a photon may interact with a molecule, inducing a change in its vibrational state, which also results in photon absorption and optical power loss. These vibrational resonances take place in the far-infrared region λ > 7 µm, while their absorption tail extends into the near-infrared, as illustrated in Fig. 7 for λ > 1.6 µm [14].

- **Extrinsic Absorption**

This type of loss arises from the interaction between impurities in silica with light. Metallic impurities such as Cu, Fe, Cr, Ni, and V contribute significantly to signal attenuation. However, these impurities can be minimized to concentrations below one part in 1010 using glass-refining methods such as vapor-phase oxidation. Another major source of extrinsic absorption is the presence of water vapor within silica fibers. The OH ion from water vapor becomes bonded to the glass matrix and exhibits a fundamental vibrational resonance at 2.73 μm. Its overtones, along with combination tones involving the fundamental silica vibrational resonances, give rise to strong absorption peaks at 1.38, 1.24, 0.95, and 0.88 μm. As illustrated in Fig. 7, the absorption peak at 1.31 μm is the most pronounced, and its absorption tail around 1.3 μm once posed a major limitation for the advancement of fiber-optic communication systems at this wavelength. Through reduction of water content in the glass, this absorption at 1.31 μm has been lowered to approximately 0.35 dB/km. Consequently, the majority of fiber-optic communication systems are designed to operate within the low-loss and low-dispersion transmission windows centered at 1.3μm and 1.55μm, where the former offers minimal chromatic dispersion in standard single-mode fibers and the latter provides the lowest transmission loss [14].

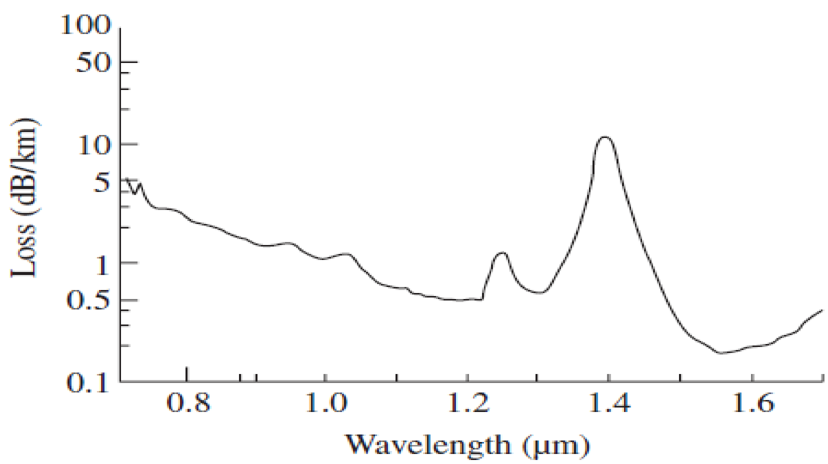

Fig 7. *Loss spectrum obtained for a single-mode fiber. Reproduced from [14].*

4.4.2.2 Scattering Losses

Scattering losses in optical guiding structures arise from the interaction of the material forming the structure with guided light. These losses are classified into two types: linear scattering (elastic), where scattered photons retain the same frequency as incident photons, and nonlinear scattering (inelastic), where scattered photons exhibit frequency shifts. Linear scattering is further divided into Mie scattering and Rayleigh. Rayleigh scattering occurs when the electric field of an incident electromagnetic wave distorts an atom's electron cloud, creating an induced dipole that emits isotropic radiation at the same wavelength as the incident light. The intensity of Rayleigh scattering is inversely proportional to the fourth power of the wavelength ($I \sim 1/\lambda^4$), resulting in higher attenuation at shorter wavelengths. On the other hand, Mie scattering arises from the interaction of guided light with particles whose sizes are comparable to the incident wavelength. It originates from refractive index fluctuations in the core and cladding due to impurities, defects, or inhomogeneities in the glass. The intensity of Mie scattering follows an inverse square relationship with the wavelength ($I \sim 1/\lambda^2$), and improving glass quality can minimize or eliminate this type of scattering [5,15,16].

4.4.2.3 Confinement Losses

Confinement losses, or leakage losses, occur in photonic crystal fibers (PCFs) due to the imperfect confinement of the optical mode within the fiber core. These losses are significant in PCFs because their cladding consists of a periodic arrangement of air holes rather than a homogeneous material, as in conventional optical fibers. The finite cladding structure formed by the air-hole lattice does not create a perfect mirror, allowing some light to leak into the cladding and escape. Additionally, the optical mode extends beyond the core into the air-hole lattice, and this overlap increases for higher-order modes or longer wavelengths, leading to greater interaction with the cladding boundaries and higher losses. Confinement losses are wavelength-dependent, with longer wavelengths resulting in larger mode sizes, increased overlap with the cladding, and thus higher losses [17]. These losses are quantified using the imaginary part of the effective refractive index ($Im(n_{eff})$) and are expressed in dB/km using the formula [18]:

$$L_c = \frac{20}{\ln(10)} \frac{2\pi}{\lambda} Im(n_{eff}) \quad (4)$$

Where L_c : Confinement Loss, $Im(n_{eff})$: Imaginary part of the effective refractive index and λ: Operating wavelength in meters. The result is usually expressed in units of dB/km.

Several factors influence confinement losses in optical fibers. Air-hole size (d) plays a significant role, as larger air holes increase the refractive index contrast, improving light confinement and reducing losses. The pitch (Λ), which refers to the spacing between air holes, also affects the cladding's ability to guide light; optimizing the pitch minimizes leakage. The core design is another critical aspect: a smaller core enhances light confinement but can increase nonlinearity, whereas a larger core reduces confinement but lowers losses. Additionally, the number of air-hole rings in the cladding impacts losses, with more rings effectively confining the mode to the core and reducing losses, albeit at the cost of increased fabrication complexity.

4.4.3 Chromatic Dispersion

An optical waveguide is dispersive when the effective index of its fundamental mode varies with the wavelength. Thus, a pulse propagating through an optical fiber will experience a temporal broadening that depends on its central wavelength and temporal width. Indeed, when a light pulse propagates through a waveguide, the spectral phase associated with each of the wave's spectral components can be expressed as [8]:

$$\varphi(\omega) = \beta(\omega)L \quad (5)$$

Where β is the propagation constant at the carrier frequency $f = \omega/2\pi$, and L is the propagation length.

Since the pulse has a non-zero spectral width around the frequency f_0, we can use the Taylor expansion around the angular frequency ω_0 to express the propagation constant β at frequency ω.

$$\beta(\omega) = \sum_n \frac{\beta^{(n)}}{n!}(\omega - \omega_0)^n \; and \;\; \beta^{(n)} = \left.\frac{\partial^n \beta}{\partial \omega^n}\right|_{\omega=\omega_0} \quad (6)$$

The term β_1 is inversely proportional to the group velocity v_g of the wave, and β_2 corresponds to the derivative (with respect to ω) of the group velocity, also known as the group velocity dispersion (GVD):

$$\beta_1 = \frac{1}{v_g} = \frac{1}{c}\left(n + \omega\frac{dn}{d\omega}\right) \quad (7)$$

$$\beta_2 = \frac{1}{c}\left(2\frac{dn}{d\omega} + \omega\frac{d^2n}{d\omega^2}\right) \quad (8)$$

In the field of optical fibers, the term chromatic dispersion (D_c) is more commonly used, expressed in ps/(nm.km), and is given by:

$$D_c = -\frac{2\pi c}{\lambda}\beta_2 \quad (9)$$

Chromatic dispersion results from the contribution of two sources: material dispersion and waveguide dispersion:

$$D_c = D_m + D_g \quad (10)$$

The material dispersion is given by:

$$D_m = -\frac{\lambda}{c}\frac{d^2 n}{d\lambda^2} \quad (11)$$

Where n is the refractive index of the material is described by the Sellmeier formula, which is given as:

$$n = 1 + \sum_j \frac{A_j \lambda^2}{\lambda^2 - \lambda_j^2} \quad (12)$$

where λ is the wavelength. A_j and λ_j are the Sellmeier coefficient of material. And the waveguide dispersion, its expression is given by:

$$D_g = -\frac{\lambda}{c}\frac{d^2 n_{eff}}{d\lambda^2} \quad (13)$$

Dispersion can be classified into two types based on the sign of the group velocity dispersion (GVD) parameter: normal and anomalous. When $\beta_2 > 0$, it is referred to as normal dispersion, where the low-frequency (red-shifted) components of an optical pulse propagate faster than the high-frequency (blue-shifted) components. Conversely, in anomalous dispersion, which occurs when $\beta_2 < 0$, the opposite behavior is observed. The wavelength at which $\beta_2 = 0$ is termed the zero-dispersion wavelength (ZDW). However, at the ZDW, dispersion effects do not vanish entirely. As a result, it becomes essential to account for the β_3 parameter($\beta_3 = \frac{\partial^3 \beta}{\partial \omega^3}$), known as the third-order dispersion (TOD) parameter, in the relevant equations. This parameter plays a critical role in pulse propagation near the ZDW by causing asymmetric pulse broadening. Additionally, third-order dispersion significantly influences supercontinuum (SC) generation by introducing perturbations to the stability of solitary waves, or solitons, leading to their break-up and the formation of resonant radiation known as dispersive waves (DW) [20]. In photonic crystal fibers (PCFs), dispersion characteristics can be engineered with remarkable flexibility. Owing to the large refractive index contrast between silica and air, together with the design versatility offered by varying the dimensions and arrangements of air holes, PCFs enable access to a significantly wider range of dispersion profiles compared to conventional optical fibers. [6].

4.4.4 Birefringent

Birefringent fibers are single-mode fibers in which two orthogonally polarized modes propagate at different velocities, enabling the preservation of polarization states in optical systems and components. Such birefringence can be induced when the fiber core is intentionally designed with a twofold symmetric structure, for instance, by incorporating air capillaries of unequal wall thickness above and below the core region. A slight modification of the air-hole geometry allows the achievement of birefringence levels that surpass those of conventional birefringent fibers by up to an order of magnitude. It is worth noting that, unlike standard polarization-maintaining fibers such as Panda, bow-tie, or elliptical-core designs, which typically rely on two glasses with distinct thermal expansion coefficients, the birefringence in photonic crystal fibers (PCFs) is largely insensitive to temperature variations, a property of particular relevance for many practical applications. An illustration of the cross-section of a highly birefringent PCF is presented in Fig. 8. [6].

Birefringence B is the absolute difference between the effective refractive indices of the x- and y-polarized modes at a specific wavelength. The refractive index of the material, which varies with the polarization and propagation direction of the signal, determines it. You can calculate the birefringence of the PCF using the following expression [21]:

$$B = \left|Re\left\{n_{eff}^{x} - n_{eff}^{y}\right\}\right| \quad (14)$$

Here, n_{eff}^{x} and n_{eff}^{y} denote the effective refractive indices of the x- and y-polarized modes, respectively. In our simulation, the fundamental x- and y-polarized modes exhibit a significant refractive index difference, attributed to the presence of small circular air holes within the core.

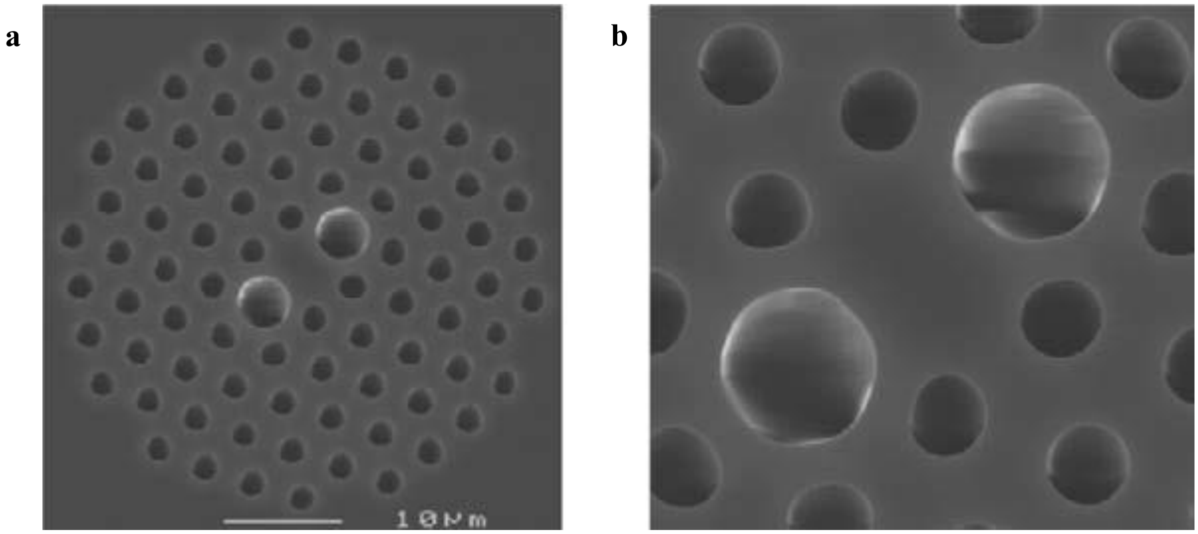

Fig 8. *shows a microscopy of a highly birefringent triangular PCF's (a) cross-section and (b) core region. Reproduced from [6].*

4.4.5 Effective area (A_{eff})

The effective area (A_{eff}) of an optical fiber represents the region over which the electric field E (x, y) is distributed. In optical fibers, A_{eff} serves as a measure of the light intensity or energy the fiber can transmit without inducing significant nonlinear effects. This parameter is crucial for determining the nonlinear phase shift and plays a vital role in evaluating factors such as numerical aperture, nonlinearity, leakage loss, and macro-bending losses. The effective area can be tailored by adjusting the pitch size, air filling fraction, and the number of air-hole rings, while considering the operating wavelength. It is mathematically defined as [22]:

$$A_{eff} = \frac{(\iint |E(x,y)dxdy|)^2}{\iint |E(x,y)|^4 dxdy} \, [\mu.m^2] \quad (15)$$

The value of A_{eff} varies depending on the type of fiber, it based on fiber's refractive index profile and the input wavelength.

4.5 Applications of Photonic Crystal Fibers (PCFs):

Photonic Crystal Fibers (PCFs) represent a groundbreaking advancement in optical fiber technology, offering unique properties that distinguish them from conventional optical fibers. Their distinctive microstructured design, typically incorporating periodic air holes running along the fiber's length, allows for precise control over the fiber's optical characteristics. This enables a wide range of applications across various industries. The table 2 provides an overview of some key applications of PCFs, highlighting their versatility and advantages in fields such as telecommunications, medicine, sensing, and industrial applications. These fibers are especially useful in scenarios requiring low-loss transmission, dispersion control, and novel guiding mechanisms [23].

Table 2. *Applications and Advancements in Photonic Crystal [23].*

Application Area	Details
PCF-Based Sensors	Applications include temperature, strain, pressure, electric field, bending, biosensors, fluorescence, and gas sensors.
Mid- and Far-IR Guidance	Applications include sensing gases like CH4 and delivery of power using chalcogenide and tellurite glasses.
Terahertz Guidance	PCFs guide terahertz (THz) radiation for applications in imaging, spectroscopy, and communication. Innovations include birefringent PCFs and low-loss designs for polarization-sensitive devices.
PCFs with Written Gratings	Long-period gratings (LPGs) inscribed in PCFs enhance sensing for strain, temperature, and bending. Applications include biochemical sensors and tunable filters.
PCF-Based Probes	Compact lensed PCFs are used in optical imaging systems. They offer high resolution and are applied in dynamic biological visualization and cancer detection.
PCF-Based Lasers and Amplifiers	PCFs improve laser performance with features like large core area and low nonlinearity. Applications include industrial processing, high-power lasers, and random lasers for multi-wavelength emission.
High Power Transmission	PCFs offer superior guidance of high-intensity light with minimal power losses, useful in applications requiring strong light confinement.
Fiber Optic Amplifiers	They are used in amplifiers for high-speed communication systems, where the control over dispersion and losses enhances signal amplification.
Supercontinuum Generation (SC)	Supercontinuum (SC) generation in photonic crystal fibers (PCFs) occurs due to strong nonlinear effects like self-phase modulation, four-wave mixing, and soliton dynamics. PCFs allow tailoring dispersion and nonlinear properties for specific SC applications. SC is used in fields like spectroscopy, biomedical imaging, and metrology.

4.6 Material Selection for PCFs

PCFs are fabricated using a variety of materials, each suited to specific applications based on their optical, mechanical, and nonlinear properties. The primary components of glass are silicon and oxygen, forming oxide-based glasses. Silica-based photonic crystal fibers (PCFs) have been extensively studied over the previous decades. However, conventional PCFs made of silica exhibit significant propagation losses when used at wavelengths beyond 3 μm, making them less suitable for nonlinear applications of mid-infrared like supercontinuum generation. In contrast, soft glasses such as chalcogenide (S, Te, and Se), tellurite (TeO_2), and fluoride (ZrF_4 and AlF_3) offer excellent optical transparency over broader wavelength ranges: 1–16 μm, 0.5–5 μm, 0.4–6 μm, and, respectively. These properties make them attractive alternatives to silica for MIR applications. As shown in Fig 9, Chalcogenide glasses (ChGs) offer a notably wider IR transparency region relative to oxide-based glasses. Moreover, Mid-infrared supercontinuum sources utilizing soft glasses, especially chalcogenides, are essential for applications within the MIR atmospheric windows. This is because their exceptionally high nonlinear indices, which can be up to three orders of magnitude greater than that of silica. Among fluoride glasses, for applications using optical fiber, ZBLAN is the most resilient material.; however, its nonlinear refractive index is relatively low [24].

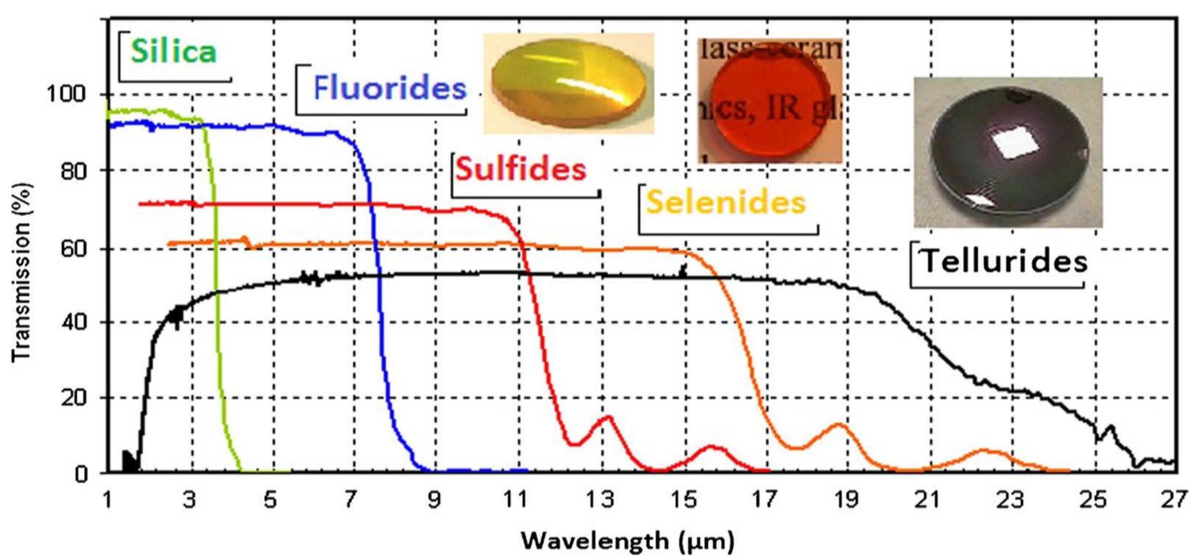

Fig 9. *shows how ChGs transmit light compared to fluoride and silica glasses. Reproduced from [25]*

5. Conclusion

This chapter provided an overview of optical fibers, starting with their fundamental principles and classifications. It covered standard fibers as the backbone of optical communication, followed by photonic crystal fibers (PCFs), which offer unique structural and optical advantages. The fabrication techniques and mechanisms of PCFs, including their linear properties like chromatic dispersion, propagation losses, birefringence, and effective area, were discussed. The applications of PCFs in supercontinuum generation, sensing, and nonlinear optics were highlighted, along with the impact of material selection on their performance.

The next chapter will focus on Nonlinear Optics (Second and Third Order Nonlinearities).

References

[1]. Wetzel, B. Experimental and numerical studies of nonlinear instabilities and optical rogue waves (Doctoral dissertation, University of Franche-Comté). (2012).

[2]. Agrawal, Govind P. "Nonlinear fiber optics." Nonlinear Science at the Dawn of the 21st Century. Berlin, Heidelberg: Springer Berlin Heidelberg, 195-211. (2000).

[3]. Personick, S. Review of fundamentals of optical fiber systems. IEEE Journal on Selected Areas in Communications, 1(3), 373-380. (1983).

[4]. Addanki, S., Amiri, I. S., & Yupapin, P. Review of optical fibers-introduction and applications in fiber lasers. Results in Physics, 10, 743-750. (2018).

[5]. Zhou, X., Chen, Z., Zhou, H., & Hou, J. Mode-field adaptor between large-mode-area fiber and single-mode fiber based on fiber tapering and thermally expanded core technique. Applied optics, 53(22), 5053-5057. (2014).

[6]. Poli, F., Cucinotta, A., & Selleri, S. Photonic crystal fibers: properties and applications (Vol. 102). Springer Science & Business Media. (2007).

[7]. Markos, C., Travers, J. C., Abdolvand, A., Eggleton, B. J., & Bang, O. Hybrid photonic-crystal fiber. Reviews of Modern Physics, 89(4), 045003. (2017).

[8]. Medjouri, A. Study of microstructured optical fibers and their applications to optoelectronic systems (Doctoral dissertation, University of Science and Technology Houari Boumediene. Algeria). (2016).

[9]. Hu, D. J. J., Xu, Z., & Shum, P. P. Review on photonic crystal fibers with hybrid guiding mechanisms. IEEE Access, 7, 67469-67482. . (2019)

[10]. Knight, J. C. Photonic crystal fibres. nature, 424(6950), 847-851. (2003).

[11]. Algorri, J. F., Zografopoulos, D. C., Tapetado, A., Poudereux, D., & Sánchez-Pena, J. M. Infiltrated photonic crystal fibers for sensing applications. Sensors, 18(12), 4263. (2018).

[12]. Mouawad, O. Infrared supercontinuum generation and aging challenges in sulfur-based chalcogenide glasses suspended core highly nonlinear optical fibers (Doctoral dissertation, Université de Bourgogne). (2014).

[13]. Knight, J. C., Birks, T. A., Russell, P. S. J., & De Sandro, J. P. Properties of photonic crystal fiber and the effective index model. JOSA A, 15(3), 748-752. (1998).

[14]. Kumar, S., & Deen, M. J. Fiber optic communications: fundamentals and applications. John Wiley & Sons. (2014).

[15]. Broquet, Irène. Diffusion in multimode optical fibers. Annales des Télécommunications, vol. 29, Springer-Verlag. (1974).

[16]. Jacobsen, A., Neuroth, N., & Reitmayer, F. Absorption and scattering losses in glasses and fibers for light guidance. Journal of the American Ceramic Society, 54(4), 186-187. (1971).

[17]. Zolla, F., Renversez, G., Nicolet, A., Kuhlmey, B., Guenneau, S. R., & Felbacq, D. Foundations of photonic crystal fibres. World Scientific. (2005).

[18]. Singh, S., & Prajapati, Y. K. Highly sensitive refractive index sensor based on D-shaped PCF with gold-graphene layers on the polished surface. Applied Physics A, 125(6), 437. (2019).

[19]. Agrawal, G. P. Applications of nonlinear fiber optics (Vol. 10). Academic press. (2008).

[20]. Ghosh, A. N. Design, modelling, and experiments of mid-infrared supercontinuum generation in soft-glass photonic crystal fibers (Doctoral dissertation, Université Bourgogne Franche-Comté). (2020).

[21]. Arif, M. F. H., & Biddut, M. J. H. Enhancement of relative sensitivity of photonic crystal fiber with high birefringence and low confinement loss. Optik, 131, 697-704. (2017).

[22]. Pandey, S. K., Singh, S., & Prajapati, Y. K. A novel PCF design with an ultra-flattened dispersion and low confinement loss by varying tiny air-hole concentration at core and cladding. Optical Review, 28(3), 304-313. (2021).

[23]. Cerqueira, S. A. Recent progress and novel applications of photonic crystal fibers. Reports on progress in physics, 73(2), 024401. (2010).

[24]. James Raja, S., Jose, T., Charlcedony, R., Sam Paul, M., & Chakravarthi, R. Design of hexagonal chalcogenide photonic crystal fiber with ultra-flattened dispersion in mid-infrared wavelength spectrum. Beni-Suef University Journal of Basic and Applied Sciences, 11(1), 103. (2022).

[25]. Calvez, L. Chalcogenide glasses and glass-ceramics: Transparent materials in the infrared for dual applications. Comptes Rendus. Physique, 18(5-6), 314-322. (2017).

Chapter 2:

Nonlinear Optics (Second and Third Order Nonlinearities)

1. Introduction

Nonlinear optics explores the interaction of intense electromagnetic fields with materials, where the material's response becomes nonlinear, enabling phenomena beyond linear optics. This chapter focuses on second- and third-order nonlinearities, covering their principles, mechanisms, and applications. Key topics include nonlinear optics in fibers, which provide an ideal platform due to their high field confinement and long interaction lengths. The fundamentals of optical nonlinearities are discussed, followed by second-order effects like second harmonic generation (SHG), phase matching, frequency sum and difference generation, and parametric processes. Third-order effects are extensively covered, including self-phase and cross-phase modulation, four-wave mixing, solitons, self-steepening, dispersive waves, and Raman and Brillouin scattering. These phenomena play crucial roles in ultrafast optics, telecommunications, and supercontinuum generation.

2. Nonlinear optics in fibers

In optical fibers, nonlinear propagation began to be studied in the 1970s after the development of silica fiber waveguides with reduced loss. The origin of nonlinearity lies in the refractive index dependence on the optical intensity, and its interplay with fiber dispersion gives rise to a variety of dynamic effects. In the late 1980s, it was understood that dispersion and nonlinearity might interact close to the zero-dispersion wavelength to generate large supercontinuum spectra or balance to support stable soliton propagation. PCF emerged in the 1990s, initially aiming to achieve guidance through the photonic bandgap effect. However, an effective refractive index difference between a solid silica core and a cladding with air-hole microstructures was used in the first practical PCF. Achieving zero-dispersion wavelengths in the visible or near-infrared spectrum, which are far from silica's inherent dispersion value, was made possible by engineering the air-hole geometry. In 1999, experiments with modified PCF demonstrated dispersion shifted near the pump laser wavelength, enabling supercontinuum generation spanning 400–1500 nm using ultrashort 100-fs pulses. Enhanced nonlinearity from tight modal confinement also contributed to these results. Recently, similar concepts have been applied to planar waveguides and non-silica glass fibers, paving the way for novel nonlinear waveguide designs [1].

The propagation of a pulse or electromagnetic (EM) wave is determined entirely by the properties of the medium through which it travels. In a vacuum, the pulse can propagate without alteration. However, when travelling through a medium, the EM field interacts with the medium's atoms, leading to effects such as loss and dispersion. Dispersion arises due to the variation of the refractive index with wavelength, resulting in disparate velocities for various wavelength components of the pulse. These phenomena are referred to as the linear response of the medium. If the pulse intensity is sufficiently high, the medium exhibits a nonlinear response. In this case, Photons can interact with the phonons or molecular vibrations of the medium (the Raman effect), and the refractive index becomes reliant on the intensity of the pulse (the Kerr effect). These nonlinear effects underpin various spectral broadening mechanisms [2].

3. The foundations of optical nonlinearities

The interaction of a dielectric material with an incident electromagnetic wave is primarily governed by the behavior of its outer, weakly bound valence electrons. When subjected to the incident field, the medium develops a polarization p , which in scalar form can be expressed as:

$$p = \epsilon_0 \chi E \qquad (1)$$

where E denotes the electric field, ϵ_0 is the permittivity of free space and χ represents the material susceptibility. When the applied field is sufficiently strong, the electronic response of the medium deviates from linearity. In this regime, the susceptibility χ is expressed through a Taylor series expansion, leading to a polynomial approximation that captures both linear and nonlinear contributions to the polarization.

$$p = \epsilon_0 \sum_n \chi_n E^n \qquad (2)$$

where χ_1 provides the dominant contribution to the polarization p. In materials with inversion symmetry (such as silica), p_2 vanishes because the second-order nonlinear susceptibility χ_2 is equal to zero. χ_3 is the third-order nonlinear susceptibility [3].

4. Second-order nonlinear effects

Second-order nonlinear effects in optics occur when the polarization of a material responds nonlinearly to the applied electric field, typically in materials lacking inversion symmetry. These effects, governed by the second-order nonlinear susceptibility χ_2, include phenomena such as Second Harmonic Generation (SHG), where two photons combine to form one at double the frequency, and Frequency Sum Generation (FSF) and Frequency Difference Generation (GDF), which involve the creation of new frequencies from the sum or difference of two input frequencies. These processes require conditions like coherence length and phase matching for efficient interaction. Additionally, parametric amplification and oscillation allow for the amplification of weak signals, forming the basis for devices such as Optical Parametric Oscillators (OPOs), which generate tunable coherent light.

4.1 Second harmonic generation (SHG)

The frequency doubling process, also widely known as Second Harmonic Generation (SHG), is a second-order nonlinear phenomenon that occurs when an initial optical wave of frequency ω propagates through a nonlinear medium. It involves generating a wave with a doubled frequency, 2ω, from the incident radiation at ω. Its principle is schematically illustrated in Fig. 1. It should be noted that this phenomenon can only occur in non-Centro symmetric materials. For instance, in the particular case of a silica optical fiber of length L, the second-order susceptibility χ_2 is zero [4,5].

Let us consider a laser beam represented by a monochromatic plane wave propagating along the z-axis at a frequency ω in the following form:

$$\tilde{E}(z,t) = E(z)\exp(-i\omega t) + c.c. \tag{3}$$

where $c.c$ denotes the complex conjugate. The second-order nonlinear polarization is given by the following equation:

$$\tilde{P}^{(2)}(t) = 2\epsilon_0\chi^2 EE^* + (\epsilon_0\chi^2 E^2\exp(-i2\omega t) + c.c.) \tag{4}$$

The second-order polarization consists of a zero-frequency contribution (the first term) and 2ω frequency contribution (the second term). The latter contribution is responsible for the phenomenon of second harmonic generation (SHG).

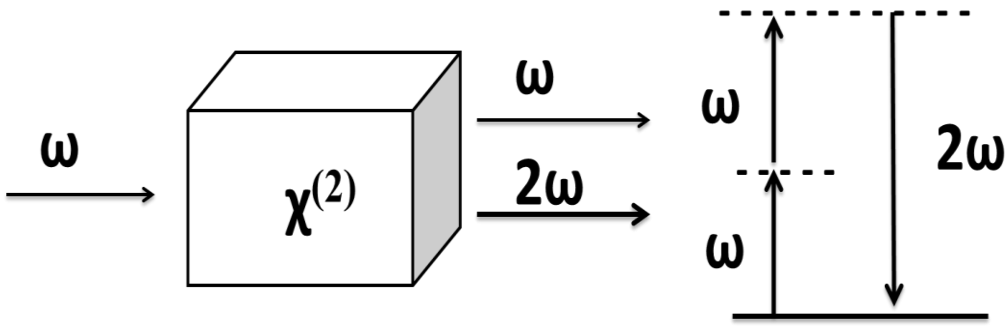

Fig. 1. Principle of Second Harmonic Generation (SHG). Adapted from [4,6]

4.2 Coherence Length

The coherence length L_C in a nonlinear material is the propagation length at which the intensity of the generated second harmonic wave is maximal. This parameter characterizes the phase difference between the free wave and the bound wave and varies with the angle of incidence. It can also be expressed in terms of the wave vector mismatch at ω and 2ω, as follows [7]:

$$\Delta k = k_{2\omega} - 2k_{\omega} \tag{5}$$

$$L_C = \frac{2\pi}{\Delta k} = \frac{\lambda}{4(n_{2\omega} - n_{\omega})} \tag{6}$$

Where n_{ω} and $n_{2\omega}$ represent the refractive indices at the fundamental wave and the generated harmonic wave, respectively.

4.3 Phase Matching

Phase matching is the condition in nonlinear optics in which the interacting waves maintain a constant phase relationship, enabling efficient energy transfer over long propagation distances. This condition ensures that the generated wave remains in phase with the nonlinear polarization, thereby maximizing conversion efficiency in processes such generation (SHG). Phase matching is essential because, in most materials, the refractive indices of the fundamental wave (ω) and the second harmonic (2ω) are different due to dispersion. Without phase matching, the waves fall out of sync, leading to periodic energy exchange between the waves and limiting the overall efficiency. For a plane wave propagating in the z-direction, the electric field of the fundamental wave is given by:

$$E_1 = A_1 cos(\omega t - k_1 z) \qquad (7)$$

Where the angular wave number of the fundamental beam is $k_1 = n_1\omega/c$, and n_1 is the refractive index at ω.

The second-order nonlinear polarization generates the second harmonic:

$$P_2 = \frac{1}{2}\varepsilon_0\chi^{(2)}A_1^2 cos(2\omega t - 2k_1 z) \qquad (8)$$

This polarization acts as the source term for the second-harmonic wave, which propagates as:

$$E_2 = A_2 cos(2\omega t - k_2 z) \qquad (9)$$

where $k_2 = n_2\omega/c$. For efficient energy transfer, the phase relationship must be maintained: $k_2 = 2k_1$. However, due to material dispersion, $n_1 \neq n_2$, resulting in a phase mismatch $\Delta k = k_2 - 2k_1$. This leads to periodic energy exchange between the fundamental and harmonic waves, quantified by the coherence length L_C .In materials with significant dispersion, L_C is typically a few microns, meaning only a small portion of the material contributes effectively to the SHG process.

The solution is to achieve phase matching by modifying the material's properties. For example, birefringent phase matching (BPM) uses crystals like potassium dihydrogen phosphate (KDP) to align the refractive indices such that: $n_{\text{extraordinary}}(2\omega) = n_{\text{ordinary}}(\omega)$. Under phase-matched conditions, the waves remain in phase, allowing consistent energy transfer and significantly enhancing the SHG efficiency, often reaching tens of percent. This development transformed nonlinear optics into a practical field, enabling its application in advanced optical technologies [8].

4.4 Sum and difference-frequency generation

When an optical field with two distinct frequency components,

$$\tilde{E}(t) = E_1 exp(-i\omega_1 t) + E_2 exp(-i\omega_2 t) + c \qquad (10)$$

The interacts with a second-order nonlinear medium, the second-order nonlinear polarization is given by:

$$\tilde{P}^{(2)}(t) = \varepsilon_0 \chi^{(2)} \tilde{E}(t)^2 \qquad (11)$$

the polarization $\widetilde{P}^{(2)}(t)$ can be expressed as:

$$\tilde{P}^{(2)}(t) = \varepsilon_0 \chi^{(2)} [E_1^2 exp(-2i\omega_1 t) + E_2^2 exp(-2i\omega_2 t) + 2E_1 E_2 exp(-i(\omega_1 + \omega_2)t) + 2E_1 E_2^* exp(-i(\omega_1 - \omega_2)t) + c\,] + \varepsilon_0 \chi^{(2)} [E_1 E_1^* + E_2 E_2^*] \qquad (12)$$

The summation includes both positive and negative frequencies ω_n . Consequently, the complex amplitudes corresponding to the different frequency components of the nonlinear polarization are expressed as:

$$P(2\omega_1) = \varepsilon_0 \chi^{(2)} E_1^2\,, P(2\omega_2) = \varepsilon_0 \chi^{(2)} E_2^2 \text{ (SHG)} \qquad (13)$$

$$P(\omega_1 + \omega_2) = 2\varepsilon_0 \chi^{(2)} E_1 E_2 \quad \text{(SFG)} \qquad (14)$$

$$P(\omega_1 - \omega_2) = 2\varepsilon_0 \chi^{(2)} 2E_1 E_2^* \quad \text{(DFG)} \qquad (15)$$

$$P(0) = 2\varepsilon_0 \chi^{(2)} [E_1 E_1^* + E_2 E_2^*] \quad \text{(OR)} \qquad (16)$$

Where SHG refers to second-harmonic generation, SFG denotes sum-frequency generation, DFG denotes difference-frequency generation.

Each frequency contribution of the nonlinear polarization has a corresponding complex conjugate, so it is sufficient to consider only the positive frequency components listed in Eq. (13, 14, 15 and 16). While four distinct frequency components exist in the nonlinear polarization, typically only one will dominate in the generated radiation. This is because efficient output generation requires fulfilling the condition of phase-matching, which is generally satisfied for only one frequency component. In practice, the desired frequency component is selected by adjusting the input radiation's polarization and the orientation of the nonlinear crystal [9].

The nonlinear polarization for SFG is:

$$P(\omega_1 + \omega_2) = 2\varepsilon_0 \chi^{(2)} E_1 E_2 \qquad (17)$$

In SFG, two input waves at different frequencies (ω_1 and ω_2) interact to produce a wave at their sum frequency ($\omega_3 = \omega_1 + \omega_2$). This is often used to generate tunable radiation in the ultraviolet region, combining a fixed-frequency visible laser with a tunable visible laser [9,10].

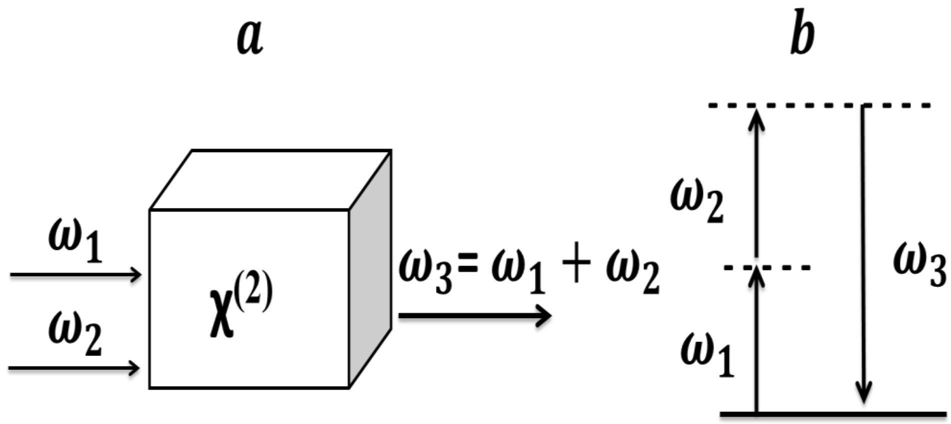

Fig. 2. Sum-frequency generation. (b) Energy-level description. (a) Geometry of the interaction. Adapted from [9].

The nonlinear polarization for DFG is:

$$P(\omega_1 - \omega_2) = 2\varepsilon_0 \chi^{(2)} 2E_1 E_2^* \qquad (18)$$

In DFG, the generated wave has a frequency equal to the difference of the input wave frequencies ($\omega_3 = \omega_1 - \omega_2$). It is utilized to generate tunable infrared radiation by combining a frequency-tunable visible laser with a fixed-frequency laser. Unlike SFG, DFG also amplifies the lower-frequency input field (ω_2). The process is called optical parametric amplification since energy transfer occurs from the higher-frequency wave (ω_1) to the lower-frequency wave (ω_2).

In a photon energy-level diagram: A photon at ω_1 is absorbed, exciting the atom to a virtual level. The atom decays by emitting photons at ($\omega_3 = \omega_1 - \omega_2$) and ω_2.

If ω_2 is not applied externally, weak fields can still be generated via spontaneous parametric down conversion, a process where two photons are emitted spontaneously from a virtual level.

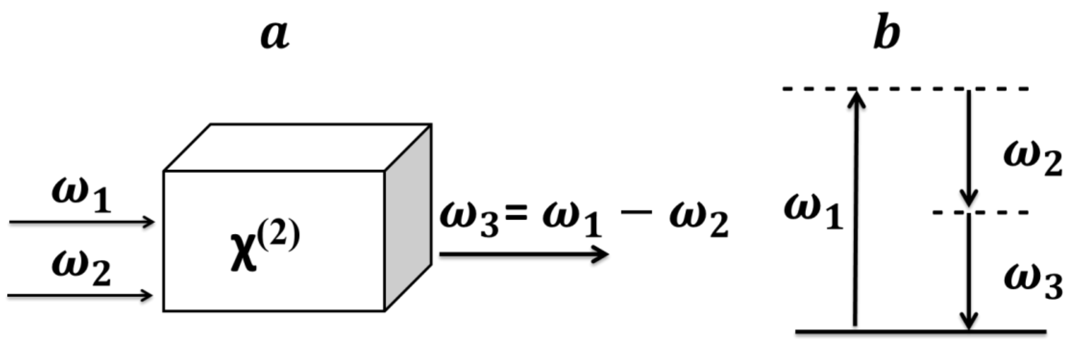

Fig. 3. Difference-frequency generation. Energy-level description(b). Geometry of the interaction(a). Adapted from [9].

4.6 Optical parametric oscillation

In difference-frequency generation, radiation at frequencies ω_2 or ω_3 can trigger the emission of additional photons at those frequencies. When the nonlinear crystal is placed inside an optical resonator, as shown in Fig .4, the ω_2 and/or ω_3 fields can amplify significantly. This setup is called an optical parametric oscillator (OPO), which is an important source of tunable radiation due to its broad tuning range. The device is tunable because any frequency ω_2 smaller than ω_1 can satisfy the condition $\omega_2 + \omega_3 = \omega_3$ for some frequency ω_3. The output frequency of an OPO is controlled by adjusting the phase-matching condition. The input frequency ω_1 acts as the pump, producing the desired signal frequency along with an unwanted idler frequency [9].

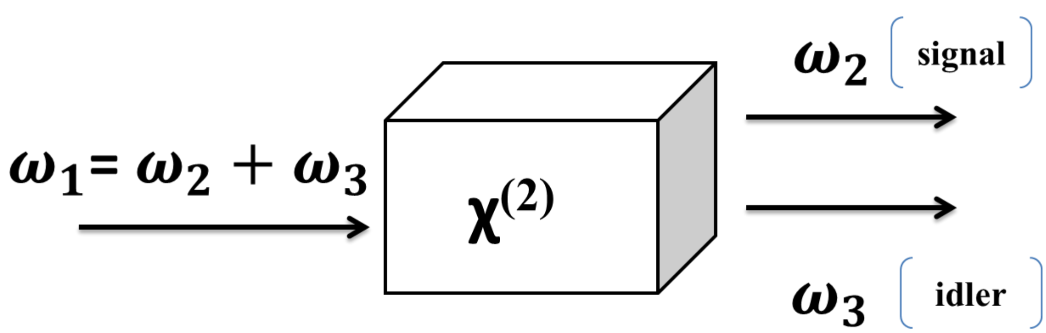

Fig. 4. Optical parametric oscillator. The cavity end mirrors exhibit high reflectivity at frequencies ω_2 and/or ω_3 . The output frequencies can be tuned by adjusting the orientation of the crystal. Adapted from [9].

5. Third-Order Nonlinear Effects

The lowest-order nonlinear phenomena in optical waveguides originate from the third-order susceptibility, including nonlinear refraction, third-harmonic generation (THG), and four-wave mixing (FWM). Among these, processes such as FWM and THG require strict phase-matching conditions to be efficient; otherwise, their contributions are negligible. In contrast, nonlinear refraction results from the intensity dependence of the refractive index and can be expressed as [11]:

$$\tilde{n}(\omega, I) = n(\omega) + n_2 I = n + n_2|E|^2 \qquad (19)$$

where $n(\omega)$ is the linear part which is well approximated by the Sellmeier equation, I *is* the optical intensity related with the electromagnetic field E, and n_2 is the nonlinear index coefficient related to χ_3 by the relation:

$$n_2 = \frac{3}{8n} Re\left(\chi_{3(\chi\chi\chi\chi)}\right) \qquad (20)$$

The analysis considers the optical field to be linearly polarized, in which case only a single component, $\chi_{3(\chi\chi\chi\chi)}$, of the fourth-rank susceptibility tensor contributes to the refractive index. Nonlinear refraction is inherently phase-matched, making it the primary origin of most nonlinear optical effects. These effects include cross-phase modulation (XPM) and self-phase modulation (SPM), both of which are elastic processes. This means that no energy exchange occurs between the the dielectric medium and electromagnetic field during these interactions. In contrast, nonlinear effects arising from inelastic energy exchange between the electromagnetic field and the medium include stimulated Brillouin scattering (SBS)and stimulated Raman scattering (SRS). The fundamental difference between these two processes arises from the nature of the phonons they involve: stimulated Raman scattering (SRS) is associated with optical phonons, whereas stimulated Brillouin scattering (SBS) is governed by acoustic phonons.

The Generalized Nonlinear Schrödinger Equation (GNLSE) is a fundamental tool for studying phenomena of nonlinear in optical fibers, as it models the evolution of optical pulses by incorporating both linear effects (such as loss and dispersion) and nonlinear effects (such as self-phase modulation, four-wave mixing, and cross-phase modulation). It enables accurate simulation of complex dynamics, such as soliton formation and supercontinuum generation, while its flexibility allows the inclusion of higher-order effects like Raman scattering and higher-order dispersion. GNLSE is essential for designing advanced fiber systems, optimizing frequency generation, and enhancing soliton dynamics [11].

5. 1 Nonlinear pulse propagation equation

In order to investigate the various nonlinear effects that arise from the interaction with linear effects during optical signal propagation in waveguides, the evolution of the pulse envelope A along the fiber axis z is described by the generalized nonlinear Schrödinger equation (GNLSE) [2].

$$\frac{\partial \tilde{A}}{\partial Z} = -\frac{\alpha(\omega)}{2}\tilde{A} + \sum_{n\geq 2}\frac{\beta_n}{n!}[\omega-\omega_0]^n\tilde{A} + j\gamma(\omega)\left(1+\frac{\omega-\omega_0}{\omega_0}\right)\times \mathcal{F}\left(\mathrm{A}(z,T)\int_{-\infty}^{+\infty}\mathrm{R}(T)\left|\mathrm{A}(z,T-\tilde{T})\right|^2 d\tilde{T}\right) \qquad (21)$$

where $\mathcal{F}$ denotes the Fourier transform and $\tilde{A}(z,T)$ is the Fourier transform of $\mathrm{A}(z,T)$,

$$\mathcal{F}\{A(z,T)\} = \tilde{A}(z,T) = \int_{-\infty}^{+\infty} A(z,T)\exp[j(\omega-\omega_0)t]\,d\,t \qquad (22)$$

and the pulse envelope $\mathrm{A}(z,T)$ is considered in a retarded time frame $T = t - \beta_1 z$ moving with the group velocity $1/\beta_1$ at the carrier frequency. The dispersion coefficients β_2, β_3, ..., are defined from the Taylor series expansion. $\alpha(\omega)$ is the linear propagation loss. $\gamma(\omega) = n_2\omega_0/[cA_{eff}]$ is the waveguide nonlinear parameter, A_{eff} is the effective area and c is the speed of light in the vacuum. $\mathrm{R}(T)$ is the delayed Raman response and has the form

$$\mathrm{R}(T) = (1-f_R)\delta(T) + f_R h_R(t) \qquad (23)$$

$$h_R(t) = \frac{\tau_1^2+\tau_2^2}{\tau_1\tau_2}\exp\left(-\frac{t}{\tau_2}\right)\sin\left(\frac{t}{\tau_1}\right) \qquad (24)$$

where f_R = 0.031, τ_1 = 15.5 fs, and τ_2 = 230.5 fs are taken as for chalcogenide material.

6.2 Self-phase modulation

Self-phase modulation (SPM) was initially observed as a spectral broadening phenomenon, where the laser spectrum extended above and below its central frequency following self-focusing in a liquid-filled cell. This effect was later explained by Shimizu, who attributed it to phase modulation induced by the intensity-dependent refractive index of the medium. Since this process took place within self-focused filaments, it involved high intensities and faced challenges such as competing nonlinear effects and uncertainties related to the filament size. SPM was later demonstrated without self-focusing or self-trapping and at lower powers by utilizing CS_2-filled glass fibers. However, analyzing the measured frequency spectrum was challenging due to the multimode nature of the liquid-filled fiber and the fact that the 2.5-ps half-width of the optical pulse was comparable to the relaxation time of the nonlinearity in CS_2 [12].

The most fundamental manifestation of nonlinear refraction is self-phase modulation (SPM), wherein the optical field modulates its own phase. This phenomenon arises from the intensity-dependent refractive index of a nonlinear optical medium, known as the Kerr effect, as expressed in Equation (19). For an electric field represented by its complex amplitude:

$$\mathrm{A}(t) = A_0 exp\big(-j\phi(t)\big) \qquad (25)$$

where A_0 is the peak intensity.

The phase of an optical field change by:

$$\phi(t) = (n + n_2|A|^2)k_0L \qquad (26)$$

The intensity dependence results in a nonlinear phase shift, $\phi_{NL}(t)$, which is expressed as

$$\phi_{NL}(t) = \frac{2\pi}{\lambda} n_2|A|^2L \qquad (27)$$

Here, L denotes the propagation distance. Self-phase modulation (SPM) generates new frequency components and induces spectral broadening of optical pulses. This effect originates from the time dependence of the nonlinear phase shift ϕ_{NL}, whereby the instantaneous optical frequency varies across the pulse.

The nonlinear Schrödinger equation (NLSE), considering only self-phase modulation (SPM) while neglecting all other nonlinear effects, can be expressed as:

$$\frac{\partial \mathrm{A}}{\partial z} = j\gamma|A|^2A \qquad (28)$$

Here, dispersive effects are neglected. This formulation is derived under the assumption that the frequency dependence of n_{eff} and A_{eff} can be ignored by considering a purely instantaneous material response, while neglecting both the optical shock effect and propagation losses.

By multiplying with the complex conjugate A^* and adding the conjugate of the resulting expression, it can be shown that the power $P = |A|^2$ remains constant with respect to z. Consequently, the solution for the electric field envelope can be expressed as:

$$\mathrm{A}(z,T) = A(0,T)exp(-j\gamma|A(0,T)|^2z) = A(0,T)exp(j\phi(z,T)) \qquad (29)$$

It follows that the temporal pulse shape, $|A|^2$, remains unchanged during propagation. However, the time-dependent phase shift $\phi(z,T)$ induces a frequency chirp $\delta\omega(T) = -\partial\phi/\partial\mathrm{T}$, which is negative near the leading edge of the pulse and positive near its trailing edge, corresponding to a redshift and a blueshift, respectively. Self-phase modulation (SPM) is typically observed during the initial stages of supercontinuum (SC) generation [11].

Finally, the self-phase modulation (SPM) leads to a broadening of the frequency spectrum of an optical pulse. This spectral broadening remains minimal as long as the peak nonlinear phase shift is below approximately π. However, when the phase shift reaches a few multiples of π, significant spectral undulations begin to appear, as depicted in Fig .5. These results are obtained through numerical simulations carried out using the nonlinear Schrödinger equation, which accurately captures the dynamics of SPM-induced spectral changes [13].

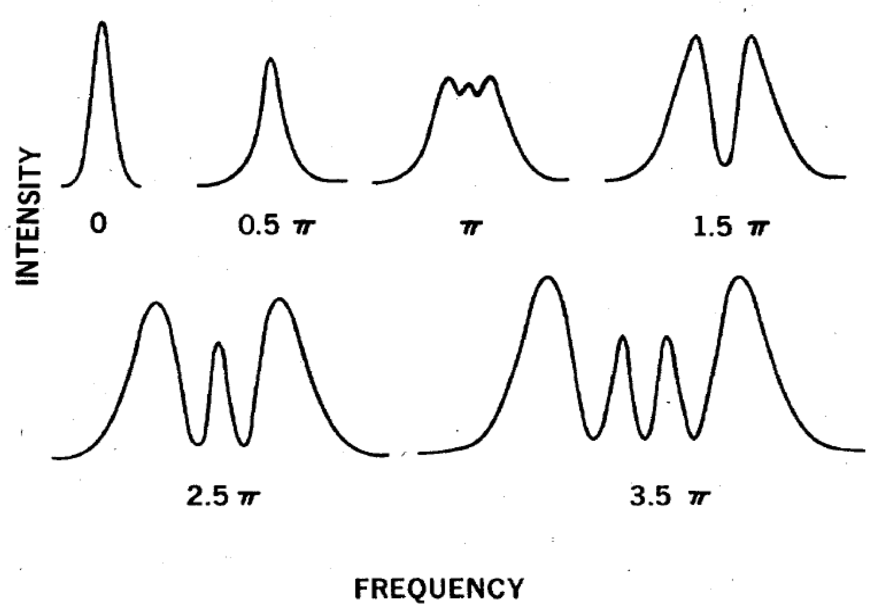

Fig. 5. Frequency spectra calculated for a Gaussian pulse, where the labels indicate the maximum phase shift at the pulse peak. Reproduced from [13].

5.3 Cross-Phase Modulation (XPM)

Cross-phase modulation (XPM) is a nonlinear optical phenomenon that arises when two or more optical pulses co-propagate within a nonlinear medium, such as an optical fiber. The intensity of one pulse induces a refractive index change in the medium, causing a phase shift in the other pulse(s). This effect leads to phenomena like spectral broadening, particularly during Raman or parametric optical pulse amplification. The phase shift ($\Delta\phi$) induced on the signal pulse is proportional to the pump intensity and can be expressed as [14].

$$\Delta\phi(t) = 2A^2 \int sech^2\,(t - t_0 - \beta z)dz \qquad (30)$$

where A^2 is the normalized pump intensity, t_0 is the initial displacement of the pump, and β represents the group velocity mismatch.

The corresponding signal spectrum can be calculated using a Fourier transform,

$$F(\omega) = \frac{1}{\sqrt{2\pi}} \int u_s\,(t) exp\big(i\Delta\phi(t)\big) exp(-i\omega t)dt \qquad (31)$$

where $u_s(t)$ is the signal pulse envelope.

For example, when the pump starts at the trailing edge of the signal pulse and walks through to the leading edge ($t_0 = 2$, $\beta z = 4$), the resulting spectrum exhibits asymmetry with characteristic "wiggles." This demonstrates how XPM modifies the signal's phase and spectrum, a behavior observed in fiber Raman amplification soliton lasers, highlighting the importance of XPM in understanding and controlling nonlinear optical interactions [14].

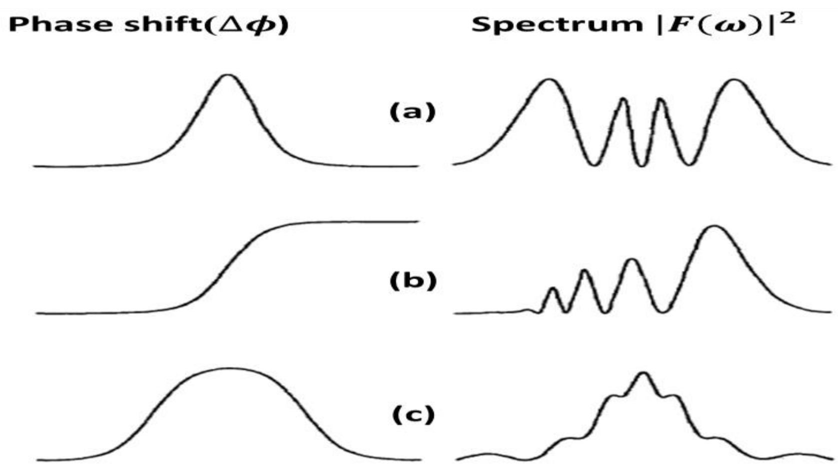

Fig. 6. Phase shifts and spectra corresponding to different degrees of walk-off between the pump and signal pulses. (a) Perfect tracking case ($t_0 = 0$, $\beta = 0, 2A^2 l = 3.5\pi, \alpha = 1$); (b) pump and signal coincide initially, and then pump walks off ($t_0 = 0$, $\beta l = 4, 2A^2/\beta = 3.5\pi, \alpha = 1$); and (c) pump walks from trailing edge of signal to the leading edge ($t_0 = -2$, $\beta l = 4, 2A^2/\beta = 3.5\pi, \alpha = 1$). Reproduced from [14].

5.4 Four-Wave Mixing (FWM)

When a high-power optical signal is introduced into a fiber, the optical response deviates from linearity. Among the resulting nonlinear effects is the optical Kerr effect, which arises from the third-order electric susceptibility. One manifestation of the optical Kerr effect is four-wave mixing (FWM), a phenomenon that occurs when light of two or more different wavelengths propagates through the fiber. Typically, FWM involves the interaction of light at three distinct wavelengths within the fiber, leading to the generation of a new wavelength, referred to as the idler. The idler wavelength is unique and does not coincide with any of the original wavelengths. FWM is often regarded as a form of optical parametric oscillation. [15,16,17].

Non-degenerate four-wave mixing (FWM) is a nonlinear optical process where three distinct frequencies ($\omega_1 \neq \omega_2 \neq \omega_3$) interact within a medium to generate a fourth frequency (ω_4) that satisfies specific frequency-matching conditions ($\Delta k = \beta(\omega_1) + \beta(\omega_2) - \beta(\omega_3) - \beta(\omega_4)$) [18]. Fig II.7 shows two of these four processes along with their interactions and energy level diagrams.

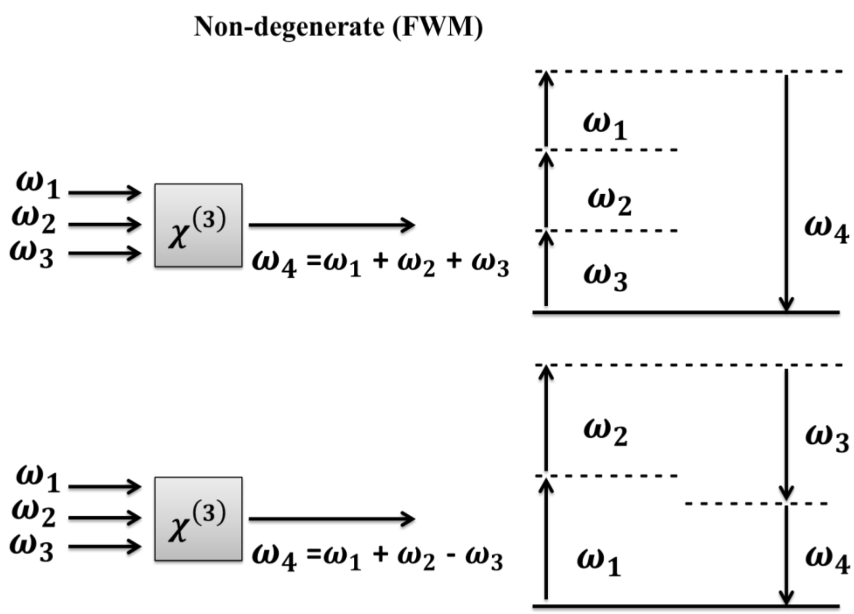

Fig. 7. Non-degenerate four-wave mixing (FWM). Adapted from [18].

The conjugated phase of an incident wave can be generated through degenerate four-wave mixing (FWM). In this process, all three interacting frequencies are identical ($\omega_1 = \omega_2 = \omega_3$), and they interact within a nonlinear medium illuminated by two strong counter propagating pump waves and a signal wave. This interaction results in the creation of a new wave with the same frequency ($\omega = 2\omega + \omega$),, which is the phase conjugate of the original wave. In the special case of dual degenerate four-wave mixing (FWM), where $\omega_1 = \omega_2 = \omega_p$, two frequencies associated with a pump (ω_p) and a weaker signal ($= \omega_s$) generate a third frequency, known as the idler frequency (ω_i), satisfying $\omega_i = \omega_p - \omega_s$. In other words, in degenerate FWM, two pump photons (ω_p) are annihilated to produce two output photons: the signal (ω_s) and the idler (ω_i). Fig. 8 illustrates the interactions and energy level diagrams for both degenerate and dual degenerate FWM processes [18].

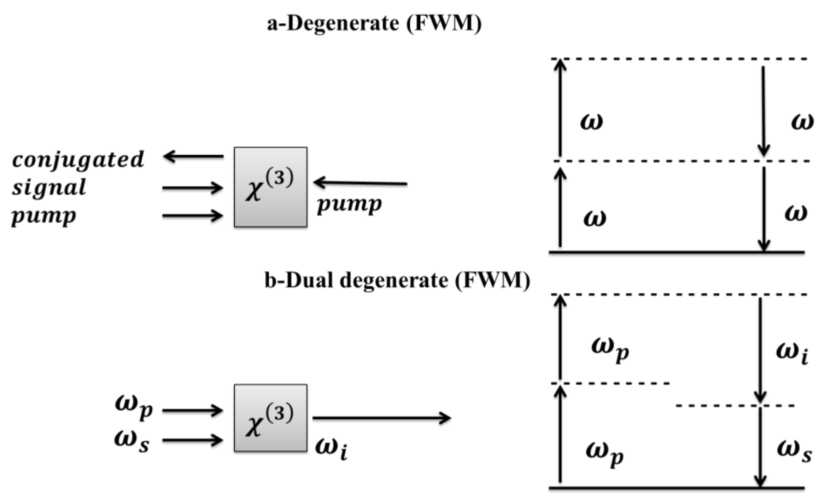

Fig. 8. (b) dual degenerate FWM(a) and Degenerate FWM. Adapted from [18].

5.5 Solitons

In the earlier subsection, it was noted that self-phase modulation (SPM) leads to a red shift at the front of the pulse and a blue shift at its rear. When normal dispersion is also present, the red-shifted portion of the pulse travels faster than the blue-shifted portion. As a result, the pulse broadens in time more rapidly compared to the case where only dispersion is acting. Conversely, in the case of anomalous dispersion, the red-shifted components of the pulse experience a delay, while the blue-shifted components propagate more quickly. Under such conditions, SPM works to mitigate the temporal broadening of the pulse as it propagates in the anomalous dispersion regime [11].

It is possible for group-velocity dispersion (GVD) and self-phase modulation (SPM) to achieve a perfect balance, allowing a pulse to propagate without any change in its shape. By incorporating GVD into the SPM Equation (II.28), the unperturbed nonlinear Schrödinger equation (NLSE) can be expressed as [11]:

$$\frac{\partial A}{\partial z} = -j\frac{\beta_2}{2}\frac{\partial^2 A}{\partial t^2} + j\gamma|A|^2 A \qquad (32)$$

There exists a solution to this equation that corresponds to a pulse which maintains its shape during propagation. This solution is known as the fundamental soliton. It can be derived by assuming a shape-preserving solution of the form $A(z,t) = V(t)exp\big(j\phi(z,t)\big)$ and substituting it into Equation (II.32) [11]. One of its possible solutions is:

$$A(z,t) = \sqrt{P_0}sech\left(\frac{t}{t_0}\right)exp\left[\frac{j|\beta_2|}{2{t_0}^2}z\right] \qquad (33)$$

where the peak power P_0 and pulse width t_0 is adjusted so that $P_0 = |\beta_2|/\gamma {t_0}^2$, and $\beta_2 < 0$ or $D > 0$, indicating anomalous dispersion. The solution of Equation (32) under these conditions corresponds to a fundamental soliton, characterized by the invariance of the power distribution $|A(t)|^2$ during propagation. This behavior arises from the exact balance between group-velocity dispersion (GVD) and self-phase modulation (SPM).

Finally, the order N of a soliton is usually defined based on the dispersion and nonlinear lengths, as follows [19.20].

$$N^2 = \frac{L_D}{L_{NL}} = \frac{\gamma P_0 T_0^2}{|\beta_2|} \qquad (34)$$

From this relationship, the peak power P_0 required to inject a soliton of order N, with characteristic duration T_0, into an optical fiber exhibiting a dispersion β_2 and a nonlinearity γ is deduced.

In the case where N =1, that is, when the dispersion length L_D is equal to the nonlinear length L_{NL}, the linear dispersion effect is compensated by the nonlinear self-phase modulation effect, resulting in the preservation of the wave shape during its propagation. This is referred to as a fundamental soliton (or first-order soliton). When N is greater than or equal to two, they are referred to as higher-order solitons. These can be described as several fundamental solitons propagating in a coupled manner. When higher-order dispersion effects and nonlinear effects (other than SPM) are neglected, the fundamental solitons forming the higher-order soliton travel at the same group velocity, leading to interactions. These interactions produce a periodic behavior of the higher-order soliton during its propagation in the optical fiber. In both the frequency and time domains, the longitudinal evolution of a structure (the pulse envelope) is observed, which may present several peaks and recover its initial form cyclically. The soliton period does not depend on the peak power of the pulse but only on its width and the group velocity dispersion [21,22].

5.6 Self-steepening

Self-steepening is a nonlinear optical phenomenon arising from an intensity-dependent group velocity, leading to temporal distortion and spectral asymmetry in optical pulses. It is modeled by including the first derivative of the nonlinear polarization's slowly varying component in the modified nonlinear Schrödinger equation (NLSE), which extends the standard NLSE to account for effects not explained by self-phase modulation (SPM) and group-velocity dispersion (GVD) alone. Unlike shocks caused by the interplay of SPM and GVD, self-steepening is an inherently asymmetric process that can occur even without GVD, producing sharp edges, often on the trailing side of the pulse. This phenomenon affects soliton behavior in the anomalous dispersion regime, introducing pulse distortion and altering the critical distance for shock formation. The modified NLSE with self-steepening is typically solved numerically, but analytical solutions exist for specific scenarios, making it a valuable model for studying nonlinear pulse propagation in optical fibers and related fields like plasma physics [23] and fluid mechanics [24].

5.7 Stimulated Raman scattering

The Raman effect, first discovered in 1928, gained significant attention starting in 1962 with the discovery of stimulated Raman scattering (SRS). SRS was initially observed in silica fibers in 1972, and by 1981, it enabled the development of fiber-based Raman amplifiers capable of delivering over 30 -dB of gain [25].

Raman scattering is a phenomenon arising from stimulated inelastic scattering. At the fundamental level, it corresponds to the interaction in which an incident photon is scattered by a molecule into a lower-frequency photon, while the molecule undergoes a transition to a higher vibrational energy state. In this process, a photon from the incident pump field is annihilated, giving rise to a lower-frequency photon (Stokes wave) and a phonon that carries the appropriate energy and momentum to satisfy conservation laws [11].

In Stimulated Raman Scattering (SRS), high-order Raman sidebands are generated when a field propagates through an optically polarizable medium. When the pump power exceeds a certain threshold, multiple Stokes frequencies can be produced at the output, including those at $\omega_P - \omega_\nu$, $\omega_P - 2\omega_\nu$, and anti-Stokes frequencies at $\omega_P + \omega_\nu$, $\omega_P + 2\omega_\nu$. If the intensity of the first Stokes wave is sufficiently high, it can generate a "second-Stokes" beam (as shown in Fig II.9). By repeatedly applying this process, higher-order Stokes waves can be generated, leading to the phenomenon known as "cascaded" SRS. The intensity of the ith Stokes order is influenced by the conversion rate from the (i−1) th Stokes order (proportional to gI_iI_{i-1}) and the loss rate to the (i+1) th order (proportional to gI_iI_{i+1}), where g represents the Raman gain of the material. It is important to note that frequency conversion can occur across a wide range of output wavelengths (from visible to ultraviolet) within a single Raman laser system. For example, standard diode-pumped crystalline solid-state lasers can be used to generate multiple Stokes orders through this cascading effect [26].

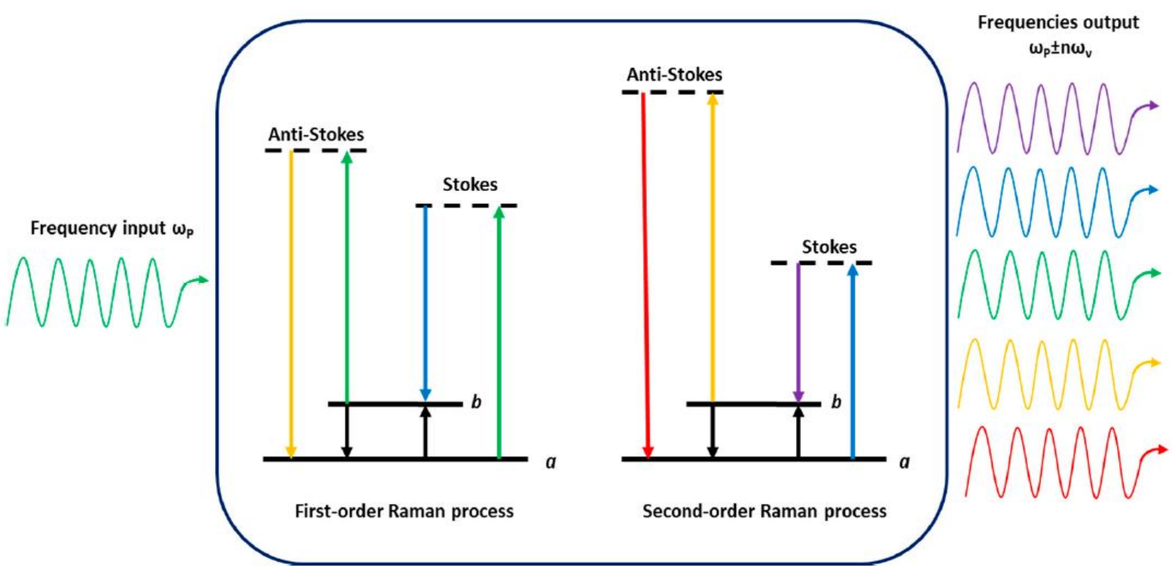

Fig. 9. Cascaded Raman scattering principle. An input frequency ω_P (green) can cause the spontaneous emission of frequencies $\omega_P \pm \omega_\nu$, [Stokes (blue) and anti-Stokes (orange)]. This initial spontaneous event provides the seed photons necessary for subsequent first-order SRS (left). The first-order Stokes and anti-Stokes photons then can cause second-order Raman scattering (right) to produce new frequencies $\omega_P \pm 2\omega_\nu$ (red and violet) and so on through propagation, resulting in a broadband ladder of frequencies $\omega_P \pm n\omega_\nu$. Reproduced from [26].

5.7 Dispersive waves

The emission of resonant dispersive waves (DWs) is a critical mechanism in fiber optics, enabling broadband frequency conversion and extending the spectral range of supercontinuum generation. Traditionally, DW emission was understood as a resonant interaction between a soliton-like pulse in the anomalous dispersion regime and a linear wave, with phase-matching conditions enabling energy transfer. However, recent studies have revealed that DWs can also be generated in the normal dispersion regime without requiring soliton formation. This occurs through phase-matched cascaded four-wave mixing (FWM), where nonlinear interactions in the frequency domain drive the generation of DWs. A key insight is that DWs are always generated across the zero-dispersion wavelength (ZDW), with normal-dispersion pumps exciting DWs directly in the anomalous regime. This phenomenon, described mathematically by:

$$\Omega_{Dv} = -\frac{3\beta_2}{\beta_3} \qquad (35)$$

where Ω_{Dv} represents the frequency detuning of the dispersive wave (DW) relative to the central frequency ω_0 of the input optical pulse, β_2 and β_3 are second- and third-order dispersion coefficients, has been confirmed through numerical simulations and experiments, highlighting its importance for understanding nonlinear fiber dynamics and enhancing optical system performance [27].

Additionally, when a powerful laser pulse propagates in an optical fiber, especially in the anomalous group velocity dispersion (GVD) regime, it often breaks into a combination of solitons and DWs. This process provides valuable insights into soliton physics, including soliton interactions and their interplay with DWs. The development of highly nonlinear photonic crystal fibers (PCFs) and tapered fibers with sub-micrometer core diameters has intensified interest in these phenomena, as such fibers enable supercontinuum generation through femtosecond pulse transformation and spectral broadening. PCFs are particularly effective for converting solitonic pump energy into spectrally narrow bands of resonant radiation or Cherenkov, with mechanisms like exponential amplification observed. While Cherenkov radiation theory has historically explained many spectral features in nonlinear PCFs, recent studies show that soliton interactions with continuous waves (CW) or DWs, including higher-order dispersion effects, can generate additional spectral lines.

Numerical and experimental studies have confirmed these findings, but comprehensive wave-number matching conditions beyond the Cherenkov condition remain underexplored [28].

5.8 Stimulated Brillouin Scattering

The study of stimulated scattering in optical fibers has gained significant interest for several reasons. First, the power levels required to observe nonlinear effects in fibers are much lower than those needed in traditional diffraction-limited cases. Second, the long interaction lengths in fibers allow for the observation of different dynamic behaviors. Nonlinear effects are particularly important for optical fiber communication systems, as they can severely limit the power levels that can be transmitted through a fiber. Previous reports have highlighted efficient low-threshold stimulated Raman scattering (SRS) in both liquid-core and low-loss glass fibers. This letter presents observations of low-threshold stimulated Brillouin scattering (SBS) [29].

Brillouin scattering (SBS), a significant optical effect, involves the interaction of light with acoustic phonons (lattice vibrations). It was theoretically predicted by Léon Brillouin in 1922. In spontaneous Brillouin scattering, a photon from an incident light wave transforms into a scattered photon and a phonon, with the scattered wave experiencing a frequency downshift (Stokes shift). In optical fibers, where light can travel long distances without much attenuation, Brillouin scattering is often undesirable. Stimulated Brillouin scattering (SBS) occurs when the process is strongly dependent on the input pump power, leading to efficient energy conversion from the pump light to the backscattered wave. This effect arises from electrostriction, where the density of the medium changes under the influence of light. The scattered light creates a moving density grating, which results in the backscattering of light. The frequency downshift of the Stokes wave can be explained by the Doppler effect. As the Stokes wave's intensity increases, the interference pattern strengthens, amplifying the acoustic wave, which in turn scatters more light in the backward direction. There are several recent applications that rely on or are related to Brillouin scattering, such as radio-over-fiber technology, slow light, optical delay lines, and high-power lasers [30].

6. conclusion

In conclusion, this chapter has provided an overview of second- and third-order nonlinearities, focusing on their principles, mechanisms, and wide range of applications. Special attention has been given to nonlinear effects in fibers, which serve as an ideal medium due to their high field confinement and long interaction lengths. The chapter explored key second-order effects such as second harmonic generation, phase matching, and parametric processes, as well as third-order effects, including self-phase modulation, four-wave mixing, and various scattering phenomena like Raman and Brillouin scattering. These nonlinear effects are fundamental to technologies in ultrafast optics, telecommunications, and supercontinuum generation. As we transition to the next chapter, the concept of supercontinuum generation will be explored in more detail, building upon the principles and phenomena discussed in this chapter.

References

[1]. Dudley, J. M., & Taylor, J. R. Ten years of nonlinear optics in photonic crystal fibre. Nature Photonics, 3(2), 85-90. (2009).

[2]. Dudley, J. M., & Taylor, J. R. (Eds.). Supercontinuum generation in optical fibers. Cambridge university press. (2010).

[3]. Powers, P. E., & Haus, J. W. Fundamentals of nonlinear optics. CRC press. (2017).

[4]. Shi, L., & Alfano, R. R. (Eds.). Deep imaging in tissue and biomedical materials: using linear and nonlinear optical methods. CRC Press. (2017).

[5]. Stegeman, G. I., & Stolen, R. H. Waveguides and fibers for nonlinear optics. JOSA B, 6(4), 652-662. (1989).

[6]. Zakery, A., & Elliott, S. R. Optical nonlinearities in chalcogenide glasses and their applications (Vol. 135). Springer Science & Business Media. (2007).

[7]. Amber, Z. H., Kirbus, B., Eng, L. M., & Rüsing, M. Quantifying the coherent interaction length of second-harmonic microscopy in lithium niobate confined nanostructures. Journal of Applied Physics, 130(13). (2021).

[8]. New, G. Introduction to nonlinear optics. Cambridge University Press. (2011).

[9]. Boyd, R. Nonlinear optics fourth edition. Academic Press. (2020).

[10]. Sutherland, R. L. Handbook of nonlinear optics. CRC press. (2003).

[11]. G. P. Agrawal, Nonlinear Fiber Optics 5th ed., Academic press, San Diego, California, (2013).

[12]. Stolen, R. H., & Lin, C. Self-phase modulation in silica optical fibers (A). Journal of the Optical Society of America (1917-1983), 66, 1101. (1976).

[13]. Mitschke, F., & Mitschke, F. Fiber opticsand Technology. Springer Berlin Heidelberg. (2009).

[14]. Islam, M. N., Mollenauer, L. F., Stolen, R. H., Simpson, J. R., & Shang, H. T. Cross-phase modulation in optical fibers. Optics letters, 12(8), 625-627. (1987).

[15]. Aso, O., Tadakuma, M., & Namiki, S. Four-wave mixing in optical fibers and its applications. dEp, 1(2). (1999).

[16]. Abed, H. J., Din, N. M., Al-Mansoori, M. H., Fadhil, H. A., & Abdullah, F. Recent four-wave mixing suppression methods. optik, 124(15), 2214-2218. (2013).

[17]. Inoue, K. Four-wave mixing in an optical fiber in the zero-dispersion wavelength region. Journal of lightwave technology, 10(11), 1553-1561. (1992).

[18]. Sirleto, L., & Righini, G. C. An introduction to nonlinear integrated photonics devices: nonlinear effects and materials. Micromachines, 14(3), 604. (2023).

[19]. Mollenauer, L. F., & Gordon, J. P. Solitons in optical fibers: fundamentals and applications. Elsevier. (2006).

[20]. Kivshar, Y. S., & Agrawal, G. P. Optical solitons: from fibers to photonic crystals. Academic press. (2003).

[21]. Dudley, J. M., Genty, G., & Coen, S. Supercontinuum generation in photonic crystal fiber. Reviews of modern physics, 78(4), 1135-1184. (2006).

[22]. Husakou, A. V., & Herrmann, J. Supercontinuum generation, four-wave mixing, and fission of higher-order solitons in photonic-crystal fibers. JOSA B, 19(9), 2171-2182. (2002).

[23]. De Oliveira, J. R., de Moura, M. A., Hickmann, J. M., & Gomes, A. S. L. Self-steepening of optical pulses in dispersive media. JOSA B, 9(11), 2025-2027. (1992).

[24]. Suydam, B. R. Self-steepening of optical pulses. In The Supercontinuum Laser Source (pp. 295-317). New York, NY : Springer New York. (2006).

[25]. Lin, Q., & Agrawal, G. P. Vector theory of stimulated Raman scattering and its application to fiber-based Raman amplifiers. JOSA B, 20(8), 1616-1631. (2003).

[26]. Sirleto, L., & Ferrara, M. A. Fiber amplifiers and fiber lasers based on stimulated Raman scattering: a review. Micromachines, 11(3), 247. (2020).

[27]. Webb, K. E., Xu, Y. Q., Erkintalo, M., & Murdoch, S. G. Generalized dispersive wave emission in nonlinear fiber optics. Optics Letters, 38(2), 151-153. (2013).

[28]. Skryabin, D. V., & Yulin, A. V. Theory of generation of new frequencies by mixing of solitons and dispersive waves in optical fibers. Physical Review E—Statistical, Nonlinear, and Soft Matter Physics, 72(1), 016619. (2005).

[29]. Ippen, E. P., & Stolen, R. H. Stimulated Brillouin scattering in optical fibers. Applied Physics Letters, 21(11), 539-541. (1972).

[30]. Kobyakov, A., Sauer, M., & Chowdhury, D. Stimulated Brillouin scattering in optical fibers. Advances in optics and photonics, 2(1), 1-59. (2009).

Chapter 3:

Supercontinuum Generation

1. Introduction

Supercontinuum production is a nonlinear optical phenomenon distinguished by extensive spectral broadening of intense picosecond or shorter laser pulses during their propagation through a nonlinear medium. Over the past two decades, mid-infrared (mid-IR) supercontinuum generation has attracted significant attention due to its ability to exploit unique absorption bands of various biomolecules within this spectral range [1]. Broadband mid-infrared supercontinuum sources have found applications in numerous fields, including biophotonic detection, flow cytometry, diagnostics, multiplex coherent anti-Stokes Raman scattering (CARS) microscopy, spectroscopy, infrared imaging and optical coherence tomography (OCT) [2]. The formation of the supercontinuum spectrum results from the interplay of several nonlinear optical effects, such as self-phase modulation (SPM), stimulated Raman scattering (SRS), four-wave mixing (FWM) [3], and cross-phase modulation (XPM) [4]. Various optical fiber and waveguide structures have been explored to achieve broadband mid-IR supercontinuum generation. Specialty optical fibers, including microstructured fibers, tapered fibers, and suspended-core fibers in soft glasses such as chalcogenide, ZBLAN, tellurite, and fluoride, have emerged as promising platforms for designing high-brightness, spatially mid-infrared coherent supercontinuum. Among these, tellurite and chalcogenide glasses stand out due to their exceptional transparency (extending up to 20 μm in some compositions), high nonlinear refractive indices, and broad mid-IR transmission windows. For instance, As_2Se_3 chalcogenide glass exhibits outstanding transparency from 0.85 to 17.5 μm, with minimal attenuation, making it an ideal material for mid-IR supercontinuum applications [5]. Recently, Jing Xiao et al. utilized Ge-As-Se-Te (GAST) chalcogenide glasses to achieve supercontinuum (SC) generation. They demonstrated SC spectra extending from 3.5 to 10.5 μm, generated at a pump wavelength of 5 μm, using 150 fs optical pulses in a 19 cm-long double-clad fiber [6].

This chapter explores the Applications of Supercontinuum generation, mechanisms in bulk media, and its implementation in waveguides such as single-mode and multimode fibers. Additionally, it highlights diverse applications of SCG, including spectroscopy, imaging, and sensing. Finally, the chapter discusses numerical modeling, providing insights into the theoretical and computational methods used to analyze and optimize SCG.

2. Applications of Supercontinuum

Supercontinuum sources have significant potential in various fields, including optical coherence tomography (OCT), flow cytometry, multiplex coherent anti-Stokes Raman scattering (CARS) microspectroscopy, nonlinear mid-IR spectroscopy, bio-photonic detection and diagnostics, and infrared imaging [7]. Some of the notable applications of supercontinuum in the spectral range of 2 µm to 20 µm are summarized in Table 1 below.

Table 1: *Applications of Supercontinuum in the Mid-IR [7].*

Category	Applications
Medical	- Optical coherence tomography (OCT), Glucose detection - Monitoring biomarkers in exhaled breath - colon cancer and Diagnostics of ulcers
Environmental	- Atmospheric chemistry studies - Automobile exhaust emission analysis - Greenhouse gas monitoring and fire detection - Volcanic gas emission monitoring
Industrial	- Fence line monitoring of industrial plants - Diagnostics of toxic and harmful gases in the semiconductor industry
Mid-IR Spectroscopy	- Time-resolved spectroscopy for reaction kinetics studies - Environmental and climate process analysis - High-resolution spectroscopy
Security and Military	- Explosive detection, Sensing toxic and harmful gases - Monitoring fugitive emissions from illicit drug manufacturing sites
Photonic Applications	- Optical frequency metrology - Characterization of advanced specialty fiber-optic communications - Development of infrared components based on highly transparent mid-IR materials and Mid-IR light sources (3–12 µm) for LIDAR applications

The media used for generating supercontinuum (SC) can be categorized into several classes. Bulk materials, such as crystals and glasses, were used in early studies but lack the ability to finely control nonlinear effects. Optical fibers, including traditional silica fibers, photonic crystal fibers (PCFs), and hollow-core fibers, provide enhanced control over nonlinearity and dispersion. Hollow-core fibers, when filled with gases or liquids, further enhance nonlinearity, while non-silica fibers, such as chalcogenide and fluoride glasses, extend the SC spectrum into the mid-infrared.

3. Supercontinuum Generation in Bulk Media

The development of supercontinuum (SC) generation in bulk media has been shaped by key discoveries in nonlinear optics. Brewer (1967) identified self-phase modulation (SPM) as the primary mechanism driving spectral broadening [8]. Supercontinuum (SC) generation in bulk media, first discovered by Alfano and Shapiro in 1970, involves the nonlinear propagation of intense ultrashort laser pulses in transparent materials, leading to dramatic spectral broadening. This phenomenon, initially observed as white light generation from picosecond pulses in borosilicate glass, quickly expanded to various other crystals and glasses, establishing its universal nature [9,10].

In 1973, Bloembergen emphasized the role of plasma formation and defocusing in SC generation. His work showed how free-electron plasma formation arrests beam collapse, stabilizing the process and preventing material damage. This finding added a critical layer to understanding SC generation in bulk media [11]. Advances in material science were brought into focus by Brodeur and Chin in 1998, who linked SC generation to the bandgap properties of materials. Their research demonstrated that materials with smaller bandgaps exhibit lower thresholds for SC generation due to free-electron defocusing, significantly influencing the nonlinear dynamics [12]. A unified theoretical framework emerged in 2000 with Gaeta's work, which provided a comprehensive explanation of SC generation. Using three-dimensional simulations, Gaeta confirmed that SC generation in bulk media arises from optical shock formation driven by self-steepening and space-time focusing. His findings consolidated earlier hypotheses and established a robust understanding of the nonlinear processes involved. These contributions collectively shaped the modern understanding of SC generation in bulk media, emphasizing the roles of self-phase modulation, filament dynamics, plasma effects, and material properties. This understanding continues to guide advancements in nonlinear optics and its applications in spectroscopy, imaging, and laser technology [13].

Recently, in 2003, M. Kolesik et all, presented a comprehensive model and computer simulations of supercontinuum generation in bulk media. The study tested the standard model for white-light generation using water and air as representative condensed and gaseous media. The results showed that, in addition to intensity clamping and plasma-induced frequency blue shift, linear chromatic dispersion plays a significant role. It was found to be the key factor determining the achievable spectral extent of the supercontinuum [14]. In 2017, Audrius Dubieti et al, studied femtosecond supercontinuum generation in transparent solid-state media, which involves nonlinear laser pulse propagation leading to spectral broadening. This technique generates coherent broadband radiation across the optical spectrum, with applications in ultrafast science. Recent advances include multioctave generation, spectral control, power scaling, and pulse compression, enabling the creation of few optical cycle pulses for modern ultrafast laser systems [15]. In 2019, Atri Halder et all, developed a numerical framework to analyze coherence in spatiotemporal and spatiospectral domains for supercontinuum (SC) pulses generated in a bulk medium. The study showed that bulk-generated SC pulses exhibit higher degrees of temporal and spectral coherence compared to fiber-generated SC, particularly at higher pump energies. Coherence was lowest at the SC generation threshold in the spatial domain but highest around the optical axis in the far field. The analysis was based on simulations using a 5 mm thick sapphire plate in different group velocity dispersion regimes [16].

4. Supercontinuum Generation in Waveguides

Supercontinuum generation (SCG) can be studied in various types of waveguides, such as single-mode fibers, including conventional optical fibers and photonic crystal fibers (PCFs), as well as multimode fibers (MMFs).

4.1. Supercontinuum Generation in Single-mode fibers (SMFs)

Supercontinuum (SC) generation in optical fibers was first observed in 1976 by Lin and Stolen, using pumping in the normal group-velocity dispersion (GVD) regime of standard silica multimode fibers [17]. Following this, in 1978, R. H. Stolen and Chinlon Lin conducted the first study on frequency broadening due to self-phase modulation (SPM) in single-mode fibers. They found that the spectrum from SPM matched well with theoretical Gaussian pulse calculations and that the nonlinear coefficient was consistent with previous measurements. The study showed that

SPM becomes significant at lower powers compared to the stimulated Raman scattering (SRS) effect, highlighting its importance in high-capacity fiber transmission systems. Additionally, they introduced techniques for analyzing mode-locked laser pulses using fiber measurements [18].

After several years, in 1987, P. Beaude carried out a study on the propagation of 0.83-ps ultrashort dye laser pulses in a single-mode optical fiber, adjusting the input wavelength close to the zero dispersion point of the fiber. Although the power was sufficient to generate high-order solitons, only low-order solitons were observed, and the pulse broke up temporally and spectrally. The result was an ultrashort Stokes pulse, decreasing in frequency as fiber length increases. Numerical simulations of the nonlinear Schrödinger equation, considering the Raman effect and higher-order dispersion, matched the experimental results [19]. Important work by Golovchenko, E. A. in 1991 used numerical simulations to study the development of Raman spectra in single-mode fibers operating in the anomalous group-velocity dispersion regime with continuous-wave pump radiation. With a duration approximately equal to the inverse of the Raman gain linewidth, the study emphasized the importance of the ratio between the pump power and the fundamental soliton power. As this ratio varied, the system produced either a Raman continuum or cascade Raman scattering, the latter featuring discrete Stokes components shifted by $-440\ cm^{-1}$. The investigation also addressed whether a single soliton-like pulse could be extracted from the Raman continuum, which typically appeared as a random sequence of soliton-like pulses in the time domain [20].

The emergence of photonic crystal fibers (PCFs) in the end of the 1990s, they have proven to be superior to traditional optical fibers. These fibers enable endlessly single-mode operation, together with increased index contrast and a larger effective mode area. These advantages make PCFs ideal for various applications, including the generation of broad optical continua, thanks to their unique dispersion properties and high efficiency. In 1999, Ranka et al. provided the first experimental evidence that air–silica photonic crystal fibers are capable of supporting anomalous dispersion within the visible spectral range. By exploiting this property, they succeeded in generating a broad optical continuum with a bandwidth of approximately 550 THz, extending from the violet to the infrared, through the injection of 100-fs pulses with kilowatt-level peak powers into a photonic crystal fiber operated in the vicinity of its zero-dispersion wavelength. This breakthrough in PCFs technology paved the way for new possibilities in generating broad optical continua across a wide spectral range [21]. W. H. Reeves et al., in 2003, carried out an investigation into spectral broadening in photonic crystal fibers (PCFs) exhibiting flat chromatic dispersion, employing 100-fs input pulses. Their findings showed that precise chromatic dispersion control enables exploration of nonlinear effects and significant wavelength shifts in short fibers. The single-mode silica fibers ensured the output remained in the fundamental guided mode. Nonlinear dynamics were captured in the experiment by modeling it with the generalized nonlinear Schrödinger equation (GNLSE). The agreement between experiments and simulations highlighted the potential of PCFs to generate laser light at new wavelengths [22]. In 2006, John M. Dudley made a significant contribution to the field by presenting a comprehensive review of numerical and experimental studies on supercontinuum generation in silica-based photonic crystal fibers, with a focus on single-mode operation across a broad range of regimes, from femtosecond to continuous-wave excitation. Numerical simulations were employed to investigate the temporal and spectral properties of the supercontinuum, providing insights into the fundamental mechanisms underlying spectral broadening. Particular emphasis was placed on femtosecond pulse-driven supercontinuum generation in the anomalous dispersion regime, with detailed discussions on soliton fission, dispersive wave emission, and stimulated Raman scattering. Under varying conditions, phase stability of the supercontinuum spectra and the intensity were also analyzed in the review [23].

A novel chalcogenide glass system (such as As_2S_3, As_2Se_3, Ge–Sb–Se, Ge–As–Se) has garnered significant attention due to its exceptional infrared (IR) transparency, high linear and nonlinear refractive indices, and low phonon energy [24]. These properties have made it a subject of extensive research in areas such as IR optics, nonlinear optics, and IR laser technologies. In particular, waveguides and chalcogenide glass fibers have drawn considerable attention for mid-infrared supercontinuum generation. Shaw et al. (2005) demonstrated the first experimental generation of a broadband infrared SC in PCF based on As-Se. The SC spans from 2.1 to 3.2 um, generated under 2,5 um, 100 fs pumping. This breakthrough illustrated the suitability of As-Se fibers for generating wide spectral ranges in the infrared region [25,26].

This is attributed to their superior nonlinearity and lower transmission losses in the MIR region compared to silica fibers, which are not transparent beyond 2.5 μm. By combining the advantages of chalcogenide glasses with PCFs, the potential for SC generation in the MIR region is significantly enhanced. Generally, the most coherent and spectrally flat SCs in the mid-infrared (MIR) region are highly desirable, as this range encompasses the fundamental vibrational absorption of most molecules, making it particularly valuable for applications such as optical coherence tomography [27]. Due to these exceptional optical properties, numerous studies have emerged focusing on single-mode PCFs with an all-normal chromatic dispersion (ANDi) profile, as shown in the table 2, which highlights some of the works in this field.

Table 2: *Summary of SC generation in single-mode Chalcogenide PCFs with All-Normal Dispersion Profiles*

Study	Material/PCF Type	Pump Parameters	SC Spectrum
Diouf et al. 2017 [28]	AsSe: Hexagonal chalcogenide glass PCF.	3.5 µm, 100 fs, 11.44 kW	10.7 µm
Han et al. 2019 [29]	As_2S_5: Hexagonal chalcogenide glass.	3 µm, 100 fs, 16.8 kW	8.6 µm
Cheshmberahet al. 2021 [30]	$Ge_{11.5}As_{24}Se_{64.5}$: Hexagonal chalcogenide glass PCF.	1.3 µm, 50 fs, 10 kW	1.1 µm
Medjouri et al. 2021 [31]	$Ge_{15}Sb_{15}Se_{70}$ / $Ge_{20}Se_{80}$: Hexagonal all-solid chalcogenide glass PCF	3 µm, 50 fs, 900 pJ	5.4 µm
Xiao et al. 2022 [32]	.$Ge_{11.5}As_{24}S_{64.5}$: Hexagonal chalcogenide glass PCF.	7 µm, 50 fs, 6 kW	9.75 µm
Nguyen et al. 2023 [33]	As_2Se: Hexagonal lattice chalcogenide glass PCF.	5.5 µm, 180 fs, 2.778 kW	5.936 µm,
Tomer et al. 2024 [34]	$AsSe_2$ / As_2S_5: Hexagonal chalcogenide glass PCF.	5 µm, 50 fs, 0.75 kW	10 µm

4.2. Supercontinuum Generation in Multimode fibers (MMFs))

Multimode optical fiber (MMF) is commonly used for short-distance communication, such as campuses, within buildings, or data centers. Its high numerical aperture and large core diameter make it compatible with cost-effective light sources like LEDs and VCSELs, while also supporting low-cost splicing and connectors. However, MMF has lower modal bandwidth than single-mode fiber due to modal dispersion caused by the propagation of multiple modes [35].

Nonlinear optical phenomena in multimode fibers, including modal phase-matching in four-wave mixing (FWM) processes, have been thoroughly investigated for decades. Nevertheless, the control of the spectral and temporal characteristics of ultrashort pulses, in conjunction with the additional degrees of freedom offered by fiber multimodality, represents a relatively recent research direction that has experienced remarkable growth in recent years [36].

Multimode fibers (MMFs) provide a suitable medium for generating supercontinuum (SC) spectra with broad wavelength coverage and high-power throughput. They facilitate the observation of unique nonlinear effects [37,38].

The generalized nonlinear Schrödinger equation (GNLSE) has been effectively modified to examine pulse propagation in multimode fibers, yielding the multimode (MM)-GNLSE. This equation considers the temporal and longitudinal fluctuations of the pulse envelope, integrating linear effects such as attenuation and dispersion, alongside nonlinear effects including self-steepening, cross-phase modulation (XPM), self-phase modulation (SPM), four-wave mixing (FWM), and stimulated Raman scattering (SRS) [39].

Despite limited studies on modeling supercontinuum generation (SCG) in multimode fibers (MMFs), their nonlinear properties remain largely unexplored. Several research groups have conducted investigations into SCG in MMFs. Ramsey et al. studied infrared supercontinuum generation in non-single-moded fibers, such as step-index ZBLAN fibers, using femtosecond upconversion techniques. They found that intermodal scattering into higher-order spatial modes (HOMs) causes spatial and temporal fragmentation of the supercontinuum [40]. Kubat et al. presented a numerical study of mid-infrared supercontinuum in a high numerical aperture multimode chalcogenide step-index fiber. They considered both polarizations of the fundamental mode and higher-order modes (LP11, 21, 02 modes). They observed a spectral broadening of only 5.5 μm when 60 ps input pulses with a 4.8 kW peak power at a 2.9 μm pump wavelength were injected. Additionally, they found that energy was transferred from the fundamental mode to the LP02 mode when long pump pulses (≥ 40 ps) were injected, effectively exciting higher-order modes through Raman scattering and limiting the supercontinuum broadening in the fundamental mode

[41]. Recently, Ben Khalifa et al. investigated mid-infrared supercontinuum generation (SCG) in a multimode As_2Se_3 chalcogenide photonic crystal fiber (PCF). The study analyzed the impact of intermodal nonlinear effects on the propagation of fundamental and higher-order modes. By solving the multimode generalized nonlinear Schrödinger equation (MM-GNLSE), a highly broadband supercontinuum spanning 2 to 11 µm at -20 dB was predicted in both polarizations of the fundamental mode, achieved over just 5 cm of PCF. The findings confirmed that energy transfer occurs only between optically degenerate modes in the mid-infrared region of the multimode chalcogenide PCF [42].

Since the 1990s, a new generation of waveguides with diameters smaller than or equal to the wavelength of transmitted light has emerged, enabling significant advancements toward fully optical integrated circuits at the micrometer scale. These waveguides are classified into two main categories: photonic crystal waveguides, which use the concept of photonic bandgap guidance similar to photonic bandgap fibers, and silica nanowires, which guide light through total internal reflection at the silica/air interface. Both structures offer new opportunities for enhancing nonlinear optical effects, making them essential for next-generation photonic technologies [43].

5. Single-mode SC Generation Modeling

The split-step Fourier method (SSFM) is the most commonly used numerical scheme for solving the GNLSE, as it efficiently separates the integration of dispersive and nonlinear effects. The fourth-order Runge–Kutta in the interaction picture (RK4IP) method also provides high accuracy in solving nonlinear problems [44].

5.1 Split-Step Fourier Method (SSFM)

In the simulation of nonlinear Schrödinger systems, the split-step Fourier method (SSFM) is widely employed compared to other available methods due to its user-friendly nature and time efficiency. Considering one of the simplest NLS-type systems, the equation incorporates terms for higher-order dispersions, loss, and nonlinearity (see Eq. (II.22). To solve Eq. (II.22) using SSFM, the aforementioned equation was reformulated into the following applicable format [45].

$$\frac{\partial A(z,t)}{\partial z} = [L + N]A(z,t) \qquad (1)$$

N and *L* represent the nonlinear and linear components of Equation (II.22), respectively, and are defined as follows:

$$L = -\frac{\alpha}{2}A - \left[\sum_{m=2}^{N} \frac{i^{m-1}}{m!} \beta_m \frac{\partial^m}{\partial \mathrm{T}^m}\right] \qquad (2)$$

$$N = i\gamma \left[|A^2|A + i\frac{1}{\omega_0}\frac{\partial}{\partial \mathrm{T}}(|A^2|A) - R(T)A\frac{\partial}{\partial \mathrm{T}}|A^2|\right] \qquad (3)$$

The following form of the solution has been widely proposed as the final solution for the SSFM. By applying Eq. (2) and (3) to this solution format and using a small spatial step size Δz, the evolution of the propagated pulses along the fiber's z-direction can be described in both the time and frequency domains [45].

$$A(z+\Delta z, T) = exp\left[\frac{\Delta z}{2}L\right] exp\left[\frac{\Delta z}{2}N(z) + N(z+\Delta z)\right] exp\left[\frac{\Delta z}{2}L\right] A(z,T) \qquad (4)$$

It is worth mentioning that this solution is referred to as the symmetrized SSFM, offering second-order accuracy compared to the first-order accuracy of the conventional SSFM solution [45].

5.2 Runge-Kutta in the interaction picture (RK4IP) method

Recently, the RK4IP method has garnered significant attention for its application in modeling soliton propagation, supercontinuum (SC) generation, nonlinear propagation in multimode fibers, and chaotic dynamics in standard fibers. This popularity stems from the method's ability to perform numerical simulations of SC with a fourth-order global error, offering higher accuracy compared to various Split-Step (SS) schemes, such as the simple SS method, full SS method, reduced SS method, Agrawal's SS method, and the Blow-Wood method. Furthermore, the RK4IP method allows for the use of larger step sizes relative to the correlation and beat lengths, making it an efficient and reliable technique for simulating nonlinear propagation in multimode optical fibers [46].

Furthermore, The Runge-Kutta in the Interaction Picture (RK4IP) method is characterized by high numerical accuracy, providing a fifth-order local error O(h^5) and a fourth-order global error(h^4). Generally, the RK4IP method is closely related to the Split-Step Fourier Method (SSFM). In the RK4IP method, the dispersion and nonlinear operators are defined as follows [44,45,47].

$$\widehat{D} = \frac{\alpha}{2}A - (\sum_{n\geq 2} \beta_n \frac{i^{n+1}}{n!}\frac{\partial^n A}{\partial T^n})A \qquad (5)$$

$$\widehat{N} = i\gamma\left(1 + \frac{i}{\omega_0}\frac{\partial}{\partial T}\right) \times \left((1-f_R)A|A|^2 + f_R A\int_0^\infty h_R(\tau)|A(z,t-\tau)|^2 \partial\tau\right) \qquad (6)$$

by transforming A into the Interaction Picture, we can write:

$$A_I = \exp\left(-(z - \grave{z})\hat{D}\right) A \qquad (7)$$

$\grave{z}$ is the separation distance between the standard and interaction pictures. Differentiating (13) gives the evolution of A_I.

$$\frac{\partial A_I}{\partial z} = \hat{N}_I A_I \qquad (8)$$

Where $\hat{N}_I$ is the nonlinear operator in the interaction picture given by:

$$\hat{N}_I = \exp\left(-(z - \grave{z})\hat{D}\right) \hat{N} \exp\left(-(z - \grave{z})\hat{D}\right) \quad (9)$$

with a spatial step h, The RK4IP algorithm advances $A(z,t)$ to $A(z+h,t)$ which is expressed as follows [45]:

$$A_I = \exp\left(\frac{h}{2}\hat{D}\right) A(z+h,t) \qquad (10)$$

$$K_1 = \exp\left(\frac{h}{2}\hat{D}\right)\left[h\hat{N}A(z+h,t)\right]A(z+h,t) \qquad (11)$$

$$K_2 = \mathrm{h}\hat{N}\left(A_I + \frac{K_1}{2}\right)\left[A_I + \frac{K_1}{2}\right] \quad (12)$$

$$K_3 = \mathrm{h}\,\hat{N}\left(A_I + \frac{K_2}{2}\right)\left[A_I + \frac{K_2}{2}\right] \qquad (13)$$

$$K_4 = \mathrm{h}\,\hat{N}\left[\left(\frac{h}{2}\hat{D}\right)(A_I + K_3)\right] \times \exp\left(\frac{h}{2}\hat{D}\right)\left[(A_I + K_3)\right] \quad (14)$$

$$A(z+h,t) = \exp\left(\frac{h}{2}\hat{D}\right)\left[A_I + \frac{K_1}{6} + \frac{K_2}{3} + \frac{K_3}{3}\right] + \frac{K_4}{6} \quad (15)$$

In general, the computational algorithm of The RK4IP method is the most efficient and precise for simulating pulse propagation in optical fibers [47].

5.3 Spectral dynamics broadening of Supercontinuum

The various regimes of supercontinuum (SC) generation can be broadly categorized based on the type of group velocity dispersion (GVD) at the pump wavelength, distinguishing between anomalous and normal GVD, as well as the duration of the pump pulses, ranging from short (sub-picosecond) pulses to long (picosecond, nanosecond, and continuous-wave) pulses [23,48].

1. In the anomalous GVD regime,

The dynamics of supercontinuum (SC) generation can be described in different regimes based on the characteristics of the pump pulses and the group velocity dispersion (GVD).

1. Anomalous GVD with femtosecond pulses: In this regime, spectral broadening occurs in three phases. Initially, the pump pulses undergo spectral broadening and temporal compression as high-order solitons ($N^2= L_D /L_{NL} >1$). This leads to a period of soliton fission, where the pulse breaks into fundamental solitons. The propagation of these solitons generates dispersive wave spectral components due to energy transfer across the zero-dispersion wavelength (ZDW), with resonance causing a narrowband edge in the SC spectrum. Further propagation causes a Raman soliton self-frequency shift, and cross-phase modulation between the generated waves increases the overall bandwidth [49,50].

2. Anomalous GVD with picosecond and nanosecond pulses: When the pulse duration is long and the soliton order is large (N>10), the soliton fission process becomes less significant. Instead, modulation instability (MI) dominates the initial propagation, leading to a breakup of the pulse into sub-pulses. These sub-pulses then undergo further fission, self-frequency shift, and dispersive wave generation. Compared to femtosecond pulses, longer pulses in the anomalous GVD regime result in less spectral broadening, as the initial MI dynamics do not generate sufficient bandwidth for dispersive wave transfer into the normal GVD regime [48].

3. Continuous-wave (CW): In the CW regime, MI develops spontaneously from noise at frequencies that do not overlap with the broadened bandwidth of the propagating pulse. This affects the coherence of the SC. The partial coherence of the pump pulse seeds the breakup, and soliton collisions contribute to reducing the duration of the MI-generated pulses. The interaction of solitons plays an important role in spectral broadening, but the overall coherence is impacted due to the noise-driven MI [48].

For example, by using the Split-Step Fourier (SSFF) method and based on the parameters provided in Reference [23]. Fig. 1 shows numerical simulations of the evolution of an order-N = 1 soliton injected into a PCF fiber, with a pump wavelength λ=835nm, pick power P_0=134w and pulse width T_{FWHM} =50fs considering the integration of the NLSE without perturbations (Raman effect, higher-order dispersion). (a) Temporal evolution. (b) Spectral evolution.

The pulse did not change because the simulation neglects perturbations like Raman scattering and higher-order dispersion, maintaining an idealized balance between nonlinearity (SPM) and dispersion for the soliton [23].

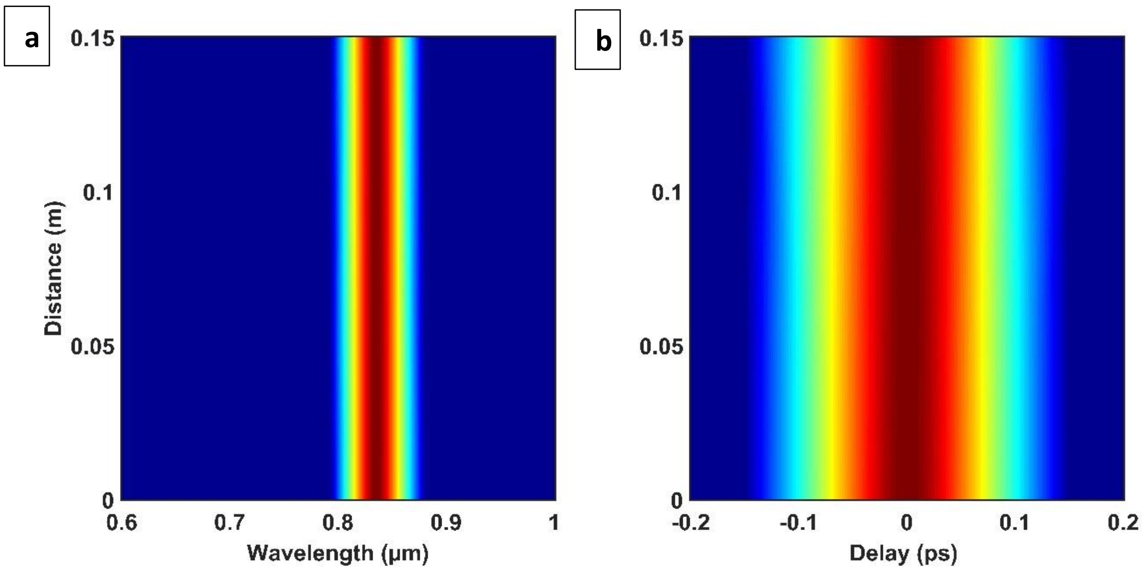

Fig.2: Numerical simulations of the evolution over one period of an order N=1 soliton injected into a PCF fiber. (a) Spectral evolution. (b) Temporal evolution.

Fig. 3 shows numerical simulations of the evolution of an order-N = 3 soliton injected into a PCF fiber, with a pump wavelength λ=835nm, pick power P_0= 1200 w and and pulse width T_{FWHM} =50fs, considering the integration of the NLSE without perturbations (Raman effect, higher-order dispersion). (a) Temporal evolution. (b) Spectral evolution.

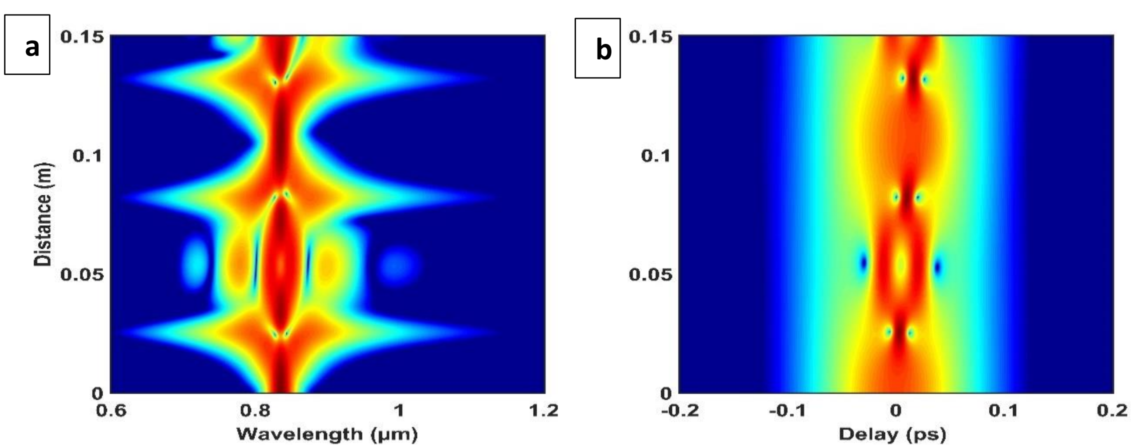

Fig.3: Numerical simulations of the evolution over one period of an order N=3 soliton injected into a PCF fiber. (a) Spectral evolution. (b) Temporal evolution.

In Fig. 3, we note that the higher-order soliton exhibits periodic spectral and temporal evolution over the length of the PCF, with the point of maximum temporal compression of the pulse corresponding to a maximum broadening in the spectral domain, and vice versa.

In the femtosecond regime, the ideal periodic evolution of pulses can be disrupted, leading to pulse breakup via soliton fission, primarily due to Raman scattering and higher-order dispersion. The dominance of either effect largely depends on the duration of the input pulse. For pulses of intermediate duration, (such as 50 fs), both higher-order dispersion and Raman introduce similar perturbations [23].

Fig. 4 shows numerical simulations of the evolution of an order-N = 3 soliton injected into a PCF fiber, with a pump wavelength λ=835nm, pick power P_0= 1200 w and pulse width T_{FWHM} =50fs, considering the integration of the NLSE without perturbations (higher-order dispersion). We note that the spectral broadening towards longer wavelengths is due to Raman perturbations, which arise from the interaction of the optical pulse with the material's vibrational modes, leading to energy transfer from the high-frequency components to the lower-frequency components of the pulse [23].

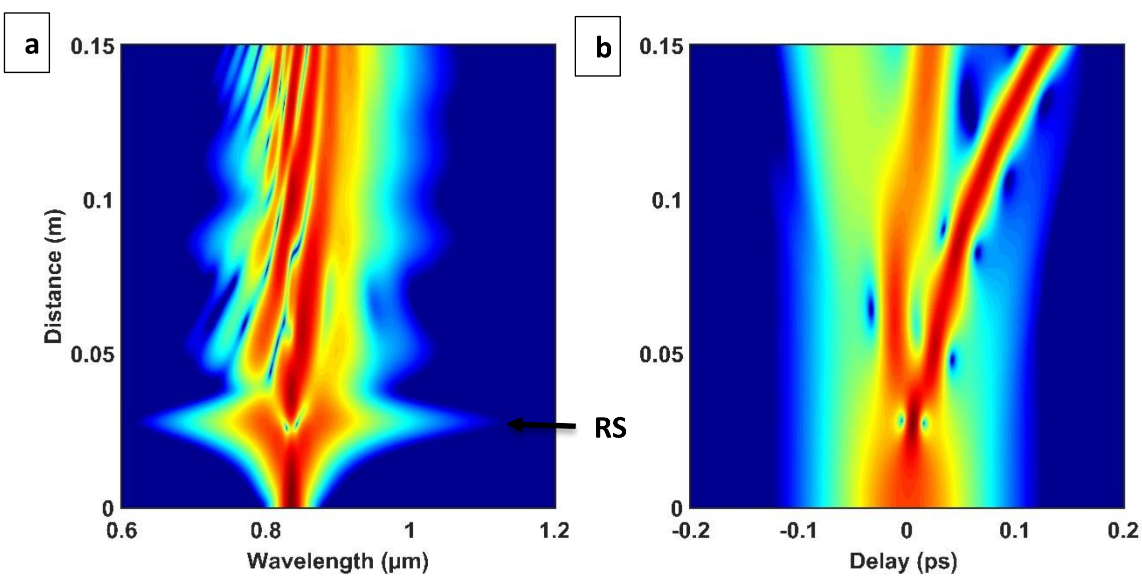

Fig.4: Numerical simulations of the evolution over one period of an order N=3 soliton injected into a PCF fiber without perturbations (higher-order dispersion). (a) Spectral evolution. (b) Temporal evolution.

Fig. 5 shows numerical simulations of the evolution of an order-N = 3 soliton injected into a PCF fiber, with a pump wavelength λ=835nm, pick power P_0= 1200 w and pulse width T_{FWHM} =50fs, considering the integration of the NLSE without Raman perturbations. We note that spectral broadening towards shorter wavelengths is due to higher-order dispersion perturbations.

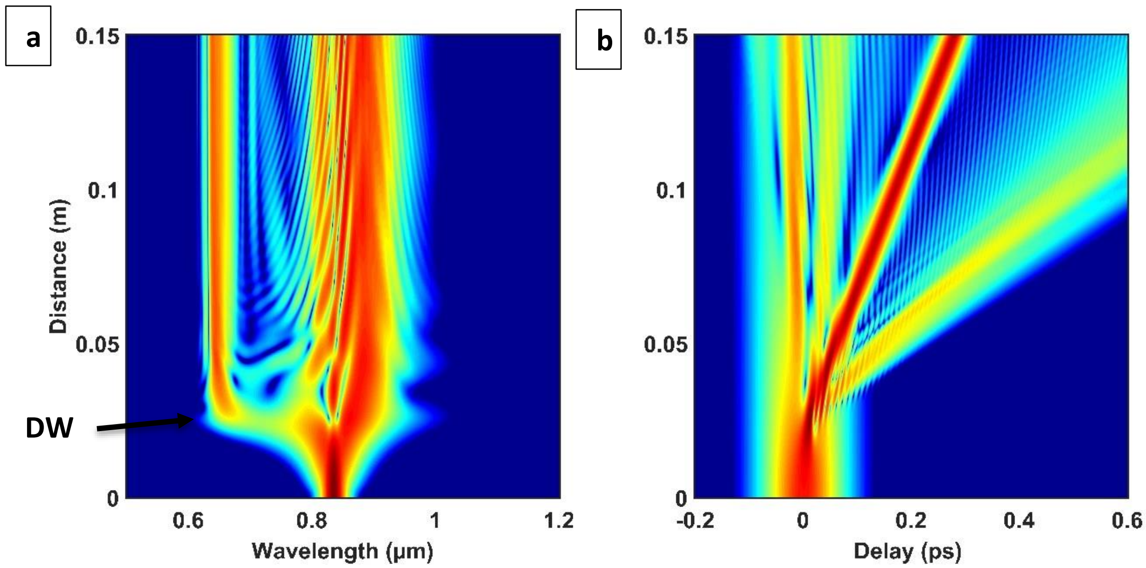

Fig.5: Numerical simulations of the evolution over one period of an order N=3 soliton injected into a PCF fiber without Raman perturbations. (a) Spectral evolution. (b) Temporal evolution.

Supercontinuum generation typically occurs in three stages. First, soliton fission induces the breakup of the initial pulse into several fundamental solitons, which happens when a sufficiently powerful pulse (such as N ≥ 1) propagates in the presence of perturbations, including the Raman effect and higher-order dispersion. Next, dispersive waves (DW) are generated, which are associated with the stabilization of the fundamental solitons ejected during soliton fission. Finally, spectral broadening takes place, resulting from the Raman self-shifting of the solitons (RS) towards longer wavelengths, coupled with the shift of dispersive radiation towards shorter wavelengths shown in Fig.5 [23,48,49]. Fig. 5 shows numerical simulations of the evolution of an order-N = 8 soliton injected into a PCF fiber, with a pump wavelength λ=835nm, pick power P_0= 8540 w and pulse width T_{FWHM} =50fs, considering the integration of the NLSE with Raman perturbations and higher-order dispersion perturbations.

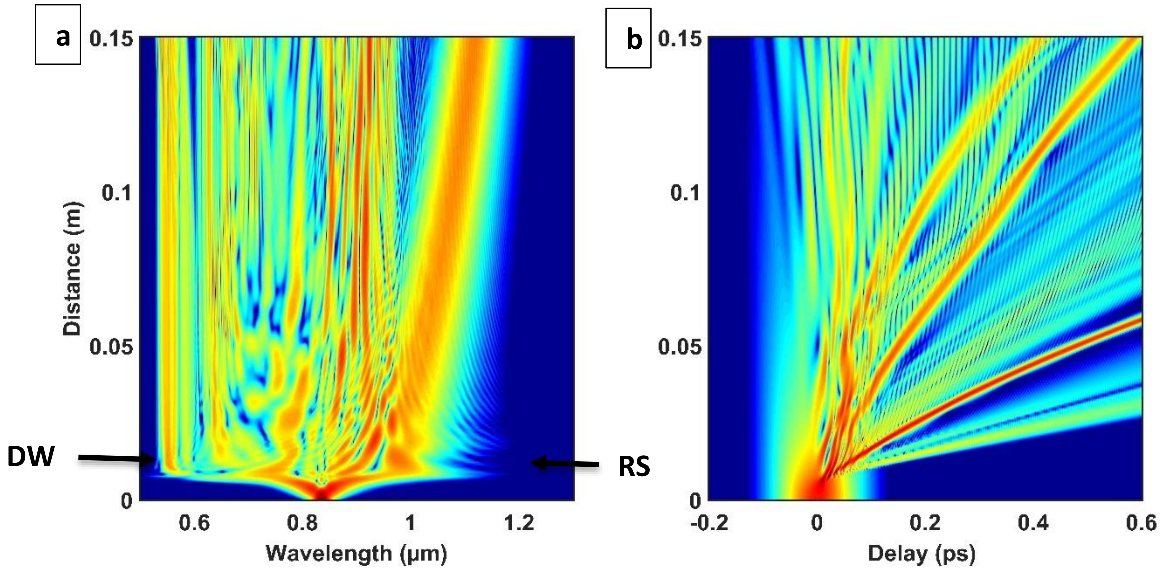

Fig.6: Numerical simulations of the evolution over one period of an order N=8 soliton injected into a PCF fiber with perturbations Raman and higher-order dispersion. (a) Spectral evolution. (b)Temporal evolution.

2. In the normal and all-normal dispersion regime,

In the normal GVD regime, the spectral broadening dynamics for femtosecond pulses are driven by the interaction between self-phase modulation (SPM) and normal GVD of the fiber. Shorter pulses induce greater nonlinear broadening, leading to significant temporal broadening and a rapid decrease in peak power over the first few centimeters of propagation. As a result, the extent of nonlinear spectral broadening is limited. However, for pulses approaching the zero-dispersion wavelength (ZDW), the initial spectral broadening due to SPM transfers spectral content toward the ZDW, which can lead to the involvement of soliton dynamics. In this case, parametric generation and stimulated Raman scattering (SRS) can play a significant role in transferring energy into the anomalous GVD regime, depending on the pumping conditions and fiber properties [48,51].

For picosecond pulses and continuous-wave (CW) radiation, SPM is not as significant, and initial spectral broadening arises primarily from four-wave mixing (FWM) and Raman scattering. When pumping deep into the normal GVD regime, Raman scattering dominates because the parametric sidebands are too detuned from the pump. As the pulse approaches the ZDW, four-wave mixing becomes more important, as parametric gain exceeds Raman gain. When the spectral broadening overlaps with the ZDW, soliton effects can again contribute to the overall dynamics [48].

Supercontinuum generation (SCG) in the all-normal dispersion regime is primarily driven by self-phase modulation (SPM) and optical wave breaking (OWB), enabling the production of spectra with low noise, smoother profiles, and enhanced coherence. However, this approach generally results in a narrower bandwidth and requires higher input pulse energy. Consequently, the realization of SCG spectra that simultaneously exhibit broad bandwidth and high coherence has remained a key focus of research [33]. Table 2 summarizes recent studies on SCG in chalcogenide PCFs with all-normal dispersion profiles.

Highly nonlinear PCFs with (ANDi) characteristics have recently emerged as promising candidates for generating low-noise, octave-spanning SC. However, the fabrication of these fibers presents significant challenges, such as the need for submicron-scale air holes. Additionally, achieving broadband, low-noise SC generation in the ANDi regime requires high-peak-power femtosecond (fs) lasers. It has been demonstrated that low-noise ANDi SC generation is unattainable with long pulses, as the Raman effect is equally as noisy as modulation instability. Despite these challenges, fs-pumped ANDi SC generation has garnered considerable attention due to its capability to produce temporally coherent SC pulses, a feature that is not achievable in the anomalous dispersion regime. This unique attribute makes such systems highly valuable for various applications, including optical coherence tomography (OCT), optical metrology, photoacoustic imaging, and spectroscopy [52].

For example, by using the Split-Step Fourier (SSFF) method to solve the NLSE and based on the parameters of $As_{39}Se_{61}$ chalcogenide photonic crystal fiber (PCF) provided in Reference [53].

Fig.7 shows numerical simulations of the evolution pulse spectral evolution with propagation distance in all-normal dispersion regime with a pump wavelength λ=3500nm, pick power P_0=880w and pulse width T_{FWHM} =50fs.

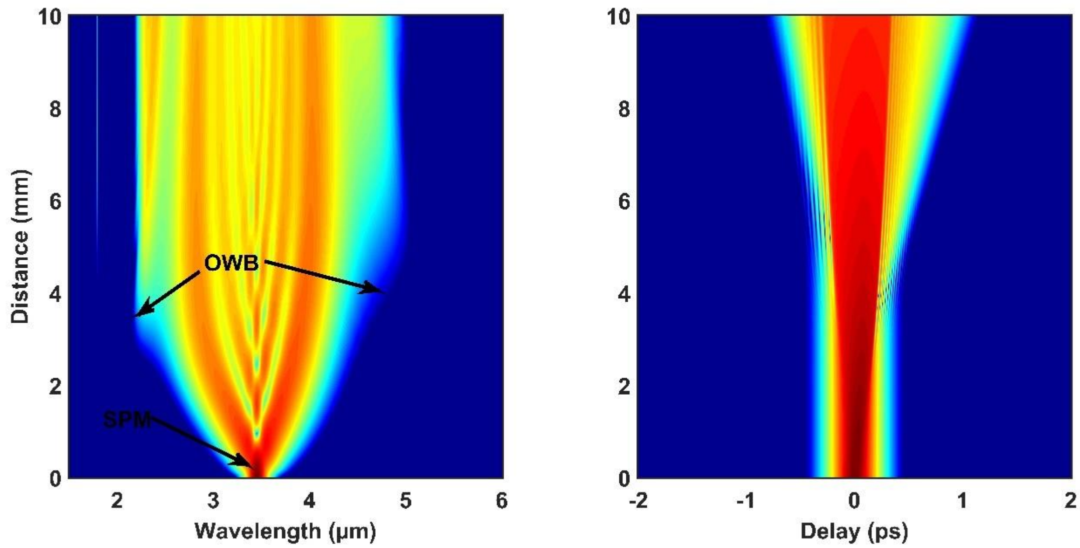

Fig 7: Numerical simulations of the evolution pulse spectral evolution with propagation distance in all-normal dispersion regime with a pump wavelength λ=3450nm, pick power P_0=880w and pulse width T_{FWHM} =50fs.

The spectral evolution of the pulse as it propagates along the length of the photonic crystal fiber (PCF). During the initial stage of propagation, the pulse spectrum begins to expand symmetrically as a result of self-phase modulation (SPM). The dashed line marks the point where the onset of the optical wave breaking (OWB) process occurs. Beyond this point, the pulse spectrum expands further toward both shorter and longer wavelengths, with newly generated spectral components drawing energy from the central part of the pulse spectrum [23,33,53].

6. Multimode SC Generation Modeling

6.1 The multimode generalized nonlinear Schrödinger equation (MM-GNLSE)

The theoretical foundation and key steps involved in the mathematical modeling of optical pulse propagation in multimode fibers are revisited. The multimode generalized nonlinear Schrödinger equation (MM-GNLSE) is utilized, accounting for nonlinear intermodal effects over short fiber propagation lengths. For a given mode p, the full expression of the MM-GNLSE in the presence of M modes is given by [54].

$$\frac{\partial A_p(z,t)}{\partial z} = i\left(\beta_n^{(p)} - \beta_0\right) A_p(z,t) - \left(\beta_1^{(p)} - \beta_1\right)\frac{\partial A_p(z,t)}{\partial t} + i\sum_{n\geq 2}\frac{\beta_n^{(p)}}{n!}\left(i\frac{\partial}{\partial t}\right)^n A_p(z,t) +$$
$$i\frac{n_2\omega_2}{c}\left\{\sum_{l,m,n}\left\{\left(1 + i\tau_{plmn}^{(1)}\frac{\partial}{\partial t}\right) \times Q_{plmn}^{(1)}\, 2A_l(z,t)\int R(t')A_m(z,t-t') \times A_n^*(z,t-t')dt' +\right.\right.$$
$$\left.\left(1 + i\tau_{plmn}^{(2)}\frac{\partial}{\partial t}\right) \times Q_{plmn}^{(2)} A_n^*(z,t) \times \int R(t')A_m(z,t-t')A_n(z,t-t')e^{-2i\omega t'}dt'\right\} = D(z,t) +$$
$$NL(z,t) \qquad (16)$$

The MM-GNLSE consists of a dispersive term $\mathrm{D(z,t)}$, represented in the first and second rows on the right-hand side (where loss is negligible for short pulse propagation lengths), and a nonlinear term $\mathrm{NL(z,t)}$, which includes various effects governed by coupling coefficients. These coefficients define the interaction between mode p and all possible mode combinations l, m, and n are rigorously defined in [55].

$$Q_{plmn}^{(1)}(\omega) = \frac{n_0^2\varepsilon_0^2c^2}{12}\frac{\iint [E_p^*(\omega)E_l(\omega)][E_m(\omega)E_n^*(\omega)]dxdy}{N_P(\omega)N_l(\omega)N_m(\omega)N_n(\omega)} \qquad (17)$$

and

$$Q_{plmn}^{(2)}(\omega) = \frac{n_0^2\varepsilon_0^2c^2}{12}\frac{\iint [E_p^*(\omega)E_l^*(\omega)][E_m(\omega)E_n(\omega)]dxdy}{N_P(\omega)N_l(\omega)N_m(\omega)N_n(\omega)} \qquad (18)$$

with normalization coefficients

$$N_p^2(\omega) = \frac{1}{4}\iint \left[E_p^*(\omega)H_p(\omega)E_p(\omega)H_p^*(\omega)\right]e_z dxdy \quad (19)$$

Where E_p and H_p represent the transverse electric and magnetic field profiles, while e_z denotes the unit vector in the z direction. n_0, n_2, ω_0, c and ε_0 represent, respectively, the linear and nonlinear refractive indices, the central frequency, the speed of light in vacuum, and the vacuum permittivity.

The terms $Q_{pppp}^{(1)}$ and $Q_{pppp}^{(2)}$ govern self-phase modulation (SPM), while the other $Q_{plmn}^{(1)}$coefficients regulate cross-phase modulation (XPM), and the remaining $Q_{plmn}^{(2)}$terms facilitate four-wave mixing (FWM). These terms are considered responsible for energy transfer between modes. It is worth noting that a coefficient $Q_{plmn}^{(1)}$ or $Q_{plmn}^{(2)}$ can be interpreted as an effective area of the nonlinear interaction of mode p with the possible combination of modes l, m, and n. This can be expressed as:

$$A_{eff;plmn} = \frac{1}{2\left(Q_{plmn}^{(1)} + Q_{plmn}^{(2)}\right)} \quad (20)$$

$A_{eff;plmn}$the effective area for a particular mode is defined in [55].

The constants $\beta_0$and $1/\beta_1$ are conveniently chosen to represent the propagation constant and the group velocity of the fundamental mode $p = 1$ at the central frequency ω_0, respectively. For higher-order modes, the propagation constant derivatives are given by

$$\beta_n = \left.\frac{\partial^2 \beta_p(z,t)}{\partial \omega^2}\right|_{\omega=\omega_0} \quad (21)$$

Notably, β_2^p is referred to as the group velocity dispersion (GVD) parameter of mode p.

The shock time constants are defined as [54]:

$$\tau_{plmn}^{(1,2)}(\omega) = \frac{1}{\omega_0} + \left\{\frac{\partial}{\partial \omega} ln\left[Q_{plmn}^{(1,2)}(\omega)\right]\right\} \quad (22)$$

For real-valued E_p, it follows that $Q_{plmn}^{(1)} = Q_{plmn}^{(2)}$ and $\tau_{plmn}^{(1)} = \tau_{plmn}^{(2)}$.

The delayed Raman response $R(t)$ is defined as in Eq. (9) of:

$$R(t) = (1 - f_R)\delta(t) + \frac{3}{2} f_R h_R(t) \quad (23)$$

Where f_R represents the fractional contribution of the Raman response to the total nonlinearity, and $h_R(t)$ is the delayed Raman response function. The function $h_R(t)$ is expressed using the Green's function of a sampled harmonic oscillator:

$$h_R(t) = \frac{\tau_1^2 + \tau_2^2}{\tau_1 \tau_2^2} exp\left(-\frac{t}{\tau_2}\right) sin\left(\frac{t}{\tau_1}\right) \quad (24)$$

Where τ_2 and τ_1 are associated with the bandwidth of the Raman gain spectrum and the inverse of the phonon oscillation frequency, respectively.

6.2 Types of multimode fibers

Multimode fibers encompass a variety of types, each enabling distinct nonlinear effects and offering specific characteristics and advantages. These include graded-index fibers, step-index fibers, and multicore fibers, as well as other types of multimode waveguides to which the GMMNLSE model can be applied [56].

In graded-index (GRIN) fibers, the refractive index varies smoothly across the core, typically following a near-parabolic profile. This structure clusters modes into nearly degenerate groups with minimal intragroup modal dispersion, resulting in significantly lower modal walk-off compared to step-index fibers. Such fibers support strong nonlinear intermodal interactions, even with ultrashort pulses (~100 fs), due to their regular mode spacing and periodic longitudinal field evolution. This has led to phenomena like resonant radiation from multimode solitons and geometric parametric instability. Moreover, the large effective index spacing between mode groups ensures high stability of the fundamental mode, especially in linear regimes [57].

In step-index fibers, the mode structure is less regular than in graded-index (GRIN) fibers, and modal dispersion is typically stronger. These fibers support more spatial modes and are especially suitable for exciting higher-order modes like LP0N, which are resilient to disorder due to their large propagation constant differences. Although step-index fibers have fewer degeneracies and larger mode areas, the effective area of higher-order LP_0N modes decreases with order—unlike in GRIN fibers. Strong modal dispersion makes nonlinear interactions with short pulses more challenging, particularly in the anomalous dispersion regime. So far, observed multimode dynamics have been mostly limited to intermodal four-wave mixing. However, with longer pulses and under normal dispersion, step-index fibers could support a broader range of nonlinear behaviors [56].

Multicore fibers consist of an array of separate cores, which may be single-mode, multimode, graded-index, or step-index. When the cores are closely spaced, the fiber supports "supermodes"—hybrid modes resulting from strong coupling between individual cores. These supermodes exhibit unique dispersion characteristics distinct from those of the individual cores. Multicore fibers offer greater design flexibility, allowing control over dispersion and mode overlap. They can achieve GRIN-like modal dispersion and support strong waveguide dispersion even in low-order modes. In weakly coupled systems, however, supermodes become nearly degenerate and sensitive to structural disorder. Multicore fibers also offer advantages in integration with single-mode fiber systems [58].

Expanding the number of spatial modes is a strategy applicable to various optical waveguide systems to enable novel or improved functionalities. Both solid-core and hollow-core photonic crystal fibers can support multiple modes, with the latter used for phase-matching in unique nonlinear processes—though typically involving only a few modes. Planar and bulk waveguides (e.g., in fused silica or silicon nitride) can also support multimode propagation. Similarly, many microresonators and larger resonators (like Herriot cells) exhibit multimode behavior, an area still under active investigation. Additionally, large-scale rod fibers with oversized claddings offer a platform for studying strongly multimode dynamics. While these rods sacrifice flexibility, this rigidity may enhance environmental stability in multimode systems [56].

Fig. 8 shows modes in multimode fibers. The multimode fibers support up to hundreds of spatial modes. The linearly polarized (LP) modes are described by $F_p(x,y) = \hat{e}_c F_p(x,y)$, where c = x or y for each linear polarization. Although LP modes are commonly labeled using a pair of radial and azimuthal indices (LP01, LP11a, LP11b...), a single-index notation is adopted for clarity and generality, with mode numbering starting from the fundamental mode—the one with the highest propagation constant $\beta = 2\pi n_{eff}/\lambda$. Due to the large number of supported modes, the spatial profile of a multimode beam can become highly complex, resulting from the superposition of the fiber's spatial eigenmodes. Fig. 8(a) shows the intensity distribution $|E(x,y)|^2 = \left|\sum_p^6 \alpha_p \, F_p(x,y)\right|^2$ representing a random combination of the first six supported modes. The corresponding individual mode intensity profiles $\left|F_p(x,y)\right|^2$ are shown in Fig. 8(b). Fig. 8(c) compares the refractive index profiles of step-index and graded-index multimode fibers. Fig. 8(d) presents the propagation constants of the first 25 modes for each fiber type, assuming the same core radius and index contrast. Step-index fibers typically support a greater number of modes with closely spaced propagation constants and effective indices. In contrast, graded-index fibers exhibit distinct mode groups: modes within the same group have nearly identical propagation constants, while different groups are separated by significant mismatches. Fig. 8(e) illustrates additional examples of multimode fiber designs [56].

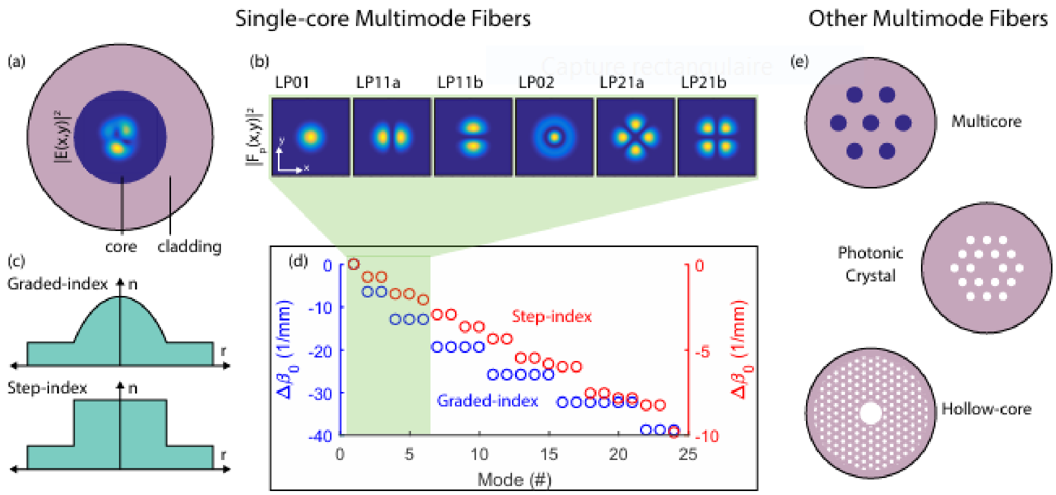

Fig 8: Modes in multimode fiber, Reproduced from [56].

6.3 Solving the MM-GNLSE Numerically

The MM-GNLSE lacks analytical solutions, thus requiring numerical methods, with the split-step Fourier method (SSFM) being the most commonly used, as it offers a good balance between speed, accuracy, and ease of implementation. However, to ensure the accuracy and convergence of the results, an error control technique and an adaptive step-size algorithm were employed. Consequently, the numerical step sizes in the SSFM algorithm along the z coordinate had to be carefully selected [55].

While SSFM remains a widely used technique, alternative numerical approaches have also been explored to enhance the efficiency and accuracy of MM-GNLSE solutions. In this context, Khakimov et al. investigated a different numerical approach by transforming the MM-GNLSE into a system of first-order ordinary differential equations (ODEs), allowing the use of standard ODE solvers to simplify pulse propagation modeling in multimode fibers. The solver was validated in the simplest multimode case, where only two orthogonal polarization states in a non-birefringent microstructured optical fiber were considered. Additionally, the study examined the nonlinear dynamics of the degree and state of spectral polarization in this scenario [59].

To express the MM-GNLSE as a system of first-order ODEs,

$$\frac{dy(z)}{dz} = f(y,z) \quad (25)$$

The temporal pulse shape $A_P(z,t)$ is expressed as the inverse Fourier transform $\mathcal{F}^{-1}$ of its complex spectral envelope $\widetilde{A}_P(z,\omega-\omega_0)$[59]:

$$A_P(z,t) = \mathcal{F}^{-1}\{\tilde{A}_P(z,\omega-\omega_0)\} = \frac{1}{2\pi}\int \tilde{A}_P(z,\omega-\omega_0)exp[-i(\omega-\omega_0)t]d\omega \quad (26)$$

Substituting $A_P(z,t)$ from Eq. (25) into only the dispersive part of Eq. (16), and then applying the Fourier transform to both sides of Eq. (16), results in

$$\frac{\partial\tilde{A}_P(z,\omega-\omega_0)}{\partial z} - i\big[\beta^{(p)}(\omega) - \beta_0 - (\omega-\omega_0)\beta_1\big]\tilde{A}_P(z,\omega-\omega_0) = \tilde{\mathrm{N}}^{(p)}(z,\omega-\omega_0) \quad (27)$$

Where $\tilde{\mathrm{N}}^{(p)} = \mathcal{F}\mathrm{N}^{(p)}$, Next, can use the relation $\left(1 + i\tau_{plmn}\frac{\partial}{\partial t}\right) = \mathcal{F}^{-1}\big(1 + (\omega-\omega_0)\tau_{plmn}\big)\mathcal{F}$ and estimate the shock term as $\tau_{plmn} = \frac{1}{\omega_0}$, perform a change of variable

$$\partial\widetilde{A}'_P(z,\omega-\omega_0) = \tilde{A}_P exp\big[-L^{(p)}(\omega)z\big],\;\; L^{(p)}(\omega) = i\big[\beta^{(p)}(\omega) - \beta_0 - (\omega-\omega_0)\beta_1\big] \quad (28)$$

p and thus derive the ODE that characterizes pulse propagation for mode [59],

$$\begin{aligned}\frac{\partial\widetilde{A}'_P(z,\omega-\omega_0)}{\partial z} &= exp\big[-L^{(p)}(\omega)z\big]i\frac{n_2\omega}{c} \\ &\times \sum_{l,m,n}^{M} \mathcal{F}\Big\{Q^{(1)}_{plmn}2A_l(z,t)[R*(A_lA_n^*)] \\ &+ Q^{(2)}_{plmn}A_l^*(z,t)\big[\big(R.e^{2i\omega_0 t}\big)*(A_mA_n)\big]\Big\} \quad (29)\end{aligned}$$

Using * to denote the superscript and the convolution integral, the coupled system for M modes over a frequency grid of N points can be expressed as a first-order vector ODE (Eq. (25)). By comparing Eq. (29) with Eq. (25), it becomes evident that the right-hand side of Eq. (29) yields the entries of $f(y,z)$, with the vector solution given by:

$$y(z) = \begin{pmatrix}\widetilde{A}'_l \\ \cdot \\ \cdot \\ \widetilde{A}'_M\end{pmatrix}, \qquad \widetilde{A}'_p = \begin{pmatrix}\widetilde{A}'_P(z,\omega_1-\omega_0) \\ \cdot \\ \cdot \\ \widetilde{A}'_P(z,\omega_N-\omega_0)\end{pmatrix} \quad (30)$$

with the initial condition

$$y(0) = \begin{pmatrix} \widetilde{A}'_1(0, \omega_1 - \omega_0) \\ \vdots \\ \widetilde{A}'_M(0, \omega_N - \omega_0) \end{pmatrix}$$

7. conclusion

In conclusion, this chapter has provided a thorough overview of supercontinuum (SC) generation, covering a range of important topics. First, we explored the various applications of SC generation. We then delved into SC generation in both waveguides and bulk media, with a focus on single-mode fibers (SMFs) and fibers of multimode (MMFs). These insights were crucial for understanding the different mechanisms and practical applications of SC generation in various fiber systems. Additionally, we discussed two primary numerical methods used for simulating SC generation: the SSFM and RK4IP method. These approaches are essential tools for modeling and analyzing the SC generation's complex dynamics in both theoretical and practical contexts. Furthermore, we examined the spectral dynamics and broadening mechanisms of SC in different dispersion regimes. In the anomalous GVD regime, we highlighted the key interactions and phenomena that contribute to spectral broadening, while also addressing the dynamics in the normal and all-normal dispersion regimes. By considering these aspects, we have gained a deeper understanding of the conditions that govern SC generation and how to optimize the process for a range of applications.

Finally, we introduced the modeling of multimode SC production, which is characterized by the MM-GNLSE. This framework extends the conventional GNLSE to account for the complex modal interactions and energy exchange between multiple spatial modes in MMFs. Understanding MM-GNLSE is crucial for accurately predicting and optimizing multimode SC generation, particularly in applications where modal dispersion and nonlinear mode coupling play a significant role.

Reference

[1]. Schliesser, A., Picqué, N., & Hänsch, T. W. Mid-infrared frequency combs. Nature photonics, 6(7), 440-449. (2012).

[2]. Heidt, A. M., Feehan, J. S., Price, J. H., & Feurer, T. Limits of coherent supercontinuum generation in normal dispersion fibers. JOSA B, 34(4), 764-775. (2017).

[3]. Kwon, Y., Vazquez-Zuniga, L. A., Park, K., Lee, S., Chang, H., & Jeong, Y.

Combinatorial study of supercontinuum generation dynamics in photonic crystal fibers pumped by ultrafast fiber lasers. IEEE Journal of Quantum Electronics, 52(6), 1-11. (2016).

[4]. Champert, P. A., Couderc, V., Leproux, P., Février, S., Tombelaine, V., Labonté, L., ... & Nérin, P. White-light supercontinuum generation in normally dispersive optical fiber using original multi-wavelength pumping system. Optics express, 12(19), 4366-4371. (2004).

[5]. Shiryaev, V. S., & Churbanov, M. F. Trends and prospects for development of chalcogenide fibers for mid-infrared transmission. Journal of non-crystalline solids, 377, 225-230. (2013).

[6]. Xiao, J., Tian, Y., Zhao, Z., Yao, J., Wang, X., Chen, P., ... & Wang, R. Investigation of tellurium-based chalcogenide double-clad fiber for coherent mid-infrared supercontinuum generation. Optical Fiber Technology, 55, 102144. (2020).

[7]. Saini, T. S., & Sinha, R. K. Mid-infrared supercontinuum generation in soft-glass specialty optical fibers: A review. Progress in Quantum Electronics, 78, 100342. (2021).

[8]. Brewer, R. G. Frequency shifts in self-focused light. Physical Review Letters, 19(1), 8. (1967).

[9]. Alfano, R. R., & Shapiro, S. L. Observation of self-phase modulation and small-scale filaments in crystals and glasses. Physical Review Letters, 24(11), 592. (1970).

[10]. Alfano, R. R., & Shapiro, S. L. Emission in the region 4000 to 7000 Å via four-photon coupling in glass. Physical Review Letters, 24(11), 584. (1970).

[11]. Bloembergen, N. The influence of electron plasma formation on superbroadening in light filaments. Optics Communications, 8(4), 285-288. (1973).

[12]. Brodeur, A., & Chin, S. L. Band-gap dependence of the ultrafast white-light continuum. Physical review letters, 80(20), 4406. (1998).

[13]. Gaeta, A. L. Catastrophic collapse of ultrashort pulses. Physical Review Letters, 84(16), 3582. (2000).

[14]. Kolesik, M., Katona, G., Moloney, J. V., & Wright, E. M. Theory and simulation of supercontinuum generation in transparent bulk media. Applied Physics B, 77, 185-195. (2003).

[15]. Dubietis, A., Tamošauskas, G., Šuminas, R., Jukna, V., & Couairon, A. Ultrafast supercontinuum generation in bulk condensed media (Invited Review). arXiv preprint arXiv:1706.04356. (2017).

[16]. Halder, A., Jukna, V., Koivurova, M., Dubietis, A., & Turunen, J. Coherence of bulk-generated supercontinuum. Photonics Research, 7(11), 1345-1353. (2019).

[17]. Lin, C., & Stolen, R. H. New nanosecond continuum for excited-state spectroscopy. Applied Physics Letters, 28(4), 216-218. (1976).

[18]. Stolen, R. H., & Lin, C. Self-phase-modulation in silica optical fibers. Physical Review A, 17(4), 1448. (1978).

[19]. Beaud, P., Hodel, W., Zysset, B., & Weber, H. Ultrashort pulse propagation, pulse breakup, and fundamental soliton formation in a single-mode optical fiber. IEEE journal of quantum electronics, 23(11), 1938-1946. (1987).

[20]. Golovchenko, E. A., Mamyshev, P. V., Pilipetskii, A. N., & Dianov, E. M. Numerical analysis of the Raman spectrum evolution and soliton pulse generation in single-mode fibers. JOSA B, 8(8), 1626-1632. (1991).

[21]. Ranka, J. K., Windeler, R. S., & Stentz, A. J. Visible continuum generation in air–silica microstructure optical fibers with anomalous dispersion at 800 nm. Optics letters, 25(1), 25-27. (2000).

[22]. Reeves, W. H., Skryabin, D. V., Biancalana, F., Knight, J. C., Russell, P. S. J., Omenetto, F. G., ... & Taylor, A. J. Transformation and control of ultra-short pulses in dispersion-engineered photonic crystal fibres. Nature, 424(6948), 511-515. (2003).

[23]. Dudley, J. M., Genty, G., & Coen, S. Supercontinuum generation in photonic crystal fiber. Reviews of modern physics, 78(4), 1135-1184. (2006).

[24]. Yang, A., Zhang, M., Li, L., Wang, Y., Zhang, B., Yang, Z., & Tang, D. Ga–Sb–S chalcogenide glasses for mid-infrared applications. Journal of the American Ceramic Society, 99(1), 12-15. (2016).

[25]. Shaw, L. B., Thielen, P. A., Kung, F. H., Nguyen, V. Q., Sanghera, J. S., & Aggarwal, I. D. IR supercontinuum generation in As-Se photonic crystal fiber. In Advanced Solid-State Photonics (p. TuC5). Optica Publishing Group. (2005).

[26]. Petersen, C. R. 2-10 μm Mid-infrared Supercontinuum Light Sources. (Doctoral dissertation, Department of Photonics Engineering Technical University of Denmark). (2016).

[27]. Diouf, M., Salem, A. B., Cherif, R., Saghaei, H., & Wague, A. Super-flat coherent supercontinuum source in As 38.8 Se 61.2 chalcogenide photonic crystal fiber with all-normal dispersion engineering at a very low input energy. Applied Optics, 56(2), 163-169. (2017).

[28]. Diouf, M., Cherif, R., Ben Salem, A., & Wague, A. Ultra-broadband, coherent mid-IR supercontinuum expanding from 1.5 to 12.2 μm in new design of AsSe2 photonic crystal fibre. Journal of Modern Optics, 64(13), 1335-1341. (2017).

[29]. Han, J., Chang, S. D., Lyu, Y. J., & Liu, Y. Numerical investigation on coherent mid-infrared supercontinuum generation in chalcogenide PCFs with near-zero flattened all-normal dispersion profiles. Chinese Physics B, 28(10), 104204. (2019).

[30]. Cheshmberah, A., Seifouri, M., & Olyaee, S. Design of all-normal dispersion with Ge 11.5 As 24 Se 64.5/Ge 20 Sb 15 Se 65 chalcogenide PCF pumped at 1300 nm for supercontinuum generation. Optical and quantum electronics, 53, 1-11. (2021).

[31]. Medjouri, A., & Abed, D. Modelling of all-chalcogenide all-normal dispersion photonic crystal fiber for ultraflat mid-infrared supercontinuum generation. Optical and Quantum Electronics, 53, 1-22. (2021).

[32]. Xiao, K., Ye, Y., & Min, R. Broadband coherent mid-infrared supercontinuum generation

in all-chalcogenide microstructured fiber with all-normal dispersion. Frontiers in Physics, 10, 933010. (2022).

[33]. Thi, T. N., Trong, D. H., & Van, L. C. Broadband supercontinuum generation in different lattices of As2Se3-photonic crystal fibers with all-normal dispersion and low peak power. Optical and Quantum Electronics, 56(3), 367. (2024).

[34]. Tomer, D. S., & Kumar, A. A Graded Index Hybrid Photonic Crystal Fiber for Supercontinuum Generation using AsSe2-As2S5. Journal of Optics, 1-10. (2024).

[35]. Perret, S., Fanjoux, G., Bigot, L., Fatome, J., Millot, G., Dudley, J. M., & Sylvestre, T. Supercontinuum generation by intermodal four-wave mixing in a step-index few-mode fibre. Apl Photonics, 4(2). (2019).

[36]. Krupa, K., Tonello, A., Barthélémy, A., Mansuryan, T., Couderc, V., Millot, G., ... & Wabnitz, S. Multimode nonlinear fiber optics, a spatiotemporal avenue. APL Photonics, 4(11). (2019).

[37]. Chen, X., Bickham, S. R., Abbott, J. S., Coleman, J. D., Li, M. J., & Peng, G. D. Multimode fibers for data centers. In Handbook of Optical Fibers (pp. 1-57). Springer. (2018).

[38]. Eftekhar, M. A., Wright, L. G., Mills, M. S., Kolesik, M., Correa, R. A., Wise, F. W., & Christodoulides, D. N. Versatile supercontinuum generation in parabolic multimode optical fibers. Optics express, 25(8), 9078-9087. (2017).

[39]. Poletti, F., & Horak, P. Description of ultrashort pulse propagation in multimode optical fibers. JOSA B, 25(10), 1645-1654. (2008).

[40]. Ramsay, J., Dupont, S., Johansen, M., Rishøj, L., Rottwitt, K., Moselund, P. M., & Keiding, S. R. Generation of infrared supercontinuum radiation: spatial mode dispersion and higher-order mode propagation in ZBLAN step-index fibers. Optics Express, 21(9), 10764-10771. (2013).

[41]. Kubat, I., & Bang, O. Multimode supercontinuum generation in chalcogenide glass fibres. Optics express, 24(3), 2513-2526. (2016).

[42]. Khalifa, A. B., Salem, A. B., & Cherif, R. Mid-infrared supercontinuum generation in multimode As 2 Se 3 chalcogenide photonic crystal fiber. Applied optics, 56(15), 4319-4324. (2017).

[43]. Kibler, B. Propagation non-linéaire d'impulsions ultracourtes dans les fibres optiques de nouvelle génération (Doctoral dissertation, Université de Franche-Comté). (2007).

[44]. Hult, J. A fourth-order Runge–Kutta in the interaction picture method for simulating supercontinuum generation in optical fibers. Journal of Lightwave Technology, 25(12), 3770-3775. (2007).

[45]. Ghanbari, A., & Olyaee, S. Numerical Study on Normalized Split-step Fourier Method and Fourth-order Runge-Kutta Method in Laser Pulses Generation by Use of Photonic Crystal Fibers. Majlesi Journal of Electrical Engineering, 17(3), 49-55. (2023).

[46]. Medjouri, A., & Abed, D. Theoretical study of coherent supercontinuum generation in

chalcohalide glass photonic crystal fiber. Optik, 219, 165178. (2020).

[47]. Martinez-Angulo, J. R., Hernandez-Garcia, J. C., Barron-Zambrano, J. H., Estudillo-Ayala, J. M., Pottiez, O., Lauterio-Cruz, J. P., ... & Rojas-Laguna, R. Numerical study on nonlinear and chaotic effects in standard fibre using RK4IP method. Results in Physics, 15, 102613. (2019).

[48]. Genty, G., Coen, S., & Dudley, J. M. Fiber supercontinuum sources. JOSA B, 24(8), 1771-1785. (2007).

[49]. Fang, Y., Bao, C., Li, S. A., Wang, Z., Geng, W., Wang, Y., ... & Yue, Y. Recent progress of supercontinuum generation in nanophotonic waveguides. Laser & Photonics Reviews, 17(1), 2200205. (2023).

[50]. Sylvestre, T., Genier, E., Ghosh, A. N., Bowen, P., Genty, G., Troles, J., ... & Dudley, J. M. Recent advances in supercontinuum generation in specialty optical fibers. JOSA B, 38(12), F90-F103. (2021).

[51]. Agrawal, G. P. Nonlinear fiber optics. In Nonlinear Science at the Dawn of the 21st Century (pp. 195-211). Berlin, Heidelberg: Springer Berlin Heidelberg. (2000).

[52]. Genier, E., Bowen, P., Sylvestre, T., Dudley, J. M., Moselund, P., & Bang, O. Amplitude noise and coherence degradation of femtosecond supercontinuum generation in all-normal-dispersion fibers. JOSA B, 36(2), A161-A167. (2019).

[53]. Medjouri, A., & Abed, D. Design and modelling of all-normal dispersion As39Se61 chalcogenide photonic crystal fiber for flat-top coherent mid-infrared supercontinuum generation. Optical Fiber Technology, 50, 154-164. (2019).

[54]. Poletti, F., & Horak, P. Dynamics of femtosecond supercontinuum generation in multimode fibers. Optics Express, 17(8), 6134-6147. (2009).

[55]. Salem, A. B., Trichili, A., Cherif, R., & Zghal, M. Rigorous study of supercontinuum generation in few mode fibers. Applied Optics, 55(16), 4317-4322. (2016).

[56]. Wright, L. G., Ziegler, Z. M., Lushnikov, P. M., Zhu, Z., Eftekhar, M. A., Christodoulides, D. N., & Wise, F. W. Multimode nonlinear fiber optics: massively parallel numerical solver, tutorial, and outlook. IEEE Journal of Selected Topics in Quantum Electronics, 24(3), 1-16. (2017).

[57]. Wright, L. G., Wabnitz, S., Christodoulides, D. N., & Wise, F. W. Ultrabroadband dispersive radiation by spatiotemporal oscillation of multimode waves. Physical review letters, 115(22), 223902. (2015).

[58]. Mumtaz, S., Essiambre, R. J., & Agrawal, G. P. Nonlinear propagation in multimode and multicore fibers: generalization of the Manakov equations. Journal of Lightwave Technology, 31(3), 398-406.2. (2012).

[59]. Khakimov, R., Shavrin, I., Novotny, S., Kaivola, M., & Ludvigsen, H. Numerical solver for supercontinuum generation in multimode optical fibers. Optics express, 21(12), 14388-14398. (2013).

Chapter 4:

Modeling of Supercontinuum Generation in Chalcogenide PCF

1. Introduction

This work presents a comprehensive model of supercontinuum generation in single-mode PCF. We choose the $Ge_{20}As_{20}Se17Te_{43}$ (GAST) as a solid background glass, and this owing to its excellent properties such as long-wave IR transparency and easiness to obtain an ANDi regime due to larger material zero-dispersion-wavelength (ZDW) [1,2]. Besides, we propose a PCF design of with a Circular Lattice (CL-PCF). This CL-PCF is described by six rings to ensure well confinement of the light in the fiber core. The numerous linear and nonlinear properties are accurately computed for various wavelengths by using the finite difference frequency domain (FDFD) method combined with the perfectly matched layers (PML) boundary condition. Besides, optical pulses propagation and SC generation process are both modeled by solving the GNLSE numerically.

2.Theoratical background

2.1 Structure of GAST based CL-PCF

Here, we suggest a CL-PCF structure design with six air hole rings. The design's transverse cross-section is illustrated in Fig. 1.

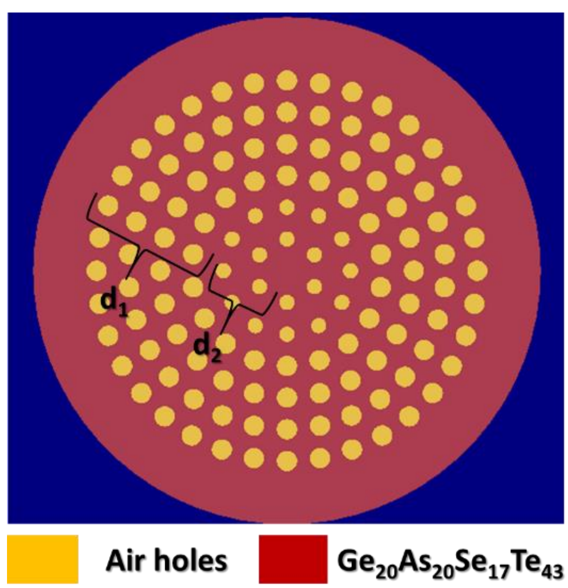

Fig. 1. Cross-sectional transverse of $Ge_{20}As_{20}Se_{17}Te_{43}$ glass CL-PCF.

. In this structure, we choose the $Ge_{20}As_{20}Se_{17}Te_{43}$ Chalcogenide glass as a solid background material. The distance between two adjacent air holes, also known as pitch is 3 µm, the first two rings have diameters of air holes d_1 equal to 1.4 µm and from the third ring to the sixth ring, the diameters of the air holes d_2 are variable from 1 µm to 1.5 µm with a step of 0.1 µm. The number of rings and diameters of air holes are carefully selected to achieve well waveguiding within the core with a slight confinement loss and changing d_2 to engineer the dispersion in regime ANDi. Besides, the proposed GAST based CL-PCF can be fabricated by a conventional method and drawing at 310°C [2, 3].

2.2 Linear and nonlinear parameters computation

We use a complete vector finite-difference frequency-domain method (FDFD) combined by perfectly matched layers (PML) as a boundary condition to simulate CL-PCF properties. In this case, the Maxwell's equations can be expressed as [4, 5]:

$$\begin{aligned} ik_0 s\varepsilon_r E &= \nabla \times H \\ -ik_0 s\varepsilon_r H &= \nabla \times E \end{aligned} \qquad (1)$$

$$s = \begin{pmatrix} \frac{S_x}{S_y} & & \\ & \frac{S_x}{S_y} & \\ & & S_x S_y \end{pmatrix} \qquad (2)$$

Where: $S_x = 1 - (\sigma_x / i\omega\varepsilon_0)$ and $S_y = 1 - (\sigma_y / i\omega\varepsilon_0)$

E and H are the electric field and magnetic field, respectively, k_0 is the wavenumber in the vacuum, ε_0 is the vacuum permittivity, ω is the angular frequency and σ is the conductivity [6]. An appropriate meshing system for the structure of PCF converts the equation system presented in (1) into a matrix eigenvalue problem. The numerical solution is achieved using the sparse matrix method to determine the optical field distribution and the effective refractive index n_{eff} [40]. Using the Sellmeier equation, the refractive indices can be determined [2]:

$$n = 1 + \sum_j \frac{A_j \lambda^2}{\lambda^2 - \lambda_j^2} \qquad (3)$$

where λ is the wavelength. A_j and λ_j are the Sellmeier coefficient. **Table 1** shows the values A_j and λ_j of (GAST) glasses.

Table. 1 Sellmeier coefficients of GAST glass.

A_j $(j = 1,2,3)$	λ_j^2 (j=1, 2, 3)
8.7503	0.39859
$3.425.10^{-4}$	191.88
-25.56	−17840

The chromatic dispersion is essential in determining the SC spectrum [7]. It results from the contribution of two sources: the waveguide dispersion and the material dispersion, denoted by D and given by [8]:

$$D(\lambda) = -\frac{\lambda}{c}\frac{d^2 n_{eff}}{d\lambda^2} \qquad (4)$$

where λ, c, n_{eff} are the wavelength, the speed of light in the vacuum, and the effective refractive index, respectively. The confinement loss (L_c) of the fundamental mode in the fiber can be defined by [9]:

$$L_c = \frac{20}{\ln(10)}\frac{2\pi}{\lambda} Im(n_{eff}) \qquad (5)$$

where $Im(n_{eff})$ represents the imaginary part of the effective index of the modes.

The nonlinear coefficient γ plays a significant role in SC. Its coefficient can be calculated by the following formula [10]:

$$\gamma = \frac{n_2 \omega_0}{c A_{eff}} \qquad (6)$$

Where n_2 is the nonlinear refractive index of $Ge_{20}As_{20}Se_{17}Te_{43}$ glass is calculated as [2]:

$$n_2 = 4.27 \times 10^{-16} \frac{(n_0^2-1)^4}{n_0^2} [cm^2.w^{-1}] \qquad (7)$$

where n_0 is the linear refractive. Moreover, A_{eff} is the effective area of the fundamental mode, defined as [11].

$$A_{eff} = \frac{(\iint |F(x,y) dxdy|)^2}{\iint |F(x,y)|^4 dxdy} [\mu. m^2] \qquad (8)$$

With $F(x, y)$ is the distribution of fundamental mode in fiber.

2.3 Modelling of pulses propagation and SC generation

This work aims to realize an SC in the mid-infrared domain. We employ the generalized nonlinear Schrödinger equation (GNLSE). This equation shows the contributions of both the linear and nonlinear effects given by [12, 13]:

$$\frac{\partial A}{\partial Z} + \frac{\alpha}{2} A - \sum_{n\geq 2} \frac{i^{n+1}}{n!} \beta_n \frac{\partial^n A}{\partial T^n} = i\gamma(1 - f_R)$$
$$\left([A]^2 A - \frac{i}{\omega_0} \frac{\partial}{\partial T} [A]^2\right) + i\gamma f_R \left(1 + \frac{i}{\omega_0}\right)$$
$$(A \int_0^\infty h_R(\tau) |A(z, T - \tau)|^2 \partial\tau) \qquad (9)$$

The first side represents the linear propagation effects, where A is the pulse envelope function, α is the loss coefficient, β_n is the nth-order dispersion, and ω_0 is the input pulse frequency. The second side of the equation represents the nonlinear effects, γ is the nonlinear coefficient. Finlay, $h_R(t)$ is the delayed Raman contribution shown as [14]:

$$h_R(t) = \frac{\tau_1^2 + \tau_2^2}{\tau_1 \tau_2} \exp\left(-\frac{t}{\tau_2}\right) \sin\left(\frac{t}{\tau_1}\right) \qquad (10)$$

where τ_1 = 15.2 fs and τ_2 = 230.5 fs, and $f_R = 0.031$ is the fractional contribution of the Raman response [38], resulting from the normalization of $\int_0^\infty h_R(t) dt = 1$ [15]

Many methods have been reported to solve the GNLSE. The technique used in our simulations is called the Runge-Kutta in the interaction picture (RK4IP) method. This method is chosen for its high numerical accuracy and local error of fifth-order O (h5) with a global error of only O(h4). The RK4IP and Split Step Fourier Method (SSFM) are closely linked [12].

Coherence is an essential parameter for determining the quality of the SC, the first-order degree of coherence given by [16]:

$$|g_{12}^1(\lambda, t_1 - t_2)| = \left| \frac{\langle E_1^*(\lambda, t_1) E_2(\lambda, t_2) \rangle}{\langle |E_1(\lambda, t_1)|^2 \rangle \langle |E_2(\lambda, t_2)|^2 \rangle} \right| \qquad (11)$$

Where E_1, E_2 are the electric fields, and t is the time measured at the scale of the temporal resolution of the spectrometer used to resolve these spectra. We use $t_1 - t_2 = 0$ to obtain the coherence $|g_{12}^1(\lambda)|$ depending on the wavelength. When $|g_{12}^1(\lambda)| = 1$, the coherence of SC is perfect [17].

3. Simulation results and discussion

3.1 Dispersion engineering of GAST PCF

Fig. 2 depicts the refractive index variation of GAST as a function of wavelengths for a spectral range spanning from 2 μm to 12 μm, using the Sellmeier model. The refractive index curve of GAST shows a decreasing pattern as the wavelength increases from 2 μm to 12 μm, with values ranging from 3.23 to 2.9. This corresponds with measurements taken by an IR ellipsometer (IR-VASE MARK II, J. A. Woollam Co.) [2].

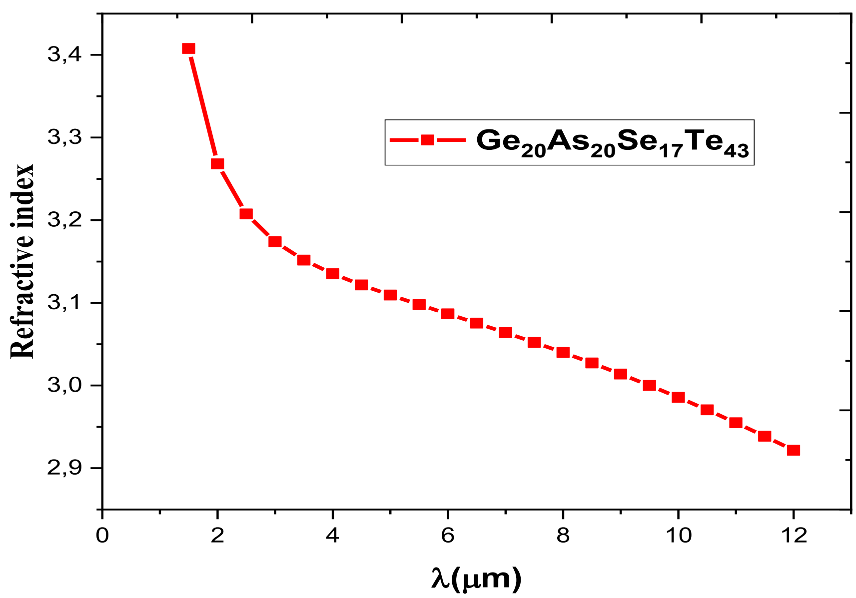

Fig. 2 Refractive index of the $Ge_{20}As_{20}Se_{17}Te_{43}$ (GAST) versus wavelength.

To achieve the ANDi property of the proposed CL-PCF, we adjusted the dispersion by varying the diameter of the first two rings of air holes d_2 while keeping Λ=3 μm and d_1=1.4 μm. Fig. 3 shows the dispersion variation as a function of wavelengths between 2 μm and 12.5 μm, with d_2

varying from 1 µm to 1.5 µm in increments of 0.1 µm, demonstrating the effect of changing d_2 on the dispersion of the proposed CL-PCF. As can be observed, when d_2 increases, the dispersion curve is up shifted, and the ANDi regime is readily achieved for d = 1.3 µm with a peak close to zero obtained around the wavelength 5.8 µm.

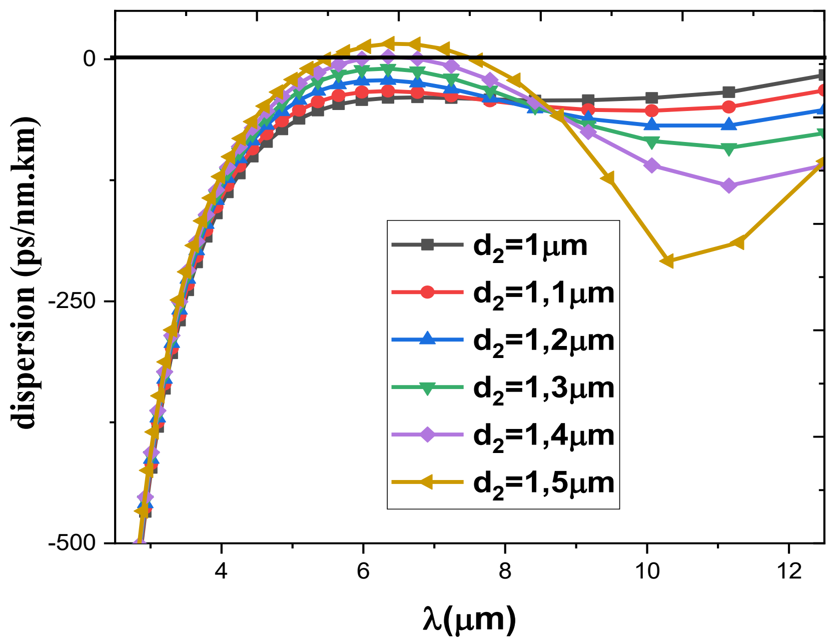

Fig. 3. dispersion dependent wavelength with Λ = 3µm, d_1=1.4 µm and d_2 varies.

Furthermore, Fig. 4 depicts the variation of the confinement loss (L_C) with wavelengths. As shown in this fig, the confinement loss curve shows that the optical (GAST) PCF material is suitable for pumping at a wavelength of 5.8 µm. The curve demonstrates that the loss remains very low from 2 to 9 µm, indicating strong energy confinement within this wavelength range and making the material effective for energy transmission, especially at 5.8 µm. Beyond 9 µm, optical losses begin to increase, indicating a decrease in efficiency outside this range.

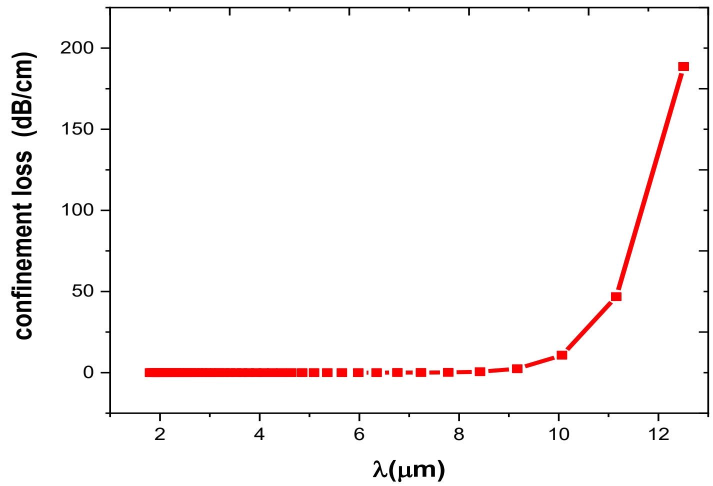

Fig. 4. The confinement loss dependent wavelength with Λ = 3μm, d_1=1.4 μm and d_2=1.3 μm

Finally, the effective area of fundamental mode A_{eff} and the nonlinear coefficient γ are both computed and presented in Fig. 5. The GAST PCF shows a decrease in the Kerr coefficient with increasing wavelength, while the effective area increases, indicating wider field spread. The Kerr coefficient is about 1,495 $m^{-1}.W^{-1}$ at the selected pump wavelength of 5.8 μm, demonstrating high nonlinearity at this wavelength.

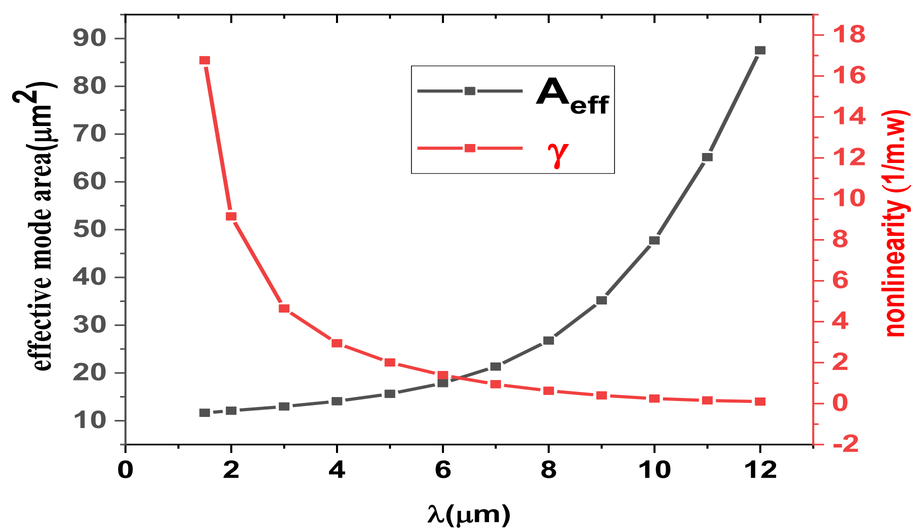

Fig.5 The Effective area and nonlinear coefficient variation with the wavelength.

3.2 SC generation in a GAST PCF

To study SC generation in our optimized PCF design, we numerically solve the Generalized Nonlinear Schrödinger Equation (GNLSE) given by Eq. (7). Optical pulses within the GAST PCF core are modelled by a hyperbolic secant envelope $A(z,t) = \sqrt{P_0}\text{sech}\,(t/T_0)$, where P_0, T_{FWHM} = 1.763 T_0, are the peak power, and the pulse duration, respectively. Laser pulses are pumped at 5.8 µm, close to the zero-dispersion wavelength. The Taylor series expansion coefficients of the propagation constant have been calculated up to the 9th order at a wavelength of 5.8 µm for two dispersion regimes: the ANDi regime with d_2=1.3 µm in Table 2, and anomalous dispersion with d_2=1.5 µm in Table 3. Furthermore, the propagation loss is neglected in the GNLSE because the pulse propagates over only a short length of the PCF. Firstly, our objective is to compare SC outputs in two dispersion regimes. Fig. 6 presents a comparison of SC outputs in two dispersion regimes: the anomalous dispersion regime with d_2=1.5 µm (a) and the ANDi regime with d_2=1.3 µm (b). In the anomalous dispersion regime, the SC output is wide and has more spectral instabilities. On the other hand, the ANDi regime produces a smoother spectral output with fewer instabilities, even though its spectral width is narrower than that of the anomalous regime. This proves that the ANDi regime is essential for optimal SC generation. The values of the parameters used in this simulation are P_0=1Kw, T_{FWHM}=150 fs and the length of the GAST PCF is 15 mm.

Table 2 The propagation constant for d_2=1.5 µm.

Coefficient	Value
β_2	-187.085 ps^2/km
β_3	12.0773 ps^3/km
β_4	0.133769 ps^4/km
β_5	-8.62397 ×10^{-03} ps^5/km
β_6	2.21362 ×10^{-04} ps^6/km
β_7	-3.2625 ×10^{-6} ps^7/km
β_8	2.73342 ×10^{-8} ps^8/km
β_9	-1.02401 ×10^{-10} ps^9/km

Table 3 The propagation constant for d_2=1.3 μm.

Coefficient	Value
β_2	253.841 ps^2/km
β_3	3.78122 ps^3/km
β_4	6.10128 $\times 10^{-02}$ ps^4/km
β_5	-1.0278 $\times 10^{-03}$ ps^5/km
β_6	1.10671 $\times 10^{-05}$ ps^6/km
β_7	-7.85847 $\times 10^{-8}$ ps^7/km
β_8	3.44315 $\times 10^{-10}$ ps^8/km
β_9	-7.08451 $\times 10^{-13}$ ps^9/km

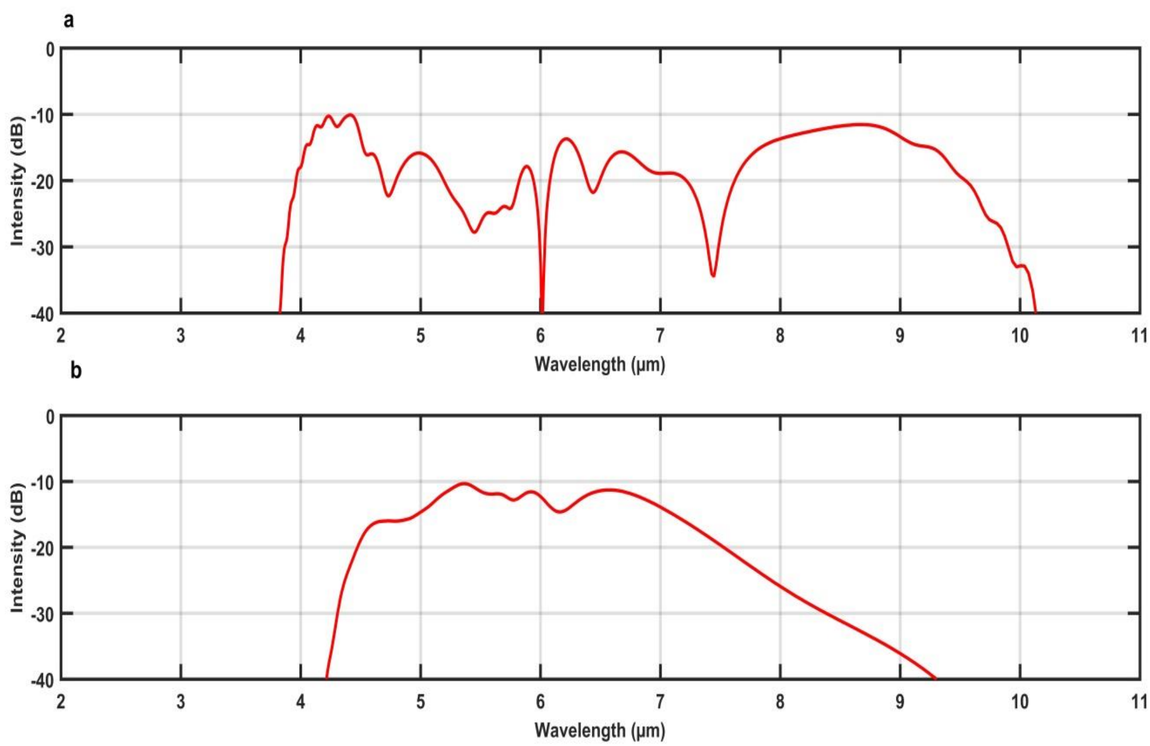

Fig. 6. SC generation outputs in anomalous dispersion regime with d_2=1.5 μm (a) and ANDi regime with d_2=1.3 μm (b)

In order to explain the dynamics of SC broadening in the ANDi regime, the characteristic dispersive and nonlinear length scales are calculated by [18]: $L_D = T_0^2|\beta_2|^{-1} = 28.6\,mm$, $L_{NL} = (\gamma P_0)^{-1} = 0.67\,mm$, respectively. It can be observed that the nonlinear length is smaller than the dispersive length, which makes the nonlinear effects responsible for spectral broadening over the first few millimeters of the PCF. **Fig. 7** shows the pulse evolution in both spectral and temporal domains with P_0=1Kw and T_{FWHM}=150 fs over the 15 mm length of the GAST PCF, as can be noted. Initially, the self-phase modulation (SPM) is the main factor causing symmetric spectral broadening of the pulse. Accordingly, the wave-breaking (OWB) distance is calculated as 5.3 mm using the formula [18]:

$$L_{OWB} = \sqrt{\frac{3\beta_2}{2\beta_2+2\gamma P_0 T_0^2}\frac{T_0^2}{\beta_2}} \quad \textbf{(12)}$$

The OWB effects become noticeable after 5.3 mm, where side lobes appear on both sides of the spectrum, marking the onset of the OWB process. This analysis emphasizes the initial impact of SPM on spectral broadening, followed by wave-breaking effects as propagation distance increases.

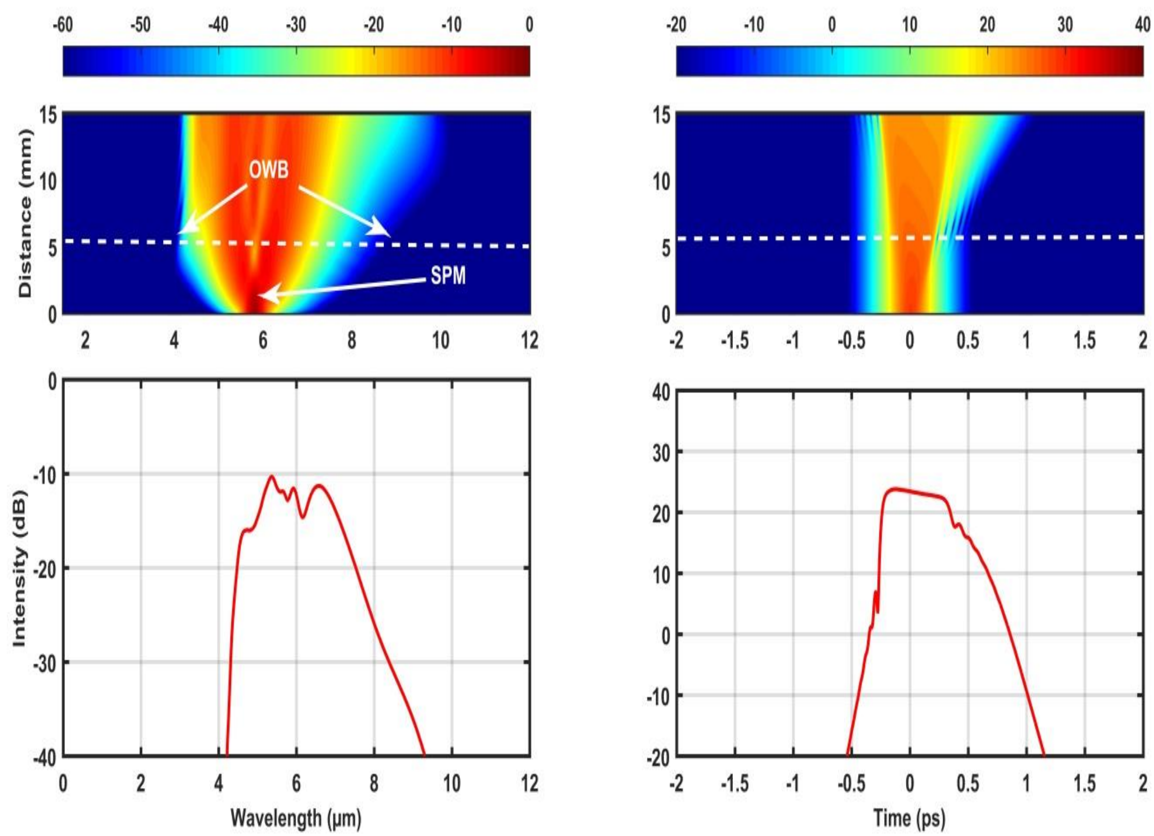

Fig. 7. Spectral and temporal evolution in 15 mm PCF length with pump wavelength 5.8 μm. P_0=1Kw, T_{FWHM}=150 fs. The beginning of the OWB process is at the dashed line.

3.2.1 Influence of the initial conditions of the pump pulses on the SC spectrum

In this section, we have studied the effects of the initial conditions of the pump pulses on the SC spectrum. Firstly, to show how the pulse duration affects the characteristics of the SC spectrum, particularly its bandwidth and flatness, we vary the pulse duration values to 200 fs (a), 150 fs (b), 100 fs (c), and 50 fs (d) with a peak power of 2 kW and pump wavelength 5.8 µm. As shown in Fig. 8, it is clear that the bandwidth of the SC generation decreases for input pulse durations of 100 fs, 150 fs, and 200 fs. But, for a pulse duration of 50 fs, a broadband and flat SC spectrum is observed, which extends from 4.18 to 9.2 µm at -10 dB in a 15 mm length of the PCF. Consequently, this short pulse duration is adopted for the remainder of the study to achieve broader and flatter spectra.

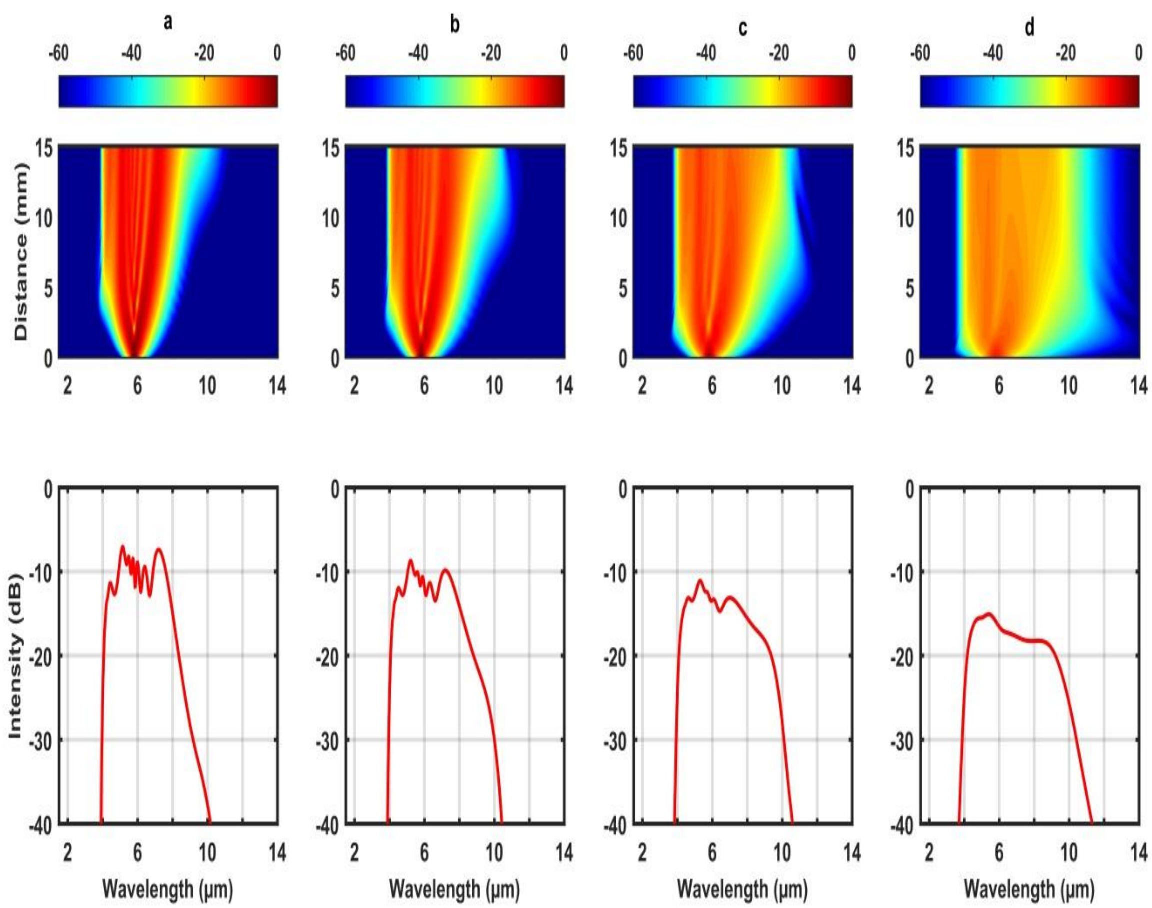

Fig. 8. Generated SC spectrum in 15 mm PCF length with an input pulse peak power of 2kw and various pulse duration T_{FWHM} values of 200fs (a), 150fs (b), 100fs (c), and 50fs (d).

Secondly, **Fig. 9** shows the influence of increasing pulse power on the generated SC bandwidth, with the pulse duration fixed at 50 fs. The peak power is adjusted to be 1 kW, 5 kW, 10 kW, and 15 kW, respectively. It can be observed that the SC spectrum achieves maximum bandwidth and high flatness at a peak power of 15 kW, covering a range from 2.9 to 13.95 µm at -5 dB with a pump wavelength of 5.8 µm in a 15 mm length of the PCF, as shown in **Fig. 9(d)**.

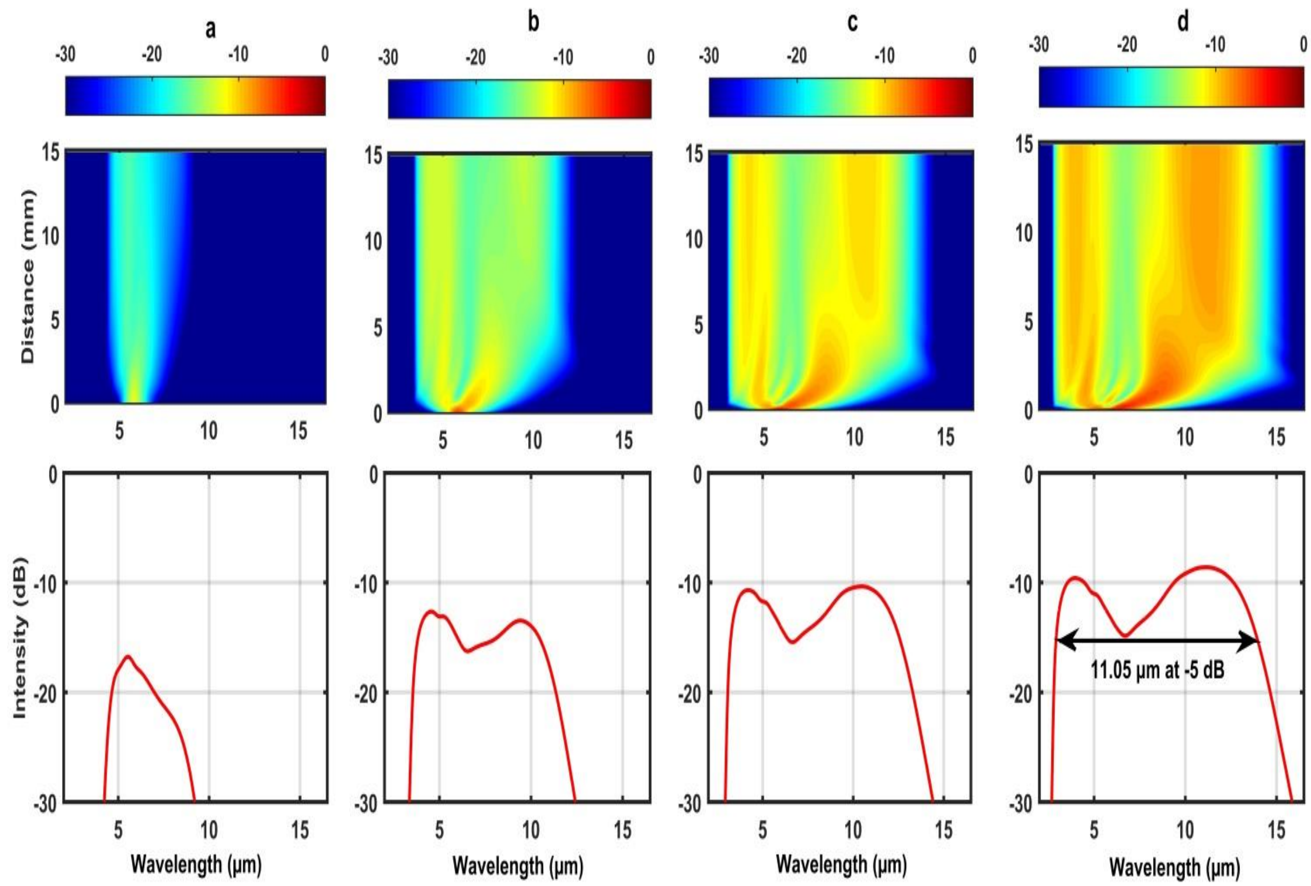

Fig. 9. Generated SC spectrum in 15 mm PCF length with an input pulse T_{FWHM} of 50fs and various values of pulse peak power: 1kw (a), 5kw (b), 10kw (c), and 15kw (d).

3.2.2 Coherence of the generated SC spectrum

Finally, Fig. 10 shows the coherence of SC spectrum versus wavelengths for a spectral range from 2 µm and 14 µm with an input peak power of 15 kw and a pulse duration of 50 fs. The SC spectrum exhibits perfect coherence in this range of wavelengths. This high spectral coherence is achieved by eliminating effects of soliton through pumping in the regime of normal dispersion. As a result, self-phase modulation (SPM), a deterministic process that preserves the coherence of the input pulses, is primarily employed to achieve spectral broadening [19]. Table (4) depicts an overview of the parameters used in the simulation used to generate the SC shown in Fig. 9(d).

Table 4. Optical parameters of the proposed GAST PCF based SC source.

Fiber length	15mm
Pump wavelength	5.8 µm
Peak power	15 kW
Pulse duration	50 fs
SC bandwidth	2.9-13.95
Flatness	-5 dB

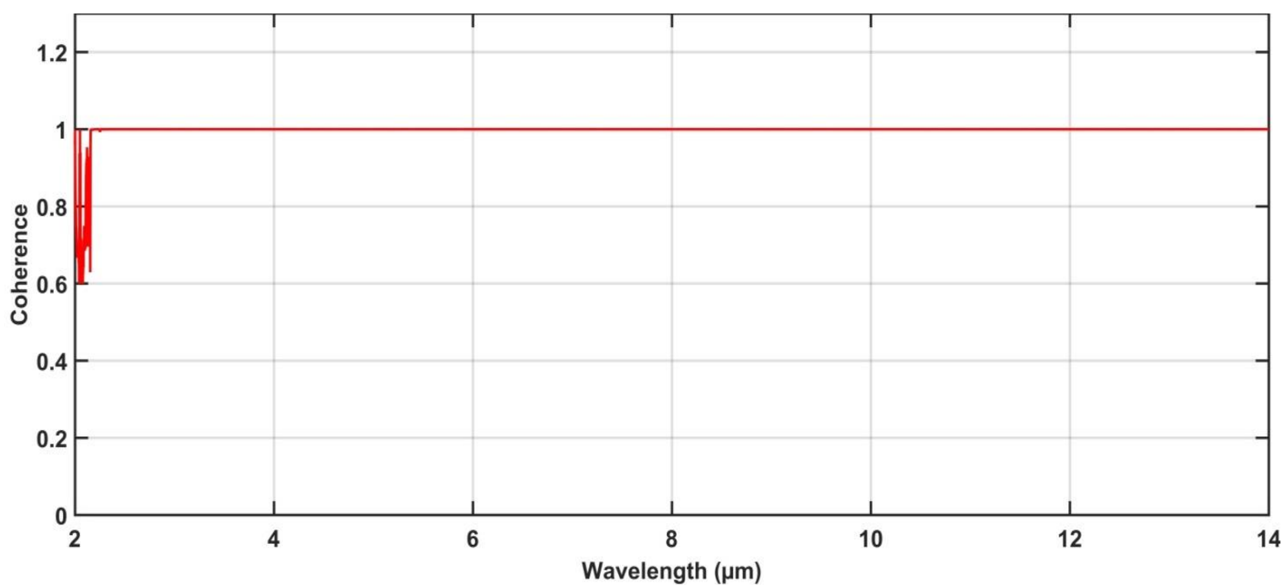

Fig. 10. Coherence of the SC spectra with pump wavelength 5.8 µm, T_{FWHM}=50 fs, and P_0 =15KW in 15 mm length of PCF.

The proposed SC based on GAST PCF offers several advantages over previous works. The SC spectrum covers a wide wavelength range of 2.9 µm to 13.95 µm at -5 dB and demonstrates high coherence. Table 5 provides a summary of the experimental and theoretical results related to our work, highlighting the capability of our designed photonic crystal fiber (PCF) to generate a flat and broad supercontinuum (SC). Through Table 2, our work demonstrates superiority over many earlier studies in terms of spectral coverage. The table provides a summary of the experimental and theoretical results, highlighting the capability of our designed PCF to generate a flat and broad supercontinuum (SC). These excellent optical properties make the proposed SC spectrum highly applicable to diverse applications in scientific and industry.

Table 5: Summary of Theoretical and Experimental Results of SC Generation Based on Mid-IR ANDi

References	Nonlinear optical medium	Pump wavelength (μm)	SC Spectrum (μm)	Spectral flatness (dB)
[20]	As_2S_5 HPCF	2.5	0.9-5.25	-20
	As_2S_5 HPCF	2.5	1.05-5.05	-8
[21]	double-clad $AsSe_2$- PCF	6.7	4.14	-8
[22]	$Ga_8Sb_{32}S_{60}$- PCF	4.5	1.65 - 9.24	-20
[23]	$As_{38.8}Se_{61.2}$- PCF	3.7	2.9-4.575	-3
[24]	GeS_2-Ga_2S_3-CsI -- PCF	3	1.45-5.95	-20
[25]	$Ge_{15}Sb_{15}Se_{70}$ / $Ge_{20}Se_{80}$- all-solid	3	1.6-7	-5
[26]	As_2S_3- PCF	2.8	2.410 – 3.150	-20
[27]	As_2Se_3 -PCF	4.7	2 - 10	-40
[28]	$Ge_{11.5}As_{24}S_{64.5}$-PCF	7	3.823 -13.577	-30
In this work	$Ge_{20}As_{20}Se_{17}Te_{43}$ -PCF	5.8	2.9 - 13.95 μm	-5

Because of its exceptional coherence, high brightness, and spectral uniformity, mid-IR broadband supercontinuum sources have attracted considerable attention, particularly for applications in optical coherence tomography (OCT) [29,30,31].

Ultrahigh-resolution optical coherence tomography (OCT) has been established as a noninvasive imaging technique designed for micrometer-scale cross-sectional visualization of biological tissues and materials, requiring a high penetration depth of up to several microns [20].

The coherence length (l_c) is a crucial parameter for determining the longitudinal resolution in the depth direction of optical coherence tomography (OCT). It can be computed with the following formula [20,29]:

$$l_c = \frac{2ln2}{\pi}\frac{\lambda_0}{\Delta\lambda} \qquad (13)$$

Where the pump wavelength is denoted by λ_0, and $\Delta\lambda$ denotes the bandwidth of the produced supercontinuum (SC). Consequently, ultrawide bandwidth light sources with shorter central wavelengths are highly desirable for enhancing depth resolution [20].

In our simulations, we observed that injecting 15 kw pulses at a central wavelength of 5.8 μm into a 15 mm long photonic crystal fiber produces a broad supercontinuum (SC) with a spectral width of 11.05 μm. Consequently, the coherence length is calculated to be 1.3 μm, which confirms the feasibility of an OCT imaging system with high resolution in the mid-infrared fingerprint region. Moreover, the ultra-flat nature of the generated supercontinuum suppresses side-lobe formation in the interferogram, thereby ensuring the excellent axial resolution required for precise imaging. [22,32].

Finally, we have investigated the impact of the material loss on the bandwidth of the generated SC spectra. Fig. 11 shows the output SC spectrum for an input laser pulse with a peak power and FWHM of 15 kW and 50 fs, respectively, where the optical attenuation due to the material loss is considered. The transmission spectrum is experimentally measured for a 15 mm thick of the GAST glass sample and the loss coefficient is estimated to be 0.17 dB/mm [58]. Compared to the previous case where the loss is not incorporated in simulations, the generated SC spectrum bandwidth at the spectral flatness level of less than 10 dB is reduced only by less than 1 μm. Moreover, this spectral narrowing can be easily compensated by increasing the peak power of the input optical pulses.

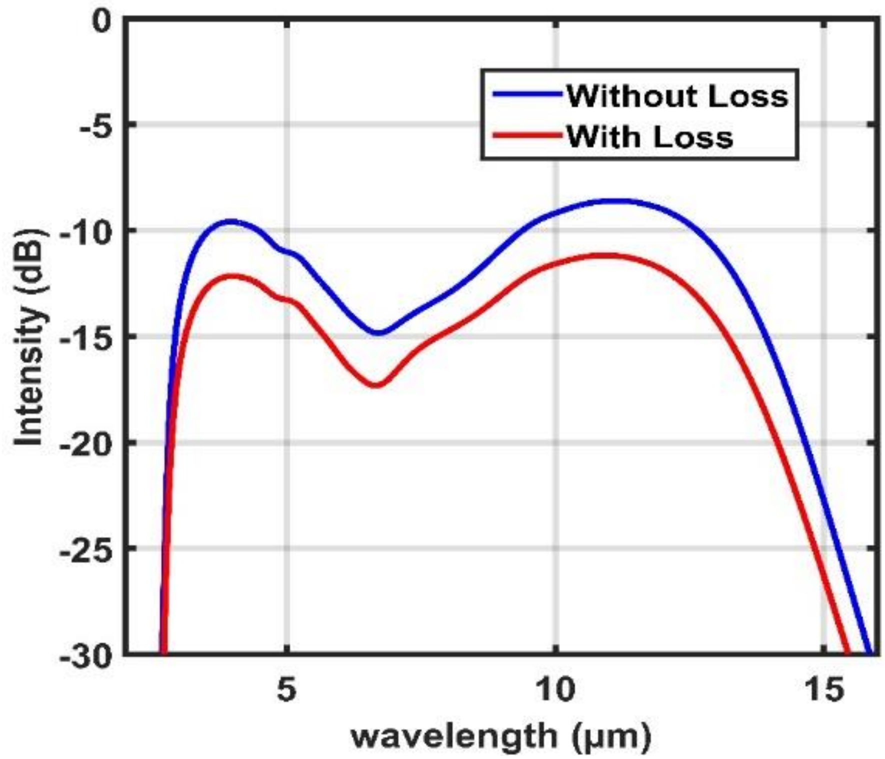

Fig. 11. SC generated with an input optical laser pulse peak power and T_{FWHM} of 15 kW and 50 fs, respectively with and without taking into account propagation material loss.

4. Conclusion

In summary, we have presented and discussed the numerical investigation of broadband supercontinuum generation in $Ge_{20}As_{20}Se_{17}Te_{43}$ chalcogenide Circular Lattice Photonic Crystal Fiber (CL-PCF) with all-normal dispersion regime (ANDi). This CL-PCF is described by six rings of air holes. Based on the CL-PCF's high nonlinear refractive index and attractive dispersion properties, the results show that this material has tremendous potential for producing a large and highly coherent supercontinuum in the mid-infrared range. With a pump wavelength of 5.8 µm, a 15-kW peak power and 50 fs pulse duration, the results highlight the material and CL-PCF design potential for producing a broad and stable supercontinuum that extends from 2.9 to 13.95 µm only at -5 dB spectral level. This is particularly significant in the mid-infrared region, owing to the favorable properties of $Ge_{20}As_{20}Se_{17}Te_{43}$ chalcogenide glass, such as the high Kerr nonlinearity (γ

= 1,495 $m^{-1}\cdot W^{-1}$) at a wavelength of 5.8 μm, in addition to its broad transparency range. Future studies can focus on further refining fiber designs to maximize efficiency and coherence, as well as validating the numerical predictions through experimental work. Overall, the insights from this investigation provide a valuable contribution to the development of new nonlinear optical devices based on chalcogenide photonic crystal fibers, paving the way for future advancements in mid-infrared supercontinuum sources.

Reference

[1]. Zhao, Z., Wang, X., Dai, S., Pan, Z., Liu, S., Sun, L., ... & Wang, R. 1.5–14 μm midinfrared supercontinuum generation in a low-loss Te-based chalcogenide step-index fiber. Optics letters, 41(22), 5222-5225. (2016).

[2]. Xiao, J., Tian, Y., Zhao, Z., Yao, J., Wang, X., Chen, P., ... & Wang, R. Investigation of tellurium-based chalcogenide double-clad fiber for coherent mid-infrared supercontinuum generation. Optical Fiber Technology, 55, 102144. (2020).

[3]. Jiao, K., Yao, J., Zhao, Z., Wang, X., Si, N., Wang, X., ... & Wang, R. Mid-infrared flattened supercontinuum generation in all-normal dispersion tellurium chalcogenide fiber. Optics Express, 27(3), 2036-2043. (2019).

[4]. Medjouri, A., Simohamed, L. M., Ziane, O., Boudrioua, A., & Becer, Z. Design of a circular photonic crystal fiber with flattened chromatic dispersion using a defected core and selectively reduced air holes: Application to supercontinuum generation at 1.55 μm. Photonics and Nanostructures-Fundamentals and Applications, 16, 43-50. (2015).

[5]. Guo, S., Wu, F., Albin, S., Tai, H., & Rogowski, R. S. Loss and dispersion analysis of microstructured fibers by finite-difference method. Optics Express, 12(15), 3341-3352. (2004).

[6]. Su, W., Lou, S., Zou, H., & Han, B. Design of a highly nonlinear twin bow-tie polymer photonic quasi-crystal fiber with high birefringence. Infrared Physics & Technology, 63, 62-68. (2014).

[7]. Karim, M. R., Rahman, B. M. A., & Agrawal, G. P. Dispersion engineered Ge 11.5 As 24 Se 64.5 nanowire for supercontinuum generation: A parametric study. Optics Express, 22(25), 31029-31040. (2014).

[8]. Van, L. C., Thi, T. N., Le Tran, B. T., Trong, D. H., Minh, N. V. T., & Van Le, H. Multi-octave supercontinuum generation in As2Se3 chalcogenide photonic crystal fiber. Photonics and Nanostructures-Fundamentals and Applications, 48, 100986. (2022).

[9]. Wang, C. C., Li, W. M., Li, N., & Wang, W. Q. Numerical simulation of coherent visible-to-near-infrared supercontinuum generation in the CHCl3-filled photonic crystal fiber with 1.06 μm pump pulses. Optics & Laser Technology, 88, 215-221. (2017).

[10]. Ahmad, H., Karim, M. R., & Rahman, B. M. A. Modeling of dispersion engineered

chalcogenide rib waveguide for ultraflat mid-infrared supercontinuum generation in all-normal dispersion regime. Applied Physics B, 124, 1-10. (2018).

[11]. Siwicki, B., Klimczak, M., Stępień, R., & Buczyński, R. Supercontinuum generation enhancement in all-solid all-normal dispersion soft glass photonic crystal fiber pumped at 1550 nm. Optical Fiber Technology, 25, 64-71. (2015).

[12]. Hult, J. A fourth-order Runge–Kutta in the interaction picture method for simulating supercontinuum generation in optical fibers. Journal of Lightwave Technology, 25(12), 3770-3775. (2007).

[13]. Agrawal, Govind P. "Nonlinear fiber optics." Nonlinear Science at the Dawn of the 21st Century. Berlin, Heidelberg: Springer Berlin Heidelberg, 2000. 195-211.

[14]. Maji, P. S., & Chaudhuri, P. R. Design of all-normal dispersion based on multi-material photonic crystal fiber in IR region for broadband supercontinuum generation. Applied Optics, 54(13), 4042-4048. (2015).

[15]. Munsaka, P., Baricholo, P., Rohwer, E. G., & Bosman, G. W. Mid Infrared supercontinuum generation in a silicon germanium photonic waveguide. Optics Continuum, 2(1), 9-20. (2022).

[16]. Dudley, J. M., & Coen, S. Coherence properties of supercontinuum spectra generated in photonic crystal and tapered optical fibers. Optics letters, 27(13), 1180-1182. (2002).

[17]. Nguyen, H. P. T., Tuan, T. H., Xing, L., Matsumoto, M., Sakai, G., Suzuki, T., & Ohishi, Y. Supercontinuum generation in a chalcogenide all-solid hybrid microstructured optical fiber. Optics Express, 28(12), 17539-17555. (2020).

[18]. Dudley, J. M., Genty, G., & Coen, S. Supercontinuum generation in photonic crystal fiber. Reviews of modern physics, 78(4), 1135-1184. (2006).

[19]. Hooper, L. E., Mosley, P. J., Muir, A. C., Wadsworth, W. J., & Knight, J. C. Coherent supercontinuum generation in photonic crystal fiber with all-normal group velocity dispersion. Optics express, 19(6), 4902-4907. (2011).

[20]. Salem, A. B., Diouf, M., Cherif, R., Wague, A., & Zghal, M. Ultraflat-top midinfrared coherent broadband supercontinuum using all normal As2S5-borosilicate hybrid photonic crystal fiber. Opt. Eng., 55(6), 066109. (2016).

[21]. Hashemi, S. A. S., & Noori, M. Dispersion tailoring of photonic crystal fibers for flat-top, coherent, and broadband supercontinuum generation. Physica Scripta, 95(7), 075501. (2020).

[22]. Medjouri, A., Abed, D., & Becer, Z. Numerical investigation of a broadband coherent supercontinuum generation in Ga8Sb32S60 chalcogenide photonic crystal fiber with all-normal dispersion. Opto-Electronics Review, 27(1), 1-9. (2019).

[23]. Zhang, M., Li, L., Li, T., Wang, F., Tian, K., Tao, H., ... & Yang, Z. Mid-infrared supercontinuum generation in chalcogenide fibers with high laser damage threshold. Optics Express, 27(20), 29287-29296. (2019).

[24]. Medjouri, A., & Abed, D. Theoretical study of coherent supercontinuum generation in

chalcohalide glass photonic crystal fiber. Optik, 219, 165178. (2020).

[25]. Medjouri, A., & Abed, D. Modelling of all-chalcogenide all-normal dispersion photonic crystal fiber for ultraflat mid-infrared supercontinuum generation. Optical and Quantum Electronics, 53, 1-22. (2021).

[26]. Maji, P. S., & Chaudhuri, P. R. Design of all-normal dispersion based on multi-material photonic crystal fiber in IR region for broadband supercontinuum generation. Applied Optics, 54(13), 4042-4048. (2015).

[27]. Baili, A., Cherif, R., & Zghal, M. Two octaves spanning supercontinuum in highly nonlinear As2Se3 nanophotonic crystal fiber for midinfrared applications. Journal of Nanophotonics, 9(1), 093059-093059. (2015).

[28]. Xiao, K., Ye, Y., & Min, R. Broadband coherent mid-infrared supercontinuum generation in all-chalcogenide microstructured fiber with all-normal dispersion. Frontiers in Physics, 10, 933010. (2022).

[29]. Nishizawa, N. Generation and application of high-quality supercontinuum sources. Optical Fiber Technology, 18(5), 394-402. (2012).

[30]. Cheung, C. S., Daniel, J. M. O., Tokurakawa, M., Clarkson, W. A., & Liang, H. Optical coherence tomography in the 2-µm wavelength regime for paint and other high opacity materials. Optics letters, 39(22), 6509-6512. (2014).

[31]. Colley, C. S., Hebden, J. C., Delpy, D. T., Cambrey, A. D., Brown, R. A., Zibik, E. A., ... & Cockburn, J. W. Mid-infrared optical coherence tomography. Review of Scientific Instruments, 78(12). (2007).

[32]. Cheung, C. S., Spring, M., & Liang, H. Ultra-high resolution Fourier domain optical coherence tomography for old master paintings. Optics express, 23(8), 10145-10157. (2015).

General Conclusion

In conclusion, we have presented and discussed the numerical analysis of SC generation in PCF based on $Ge_{20}As_{20}Se_{17}Te_{43}$chalcogenide in all-normal dispersion regime (ANDi). This CL-PCF is described by six rings of air holes, optimized to achieve a balance between high nonlinearity and desirable dispersion properties. The finite difference frequency domain (FDFD) method, along with perfectly matched layers (PML) boundary conditions, was used to calculate the linear and nonlinear optical properties of the fiber across various wavelengths. By numerically solving the generalized nonlinear Schrödinger equation (GNLSE), the study demonstrated the generation of a broad and coherent SC spectrum extending from 2.9 to 13.95 µm at a -5 dB spectral level. Key results showed that using a pump wavelength of 5.8 µm, a peak power of 15 kW, and a pulse duration of 50 fs, the $Ge_{20}As_{20}Se_{17}Te_{43}$-based PCF could produce a highly coherent SC in the mid-infrared region. This is attributed to the fiber's high Kerr nonlinearity (γ = 1,495 m^{-1}•W^{-1}) at a wavelength of 5.8 µm and its broad transparency range.

The results underscore the potential of this material and fiber design for advancing mid-infrared optical technologies, such as spectroscopy, environmental sensing, and biomedical imaging.

Future work

Several aspects warrant further exploration to build upon the theoretical and numerical findings of this study:

1. Experimental validation

While rigorous numerical simulations have been presented, experimental validation is crucial to confirm the findings and assess the practical feasibility of $Ge_{20}As_{20}Se_{17}Te_{43}$-based PCFs. Conducting experiments to generate SC using fabricated PCFs will provide direct insights into their performance under real-world conditions.

2.Optimization of fiber design

Refining the PCF structure, such as varying the air hole size, lattice arrangement, or introducing hybrid designs, could significantly enhance SC generation efficiency and achieve broader spectral coverage. Such optimizations may also reduce propagation losses and improve overall spectral coherence.

3. Material innovations

Although $Ge_{20}As_{20}Se_{17}Te_{43}$ glass exhibits excellent nonlinear optical properties, exploring alternative chalcogenide materials with higher transparency and lower propagation losses could unlock additional potential. Materials with even higher Kerr nonlinearity or broader transparency windows may enable the generation of more efficient and expansive SC spectra.

This research paves the way for advancements in nonlinear optical technologies, with promising applications in spectroscopy, environmental sensing, and biomedical imaging. The unique combination of high nonlinearity and broad transparency in $Ge_{20}As_{20}Se_{17}Te_{43}$-based PCFs makes them an ideal platform for next-generation optical devices. With continued theoretical and experimental efforts, this work holds great potential for advancing mid-infrared SC sources and their diverse applications.

International publications in peer-reviewed journals

Tahar Mesbahi, Abdelkader Medjouri, " Simulation and modeling of supercontinuum generation in GAST chalcogenide PCF". Optoelectronics and Advanced Materials – Rapid Communications, 19(7-8), 318-327. (2025).

International conferences

Abdelkader Medjouri, **Tahar Mesbahi**, and Djamel Abed, "Broadband laser source based on supercontinuum generation in all-normal dispersion chalcogenide photonic crystal fiber," 2nd Algerian-German International Conference on New Technologies and their Applications (AGICNT'2019), University Ferhat Abbas – Sétif 1, Algeria, September 2019.

Abdelkader Medjouri, **Tahar Mesbahi**, and Djamel Abed, "Supercontinuum laser source based on chalcogenide glass microstructured optical fiber for optical coherence tomography," 1st International Conference on Sustainable Energy and Advanced Materials (IC-SEAM'21), Ouargla, Algeria, April 2021.